SUPERRADIANCE AND TOPOLOGICAL QUANTUM OPTICS IN ATOMIC MEDIUM AND CAVITY QED

A Dissertation

by

HAN CAI

Submitted to the Office of Graduate and Professional Studies of
Texas A&M University
in partial fulfillment of the requirements for the degree of

DOCTOR OF PHILOSOPHY

Chair of Committee,	Marlan O. Scully
Committee Members,	Edward S. Fry
	Philip R. Hemmer
	Alexei V. Sokolov
	M. Suhail Zubairy
Head of Department,	Peter M. McIntyre

December 2017

Major Subject: Physics

ABSTRACT

In this dissertation we focused on two topics: 1. atomic cooperative effect, including superradiance, subradiance and collective Lamb shift in an atomic ensemble; 2. novel topological effect in quantum optics system, such as Haldane model, synthetic magnetic field in superradiance lattice and synthetic spin-orbit interaction in Fock-state lattices.

In the first part, we start from the Dicke state, an N-particle atomic ensemble excited by a single photon. Due to the interaction of the atoms with a continuum of vacuum modes, the Dicke state has a larger decay rate compared with an isolated atom, termed the single photon superradiance. In the "opposite" case, the single-photon subradiance state does not decay because of the destructive interference of the atomic transitions. We study the pro-tection of subradiant states by the symmetry of the atomic distributions in the Dicke limit, in which collective Lamb shifts cannot be neglected. We find that antisymmetric states are subradiant states for distributions with reflection symmetry. Continuous symmetry can also be used to achieve subradiance in an extended ensemble. This study is relevant to the problem of robust quantum memory with long storage time and fast readout.

In the second part, we start from introducing the concepts, methods, and models from quantum optics or condensed matter physics. They include the timed-Dicke states, electromagnetically induced transparency, coupled wave equations, tight-binding model, band theory, Floquet theory, superradiance lattice, integer quantum Hall effect, Haldane model, etc.. Based upon these tools, we study three topological quantum optics systems: (i) a Haldane model with $in\ situ$ tunable topological properties in a two-dimensional momentum-space superradiance lattice composed of timed Dicke states in electromagnetically induced transparency; (ii) a spin-orbit coupled Fock-state lattice, which introduce a novel quantum operation to generate mesoscopic superposition states, e.g., the NOON states and cat

states; (iii) a synthetic magnetic field created in a quasi one dimensional superradiance lattice, which is predicted to be observed in thermal vapours of alkali atoms instead of only in cold atoms (as in previous experiments). This study aims to provide a novel, highly tunable platform simulating exotic phenomena in condensed matter physics and offers a basis of topological quantum optics and novel photonic devices.

DEDICATION

I want to thank I hereby thank all my family, my advisor, my colleagues, and my friends for their support and help during the years of my Ph.D study.

I sincerely thank my advisor, Marlan O. Scully, who has given me various opportunities to study and research in the field of quantum optics; his sharp instinct for physics and his teaching of philosophy in scientific career always inspire me, not to mention his kind support on many aspects of life. I'm grateful that I had the previlege to work with the pioneer of quantum optics. I also want to show special gratefull to Da-Wei Wang, who not only guides me on the research projects, teaches me the arcane techniques in the physics realm (not only quantum optics), but also kindly carry me on the way to live an interesting lifestyle, including swimming, skiing, hiking and many more. I'm sincerely appreciate his mentoring.

I also would like to thank my committee members: Edward Fry, Philip Hemmer, Alexei V. Sokolov, and M. Suhail Zubairy for guiding and helping me in my research. Many thanks are owed to the teachers who gave wonderful classes during these years: Girish Agarwal, Artem Abanov, Katrin Becker, Alexey Belyanin, Dudley Herschbach, Teruki Kamon, Christopher Pope, Rainer Fries, Helmut G. Katzgraber, George Welch, Hans Schuessler, Valery Pokrovsky, and Aleksei Zheltikov. I also learned a lot from my colleagues: Zhenhuan Yi, Narangerel Altangerel, Gombojav O. Ariunbold, Charles W. Ballmann, Tuguldur Begzjav, Ziyun Di, Dawson Nodurft, Yuri V. Rostovtsev, Jonathan V. Thompson, Dmitri V. Voronine, Kai Wang, Luqi Yuan, Kimberly R. Chapin, Yujie Shen, John Mason, Xiwen Zhang, Anatoly Svidzinsky, Hui Dong, Moochan Kim, Luojia Wang, Chris O′brian, Tao Peng, Shengwen Li, Lida Zhang, Rongxin Chen, Zeyang Liao, Xiaodong Zeng, Zhenhong Li, Alexandra Zhdanova, Sriteja Upadhyayula, Fu Li, Wei Feng,

Haozhen Li, Jingwei Fan, Jinze Wu, Liangchao Chen, and many others. Their help made this dissertation possible. I also thank all my friends for giving me a wonderful time in College Station.

I would like to thank my family, my parents and my wife, for accompanying and supporting me. My father, Linggen Cai, is always there to support my decision and offers me enormous help in every aspect. My mother, Yuqin Li, cares me as much as she can over the Pacific. They are always there for me, giving me strength. My wife, Peng Wang, is also a PhD candidate in A&M. It is in the city of college station, we met, fell in love, and got married. She gives me a lovely home, in which we grow up independently and cooperatively.

CONTRIBUTORS AND FUNDING SOURCES

Contributors

This work was supervised by a dissertation committee consisting of Professor Marlan O. Scully (advisor) and Edward S. Fry, Alexei V. Sokolov, and M. Suhail Zubairy of the Department of Physics & Astronomy and Professor Philip R. Hemmer of the Department of Electrical & Computer Engineering. All work for the dissertation was completed by the student, in collaboration with Da-Wei Wang and Marlan O. Scully of the Department of Physics and Astronomy.

Funding Sources

Graduate study was supported by the Herman F. Heep and Minnie Belle Heep Texas A&M University Endowed Fund held/administered by the Texas A&M Foundation. The work is make possible in part by Robert A. Welch Foundation (Grant No. A-1261).

NOMENCLATURE

EIT	Electromagnetically Induced Transparency
QED	Cavity Quantum Electrodynamic
TDS	Timed-Dicke State
SL	Superradiant Lattice
BEC	Bose-Einstein Condensate
BZ	Brillouin Zone
NN	Nearest Neighbor
NNN	Next Nearest Neighbor
SWEIT	Standing Wave-Coupled EIT
DOS	Density of States
QHE	Quantum Hall Effect
AB	Aharonov-Bohm
LL	Landau level
TI	Topological Insulator
TSL	Topological Superradiance Lattice

TABLE OF CONTENTS

Page

LIST OF FIGURES

FIGURE Page

LIST OF TABLES

TABLE Page

1. INTRODUCTION

1.1 Motivation and Objectives

Interaction of light with matter is one of the major subjects in the research of quantum optics. Collective phenomenon, quantum coherence and interference have led to many novel effects. For instance, electromagnetically induced transparency (EIT) [1, 2, 3], amplification or lasing without population inversion [4, 1, 5], ultraslow light [6], directional emission of superradiance [7], single-photon subradiance [8], collective Lamb shift [9, 10, 11], quantum heat engine [12], efficient solar cells [13], etc..

Superradiance & subradiance (the enhanced & inhibited of spontaneous emission) of atomic ensembles and collective Lamb shift (cooperative vacuum-induced energy shifts) are the two sides of the same coin, which originates from the interaction of the atomic system with a common continuum of vacuum modes. Superradiance is first predicted by Dicke in 1954 [14]. It features an enhanced spontaneous decay rate much greater than that of an isolated single atom. The influence of virtual transition has attracted much attention, both in theoretical [15, 16, 17, 18, 19, 20, 21] and experimental study [22, 23, 24, 25]. Recently, Scully [8] proposed a new way to control spontaneous emission by preparing and switching between subradiant and superradiant states. We extend the idea and analyze the relation between cooperative emission and the symmetry of the atomic distribution.

Topological phases of matter [26, 27, 28, 29, 30, 31] are of fundamental interest and have promising applications. Fascinating topological properties of light have been unveiled in photonic structures [32, 33, 34, 35, 36], time-periodic systems [37, 38, 39, 40], and optical lattices of cold atoms [41]. However, the manifestation of topological physics in quantum optics has not been discovered. We study the topological effect in the scheme of standing-wave-coupled EIT and cavity quantum electrodynamic (QED), which provides

a controllable platform for exotic phenomena in condensed matter physics and offer a basis of topological quantum optics and novel photonic devices.

1.2 Outline

The outline of the present dissertation is summarized here.

In Section 2, we discuss briefly the mathematical framework used to study the interaction of matter with radiation. We derive the explicit form of the vacuum-induced cooperative interaction in the reduced density operator of the atomic system. We present the influence of atomic distribution in the single-photon subradiance. In both the Dicke-limit and an extended ensemble, we demonstrate the mitigation of the collective Lamb shift, which degrade the subradiance in general, and the symmetry-protected subradiance.

In Section 3, we give a brief introduction of EIT, especially the susceptibility with respect to probe field with a standing wave coupling field. Near the phase matching condition, a two-mode approximation is justified and we obtain the coupled-wave equations. Using the equations, we construct a novel way to probe the topological phase in quantum optics system in later sections.

In Section 4, we review the band theory, including near-free electron model and tight-binding model. The latter, in this dissertation, is the key connection between quantum optics and condensed matter physics. Then we introduce the Floquet (temporal periodic) theory by comparing it with Bloch (spatial periodic) theory. The temporal modulation is crucial for breaking the time-reversal symmetry and generating the non-trivial topological phase.

In Section 5, we discuss the Timed-Dicke state (TDS) and show that the TDS of a collection of three-level atoms can form a tight-binding lattice in momentum space. This lattice, coined the superradiance lattice (SL), can be constructed based on EIT. In order to verify the equivalence between one-dimensional (1D) superradiance lattice and standing

wave-coupled EIT, we experimentally measure the quantum transportation in a 1D SL of a Bose-Einstein condensate (BEC) based on a configuration of standing wave-coupled EIT. Resonantly excited to a superradiant state, the BEC is further transported to other collective excited states, which form a 1D SL, by the two coupling fields of the EIT. The directional emission of one of the superradiant excited state in the 1D SL is measured. The quantum transportation depends on the band structure, which can be controlled by the frequency and intensity of the standing-wave coupling laser fields.

In Section 6, we review the novel topological effect in condensed matter physics, including integer quantum Hall effect (IQHE) and the Haldane model. We derive the Kubo formula for the quantum conductivity, giving out a direct connection between the Hall conductivity and a quantity, i.e., the Chern number, which characterizes the topological property of the eigenwavefunction within the Brillouin zone (BZ). Therefore we show that the quantization of their conductivities originates from a topological number. Here we also discuss the edge-bulk correspondence. In a topologically non-trivial system with a finite size, the uni-directional transport of the edge state, as well as the Chern number, manifests its topological property.

In Section 7, we study the topological phases in a two-dimensional momentum-space SL composed of TDSs in a scheme of EIT. By periodically modulating the three EIT coupling fields, we can create a Haldane model with $in\ situ$ tunable topological properties, which manifest themselves in the contrast between diffraction signals emitted by the superradiant TDSs.

In Section 8, we present a novel system to prepare mesoscopic superposition states of photons, in which three cavities interacting with the same two-level atom. By periodically modulating the three cavity frequencies around the transition frequency of the atom with a $2\pi/3$ phase difference, the time reversal symmetry is broken and an optical circulator is generated with chiralities depending on the quantum state of the atom. A superposition of

the atomic states can guide photons from one cavity to a mesoscopic superposition of the other two cavities. The physics can be understood in a finite spin-orbit-coupled Fock-state lattice, which is closely related to the Haldane model realization in Sec. 7.

In Section 9, we show that effective magnetic field can be synthesized for the wave-mixing process. By introducing two standing waves coupled EIT with different frequencies, i.e., one is near resonant while the other is far off-resonate, a uniform effective magnetic field can be created in a quasi one dimensional tight-binding lattice. The chiral edge transportation can be tested by the multi-wave-mixing signals, which can be observed in thermal vapors of alkali atoms.

In Section 10, we summarize the key results presented in this dissertation.

2. SYMMTRY-PROTECTED SINGLE-PHOTON SUBRADIANCE*

2.1 Introduction

Cooperative spontaneous emission (Dicke superradiance [14]) and the cooperative vacuum induced levels shifts (Lamb shifts [43]) are hot topics in quantum optics. For extended ensembles when the size of the atomic cloud is much larger than the wavelength, the directional emission [7, 44] and collective Lamb shift [11] of single photon superradiance [45, 46, 47, 48, 7, 18, 19, 49, 50] have attracted much interest. Recently it has been shown [8] that it is possible to use subradiance (the cooperative suppression of spontaneous emission [50]) to store a photon in a small volume for many atomic lifetimes; and later switch the subradiant state to a superradiant state which emits a photon in a small fraction of an atomic lifetime. Such a process has potential applications in e.g., quantum informatics.

It has been proved that the distribution of the atoms (e.g., periodic or random) in an extended ensemble has a substantial effect on cooperative spontaneous emission [51]. However, the effect of the atomic distribution in the Dicke limit has been studied only a little. Since the distance between atoms is much smaller than the wavelength, one might guess that the distribution of atoms is not important. We here show that the collective Lamb shift cannot be neglected in general. However, by analyzing the relation between the symmetry of the atomic distribution and cooperative emission, we demonstrate the mitigation of the collective Lamb shift and the symmetry protected subradiance.

2.2 Hamiltonian

The Hamiltonian between a collection of identical two-level atoms, contains a ground state g and an excited state e, and radiation field is well known. If the $-\mathbf{A}\cdot\mathbf{p}$ interaction

*Reprinted with permission from "Symmetry-protected single-photon subradiance" by H. Cai, D.-W. Wang, A. A. Svidzinsky, S.-Y. Zhu, and M. O. Scully , 2016. Phys. Rev. A, 93, 053804 [42], Copyright 2017 by APS

is used, with dipole-dipole interaction V_{ij} included and terms A^2 ignored, the interaction Hamiltonian is

$$\begin{aligned} H &= H_0 + H_I + H_d, && (2.1)\\ H_0 &= \hbar\omega_0 \sum_i \sigma_i^z + \hbar \sum_{\mathbf{k}s} \nu_{\mathbf{k}} a_{\mathbf{k}s}^\dagger a_{\mathbf{k}s}, && (2.2)\\ H_I &= \hbar \sum_{i\mathbf{k}s} g_{i\mathbf{k}s} \frac{\omega_0}{\nu_{\mathbf{k}}} a_{\mathbf{k}s} e^{i\mathbf{k}\cdot\mathbf{r}_i} (\sigma_i^+ + \sigma_i^-) + h.c., && (2.3)\\ H_d &= \sum_{i\neq j} V_{ij} \sigma_i^+ \sigma_j^-, && (2.4) \end{aligned}$$

where the operator σ_j^z, $\sigma_j^\pm$ defined above satisfy the angular momentum commutation relation corresponding to spin $1/2$ value, i.e., $\sigma_j^z = |e\rangle\langle e| - |g\rangle\langle g|$and $\sigma_j^+ = (\sigma_j^-)^\dagger = |e\rangle\langle g|$, $\mathbf{k}(s)$ is the wavevector (polarization) of the radiation field, $\omega_0 = E_e - E_g$, the atomic transition frequency, $\nu_{\mathbf{k}} = kc$, and the coupling coefficient is given by

$$g_{i\mathbf{k}s} = -\sqrt{\frac{\nu_{\mathbf{k}}}{2\epsilon_0 \hbar V_{ph}}} \boldsymbol{\mu}_i \cdot \boldsymbol{\varepsilon}_{\mathbf{k}}, \tag{2.5}$$

where V_{ij} is the dipole-dipole interaction

$$V_{ij} = \frac{\boldsymbol{\mu}_i \cdot \boldsymbol{\mu}_j - 3(\boldsymbol{\mu}_i \cdot \hat{\mathbf{r}}_i)(\boldsymbol{\mu}_i \cdot \hat{\mathbf{r}}_j)}{r_{ij}^3}, \tag{2.6}$$

and $\mathbf{r}_{ij} = \mathbf{r}_i - \mathbf{r}_j = r_{ij}\hat{\mathbf{r}}_{ij}$. In the interaction picture, the field-atom coupling term is simply

$$\begin{aligned} V &= e^{iH_0 t/\hbar} H_I e^{-iH_0 t/\hbar}, \\ &= \sum_{i\mathbf{k}s} g_{i\mathbf{k}s} \frac{\omega_0}{\nu_{\mathbf{k}}} a_{\mathbf{k}s} e^{i\mathbf{k}\cdot\mathbf{r}_i - i\nu_{\mathbf{k}} t} (\sigma_i^+ e^{i\omega_0 t} + \sigma_i^- e^{-i\omega_0 t}). \end{aligned} \tag{2.7}$$

2.3 Master Equation Approach

Let us consider the spontaneous emission using the general reservoir theory [52],

$$\begin{aligned}\dot{\rho}_a = &-\frac{i}{\hbar}[H_d, \rho_a(t)] - \frac{i}{\hbar}\mathrm{Tr}_R[V(t), \rho_a(t_0)\otimes\rho_R(t_0)] \\ &- \frac{1}{\hbar^2}\mathrm{Tr}_R\int_{t_0}^{t} d\tau[V(t),[V(\tau),\rho_a(\tau)\otimes\rho_R(t_0)]],\end{aligned} \tag{2.8}$$

the reduced density operator for the atomic system ρ_a is obtained by taking a trace over the reservoir coordinates, i.e., $\rho_a(t) = \mathrm{Tr}_R(\rho_a(t)\otimes\rho_R(t_0))$, where we assume the reservoir is always at equilibrium. On inserting the interaction energy Eq. (2.7) into the the equation of motion Eq. (2.8), we obtain (ignoring the suffice a)

$$\begin{aligned}\dot{\rho} = &-\frac{i}{\hbar}[H_d + \sum_{ij}\Omega_{ij}^{Ap}\sigma_i^+\sigma_j^-, \rho(t)] - \sum_{ij}\gamma_{ij}^+(\sigma_i^+\sigma_j^-\rho - 2\sigma_j^-\rho\sigma_i^+ + \rho\sigma_i^+\sigma_j^-) \\ &- \sum_{ij}\gamma_{ij}^-(\sigma_i^-\sigma_j^+\rho - 2\sigma_j^+\rho\sigma_i^- + \rho\sigma_i^+\sigma_j^-),\end{aligned} \tag{2.9}$$

where

$$\gamma_{ij}^{\pm} = \sum_{ij\mathbf{k}s} g_{i\mathbf{k}s}g_{j\mathbf{k}s}^*\frac{\omega_0^2}{\nu_{\mathbf{k}}^2}e^{i\mathbf{k}\cdot(\mathbf{r}_i-\mathbf{r}_j)}\pi\delta(\nu_{\mathbf{k}}\mp\omega_0), \tag{2.10}$$

$$\Omega_{ii} = -\sum_{\mathbf{k}s}|g_{i\mathbf{k}s}|^2\frac{\omega_0^2}{\nu_{\mathbf{k}}^2}(\frac{1}{\nu_{\mathbf{k}}-\omega_0} - \frac{1}{\nu_{\mathbf{k}}+\omega_0}), \tag{2.11}$$

$$\Omega_{ij}^{Ap} = -\sum_{\mathbf{k}s} g_{i\mathbf{k}s}g_{j\mathbf{k}s}^*\frac{\omega_0^2}{\nu_{\mathbf{k}}^2}e^{i\mathbf{k}\cdot(\mathbf{r}_i-\mathbf{r}_j)}(\frac{1}{\nu_{\mathbf{k}}-\omega_0} + \frac{1}{\nu_{\mathbf{k}}+\omega_0}), \tag{2.12}$$

In the derivation of Eq. (2.10-2.12), we utilize the Markov approximation and the relation $[\sigma_i^+\sigma_i^-,\rho] = -[\sigma_i^-\sigma_i^+,\rho]$. The sum over $\mathbf{k}$ may be replaced by an integral through the standard prescription

$$\sum_{\mathbf{k}} \to \frac{V}{(2\pi)^3}\int_0^{4\pi} d\Omega'\int_0^{\infty} dkk^2, \tag{2.13}$$

then we assume that all the atomic dipole along z direction,$\boldsymbol{\mu}_i = \mu\hat{z}$, the unit displacement between two atoms is$\hat{\mathbf{r}}(\theta,\phi) = \sin\theta\cos\phi\hat{x} + \sin\theta\sin\phi\hat{x} + \cos\theta\hat{z}$, the directions of the wavevector and polarization of the radiation field are denoted by $\mathbf{k}/\left|\mathbf{k}\right| = \sin\theta'\cos\phi'\hat{x} + \sin\theta'\sin\phi'\hat{y} + \cos\theta'\hat{z}$, $\boldsymbol{\varepsilon}_1 = \sin\phi'\hat{x} - \cos\phi'\hat{y}$ and $\boldsymbol{\varepsilon}_2 = -\cos\theta'\cos\phi'\hat{x} + \cos\theta'\sin\phi'\hat{y} + \sin\theta'\hat{z}$. On using the expansion

$$e^{i\mathbf{k}\cdot\mathbf{r}} = 4\pi\sum_{lm} i^l j_l(kr)Y^*_{lm}(\theta,\phi)Y_{lm}(\theta',\phi'), \tag{2.14}$$

we obtain the decay rate

$$\gamma^-_{ij} = 0, \tag{2.15}$$

and (ignoring the "+" since $\gamma^-_{ij} = 0$)

$$\begin{aligned}\gamma_{ij}(\theta,r) &= \frac{\mu^2\omega^2\pi}{2\epsilon_0\hbar(2\pi)^3c}\int_0^\infty dkk\int d\Omega' e^{i\mathbf{k}\cdot\mathbf{r}}\sin^2\theta'\delta(\nu_{\mathbf{k}}-\omega_0)\\ &= \frac{3\Gamma}{4}[(1-\cos^2\theta)\frac{\sin k_0r}{k_0r} + (1-3\cos^2\theta)(\frac{\cos k_0r}{(k_0r)^2} - \frac{\sin k_0r}{(k_0r)^3})],\end{aligned} \tag{2.16}$$

where $\Gamma = \mu^2\omega^3/3\epsilon_0\hbar\pi c^3$ is the single atom spontaneous decay rate and k_0 is the transition wave vector. The collective Lamb shift is calculated via residue theorem

$$\begin{aligned}\Omega_{ij}(\theta,r) &= \frac{\mu^2\omega^2\pi}{2\epsilon_0\hbar(2\pi)^3c}\int_0^\infty dkk\int d\Omega' e^{i\mathbf{k}\cdot\mathbf{r}}\sin^2\theta'(\frac{1}{\nu_{\mathbf{k}}-\omega_0} + \frac{1}{\nu_{\mathbf{k}}+\omega_0}) + V_{ij}\\ &= \frac{3\Gamma}{4}[-(1-\cos^2\theta)\frac{\cos k_0r}{k_0r} + (1-3\cos^2\theta)(\frac{\sin k_0r}{(k_0r)^2} + \frac{\cos k_0r}{(k_0r)^3})],\end{aligned} \tag{2.17}$$

where $\Omega_{ij}(\theta,r) = \Omega^{Ap}_{ij}(\theta,r) + V_{ij}$. it should be notice that the integral in Eq. (2.17) has poles at $k = \pm k_0, 0$. It can be shown by contour integration that the contribution from $k = 0$ is precisely $-V_{ij}$ and thus cancels the dipole-dipole interaction term. The evaluation

of Ω_{ii} is a profound and involved problem. It is essentially Lamb shift and is given by

$$\Omega_{ii} = -\frac{\Gamma}{\pi k_0}\int_0^\infty dkk(\frac{1}{k-k_0} - \frac{1}{k+k_0}) = -\frac{\Gamma}{\pi}\ln\left|\frac{\omega_c^2}{\omega_0^2} - 1\right|, \tag{2.18}$$

where ω_c is the non-relativistic cut-off frequency, i.e., $\hbar\omega_c = mc^2$. One remark is that leading divergence of Ω_{ii} is not linear, but logarithmic, as it must be in a correct non-relativistic calculation even without mass-renormalization [53]. For simplicity's sake, sometimes we can use the "scaler" field theory by ignoring the polarization of field, i.e., $g_{i\mathbf{k}s} = -\sqrt{\frac{\nu_\mathbf{k}}{2\epsilon_0\hbar V_{ph}}}\mu_i$. The collective Lamb shift and collective decay rate is

$$\Omega_{ij}^s = -\Gamma_s\frac{\cos k_0 r}{k_0 r} \tag{2.19}$$

$$\Gamma_{ij}^s = \Gamma_s\frac{\sin k_0 r}{k_0 r} \tag{2.20}$$

which can be regarded as the average effect of the vector field in Eqs. (2.16) & (2.17) [54, 16].

2.4 Single Photon Superradiance and Subradiance

Having motivated our interest in the problem that the N-atom ensemble excited by a single photon, we now turn to an analysis of the correlated spontaneous emission from N atoms in free-space induced by the collective Lamb shift and decay. We look for a solution of the Schrodinger equation for the atoms as a superposition which decay exponentially

$$|\psi_n(t)\rangle = \sum_{j=1}^N \beta_j e^{-\Lambda_n t/\hbar}|j\rangle \tag{2.21}$$

where $|j\rangle = |b_1, b_2 ... a_j ... b_N\rangle$ is the subspace of single excitation and $a_j(b_j)$ is the excited (ground) state of the jth atom, Λ_n is the nth complex eigenvalue and β_j is the probability amplitude to find atom j excited. In order to describe the dynamics of the subspace, we

can rewrite the master equation of the atoms Eq. (2.9)

$$\dot{\rho} = -\frac{i}{\hbar}[H_{eff}\rho - \rho H_{eff}^{\dagger}] + \sum_{ij} 2\gamma_{ij}^{+}\sigma_{j}^{-}\rho\sigma_{i}^{+}, \tag{2.22}$$

where $H_{eff} = (\sum_{i\neq j}\Omega_{ij} - i\sum_{ij}\gamma_{ij})\sigma_{i}^{+}\sigma_{j}^{-}$ (we ignore the single atom Lamb shift since it is not interested to us in studying the cooperative effect). Since the last term in the right side of the master equation is irrelevant of the subspace of single excitation, we can plug the solution ansatz Eq. (2.21) and the effective Hamiltonian into the Schrodinger equation

$$i\hbar\frac{d}{dt}|\psi_n\rangle = -i\Lambda_n|\psi_n\rangle = H_{eff}|\psi_n\rangle, \tag{2.23}$$

the eigenvalue equations are [19, 55]

$$\Lambda_n\beta_i = \Gamma\beta_i - i\sum_{i\neq j}(-\Omega_{ij} + i\gamma_{ij})\beta_j = \sum_{j}^{N} M_{ij}\beta_j \tag{2.24}$$

with $M_{ij} = \Gamma\delta_{ij} + (i\Omega_{ij} + \gamma_{ij})(1 - \delta_{ij})$ with δ_{ij} the Kronecker delta function are the elements of the evolution matrix $\mathbf{M}$. Numerically calculating all eigenvalues Λ_n by diagonalization of the matrix $\mathbf{M}$, we obtain $|\Psi(t)\rangle = \sum_n c_n e^{-\Lambda_n t}|\psi_n\rangle$, where $c_n = \langle\psi_n^T|\Psi(0)\rangle$ is the projection of the initial state to the single-photon Dicke-Lamb eigenstate and $\langle\psi_n^T|$ is the transpose of $|\psi_n\rangle$ (since the matrix $\mathbf{M}$ is symmetric instead of Hermitian). Therefore, the dynamics of the state is essentially determined by the matrix $\mathbf{M}$, i.e., the atomic distribution of the system.

The N-atom sample (size much smaller compared to the transition wavelength λ) excited by a single photon can be described by the Dicke state

$$|+\rangle = \frac{1}{\sqrt{N}}\sum_{j=1}^{N}|j\rangle. \tag{2.25}$$

Since the size of the atom is much smaller than the wavelength of the coupling field, we could use the dipole approximation. It also allows us to distribute many atoms within one wavelength, which is called the Dicke limit. The probability amplitude of the state (2.25) decays at the rate $\Gamma_+ = N\Gamma$, where 2Γ is the single-atom population decay rate. In the "opposite" case, if we neglect the Lamb shift, the single-photon subradiance state

$$|-\rangle = \frac{1}{\sqrt{N}}(\sum_{j=1}^{N/2} |j\rangle - \sum_{j=N/2+1}^{N} |j\rangle) \tag{2.26}$$

does not decay, i.e., $\Gamma_- = 0$, because of the destructive interference of the atomic transitions. However, when the cooperative Lamb shifts Ω_{ij}, i.e., the effects of emission and reabsorption of virtual photons, are counted in, it can degrade superradiance [11, 56, 57]. In single-photon superradiance, this does not overwhelm the collective enhancement of spontaneous emission. This is not so in the case of subradiance, where the collective Lamb shift can now destroy the ability of the atoms to "store" light, i.e., the original subradiant states are no longer necessarily subradiant. For random atomic distribution, since each atom "sees" different neighboring atoms, collective Lamb-shift-type fluctuation-induced dephasing significantly degrades the destructive interference.

2.4.1 Dicke Limit

We first turn to a more detailed study of the lifetime of the $|-\rangle$ state and the way in which collective Lamb shift type fluctuations influence the state evolution. Numerically calculated population decay of the anti-symmetric $|-\rangle$ state with and without taking into account virtual transitions is compared in Fig. (2.1). The Dicke limit ensemble of 100 atoms are randomly distributed along a 1D line within 0.01λ, where λ is the atomic transition wavelength. Fig. (2.1) shows that collective Lamb shifts Ω_{ij} degrade subradiance of the state $|-\rangle$. Without Lamb shifts, $|-\rangle$ is subradiant. Counting in the Lamb shifts,

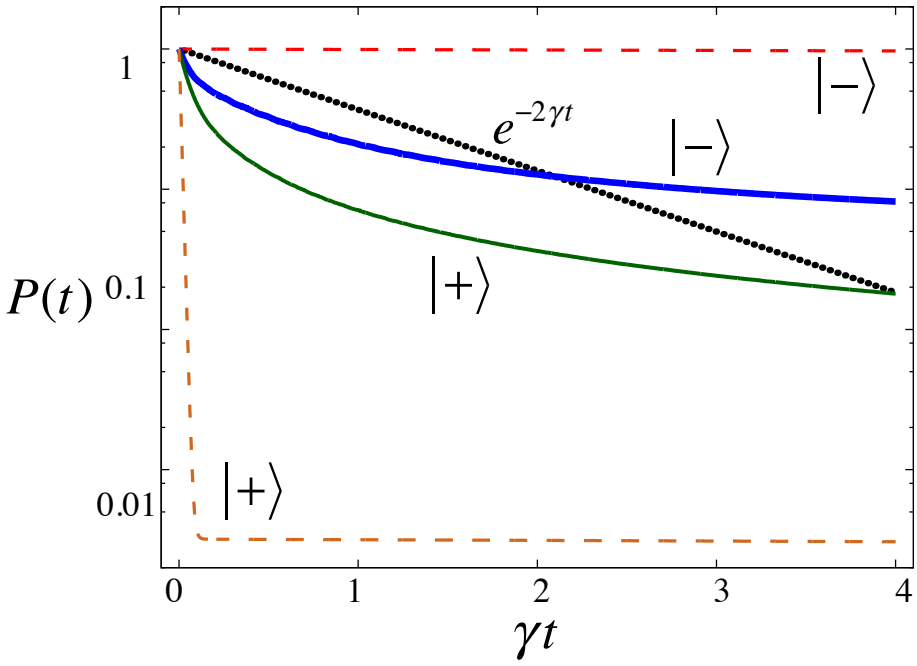

Figure 2.1: Probability $P(t) = \langle\Psi(t)|\Psi(t)\rangle$ to find atoms excited as a function of time for atoms initially prepared in the $|+\rangle$ and $|-\rangle$ states. The solid curve takes the cooperative Lamb shift into consideration, causing rapid decay for both $|+\rangle$ and $|-\rangle$. The dashed curve ignores the Lamb shift. For comparison, we also plot single-atom decay curve $e^{-2\gamma t}$ (dot line).

$|-\rangle$ is composed by both superradiant and subradiant eigenstates. The components of the superradiant eigenstate decay fast, leaving slowly decaying subradiant components. We use the scalar field, in Eq. (2.19) & (2.20), throughout this section for simplicity. There is no essential difference between the results of the scalar and vector fields.

The mitigation of the collective Lamb shifts by arranging the atom distribution in a ring has been found useful in maintaining superradiance [58]. If the atoms are distributed randomly, the transition frequencies of atoms are different due to the different environment of each atom, superradiance is destroyed. However, if they are arranged periodically on a ring, all atoms have the same environment and the superradiance is recovered. It sheds light on the importance of the symmetry of the atomic distribution.

Symmetry has long been investigated as a central feature of superradiance [44]. In Dicke's original paper [14], it was noted that the most decaying excited state of the collective atomic distribution must be symmetric since the ground state is symmetric and the Hamiltonian preserves symmetry. The symmetry of the atomic distribution determines the symmetry of the eigenstates. For the sake of simplicity, we take 1D atomic distribution preserving reflection symmetry for example. We set z along the line of atoms and $z = 0$ as the middle point of the atomic ensemble. The mirror reflection operator π, which transforms $z \to -z$, commutes with the matrix $\mathbf{M}$ for a periodic distribution of atoms, $[\mathbf{M}, \pi] = 0$. A nondegenerate eigenstate of $\mathbf{M}$ is also an eigenstate of π [59]. N eigenstates of N atoms excited by a single photon are separated into two groups with opposite eigenvalues of π, i.e., $N/2$ symmetric and $N/2$ anti-symmetric states.

In the Dicke limit, the ensemble size is much smaller than the transition wavelength. If we neglect the collective Lamb shifts Ω_{ij} in Eq. (2.24), we obtain $M_{ij} = \gamma$ for all i and j. In this case the eigenvalues of $\mathbf{M}$ are $\Lambda_1 = N\gamma$ and all others are equal to zero, i.e., there is one superradiant state and $N - 1$ subradiant states [16]. The superradiant eigenstate is the symmetric state $|+\rangle$. Any state orthogonal to this state is subradiant, for example, the anti-symmetric state $|-\rangle$. With the presence of Ω_{ij}, $|-\rangle$ is not subradiant any more, as shown in Fig. (2.1).

We can recover the subradiant nature of $|-\rangle$ state by rearranging atoms such that their distribution possesses reflection symmetry, i.e., $z_j = -z_{N+1-j}$ and $\pi^\dagger \mathbf{M} \pi = \mathbf{M}$. In Fig. (2.2b) we plot the population decay for periodic distribution of atoms. The decay of $|+\rangle$ is enhanced compared with the case of random distribution, which is consistent with Ref. [58]. On the other hand, the decay of $|-\rangle$ state is drastically inhibited.

To analyze the reason of this inhibition, we plot β_j for the superradiant state $|\psi_1\rangle$ and for a subradiant state $|\psi_2\rangle$ in the inset of Fig. (2.2a). It is clear that the state $|\psi_1\rangle$ is symmetric with respect to the center of the sample. There is only one superradiant state

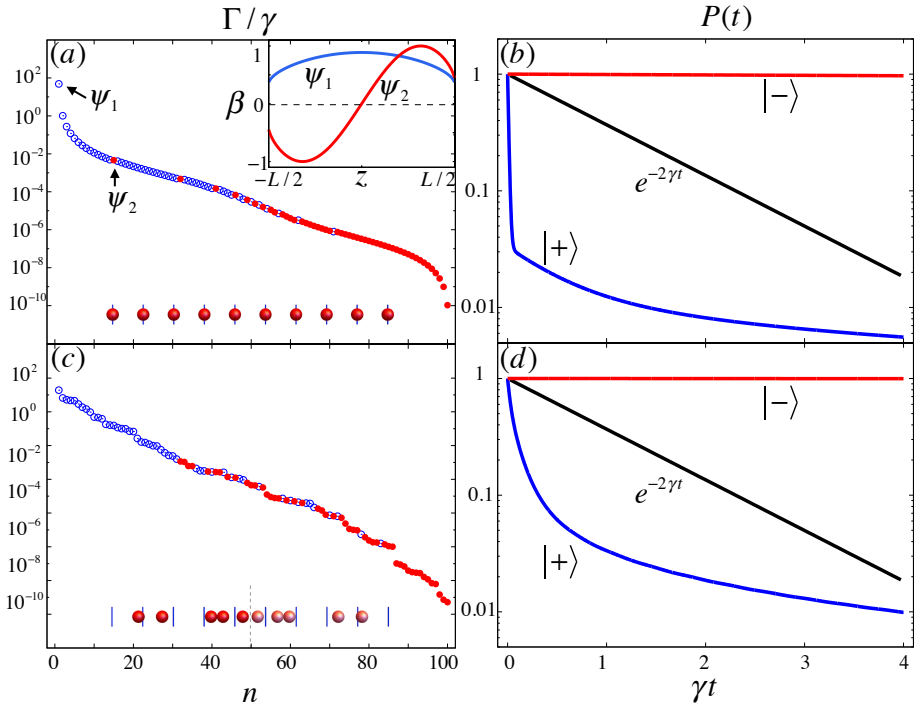

Figure 2.2: (a) Distribution of decay rates for eigenstates of an ensemble of 100 atoms regularly placed along a line with spacing between adjacent atoms 0.0001λ. Blue empty dots are symmetric states while red solid dots are anti-symmetric states. Inset: Probability amplitude β_j as a function of the coordinate of the jth atom z_j for the fastest decaying symmetric (blue line) and anti-symmetric (red line) states. (b) Population decay of states $|+\rangle$ and $|-\rangle$ as a function of time. Single-atom exponentially decaying curve is shown for comparison. (c) and (d): The same as in (a) and (b), but for random spatial distribution of atoms with reflection symmetry.

$|\psi_1\rangle$ with decay rate $\sim N\gamma$, as shown in Fig. (2.2a). The anti-symmetric state $|-\rangle$ is orthogonal to the superradiant state $|\psi_1\rangle$. Because of the Dicke limit, the superradiant state $|\psi_1\rangle$ shown in the inset of Fig. (2.2a) is similar to a uniform probability amplitude state $|+\rangle$.

Since reflection symmetry is the key point in the above analysis, it is not necessary for atoms to be periodically distributed to make the $|-\rangle$ state subradiant. In Fig. (2.2c), we allow half of the atoms to be distributed randomly, but in reflection symmetry with the other half. The population decay of $|-\rangle$ state is still substantially inhibited as shown in Fig. (2.2d). This is because the superradiant state $|\psi_1\rangle$ for random atomic distribution is still symmetric and has no overlap with the $|-\rangle$ state.

Generally, in the Dicke limit, we have one superradiant and $N-1$ subradiant eigenstates. Atomic distribution determines the symmetry of the superradiant state. By preparing atoms in an orthogonal state to this superradiant eigenstate, we can reach subradiance and store the photon. To release the photon, we can coherently change the state to have the same symmetry as the superradiant eigenstate and achieve a rapid readout [8].

2.4.2 Extended Sample

We could achieve subradiance in extended sample as well. For an extended spherical sample, we find [8] approximately decay rates $\Gamma_+^{\mathbf{k}_0} \cong \gamma[1+\frac{3}{8\pi}\frac{\lambda^2}{A}(N-1)]$ and $\Gamma_-^{\mathbf{k}_0} \cong \gamma[1-\frac{3}{8\pi}\frac{\lambda^2}{A}]$ for states $|\pm\rangle_{\mathbf{k}_0} = \sum_{j=1}^{N/2} e^{i\mathbf{k}\cdot\mathbf{r}_j}|j\rangle \pm \sum_{j=N/2+1}^{N} e^{-i\mathbf{k}\cdot\mathbf{r}_j}|j\rangle$, where λ is the transition wavelength, R is the radius of the atomic cloud and $A=\pi R^2$ is the cross section area. The "extra" γ in $\Gamma_+^{\mathbf{k}_0}$ is not important, as it is small compared to the leading term going as $\frac{3}{8\pi}\frac{\lambda^2}{A}N$. However the γ term in $\Gamma_-^{\mathbf{k}_0}$ is important. It seems like for the $|-\rangle_{\mathbf{k}_0}$ state, the single atom spontaneous decay rate is a lower decay limit for an extended sample. The good news however is that the collective spontaneous decay can also be mitigated by the spatial symmetry of the atomic distribution. In order to calculate the the evolution of

atomic system of a dense cloud of volume V , we use equation with exponential kernel [18]

$$\frac{\partial\beta(t,\mathbf{r})}{\partial t} = i\gamma \int d\mathbf{r}' n(\mathbf{r}') \frac{\exp(ik_0 |\mathbf{r}-\mathbf{r}'|)}{k_0 |\mathbf{r}-\mathbf{r}'|} \beta(t,\mathbf{r}'), \tag{2.27}$$

where $\beta(t,\mathbf{r})$ is the probability amplitude to find atom at position $\mathbf{r}$ excited at time t, $n(\mathbf{r})$ is the atomic density. Eq. (2.27) is valid in Markovian (local) approximation and is the continuous limit of Eq. (2.24). Eigenfunctions of Eq. (2.27) are $\beta(t,\mathbf{r}) = e^{-\Lambda t}\beta(\mathbf{r})$ and the eigenvalues Λ determine the evolution of the atomic system. Re(Λ) yields the state decay rate, while Im(Λ) describes frequency (Lamb) shift of the collective excitation. The eigenfunction equation for $\beta(\mathbf{r})$ reads

$$-i\gamma \int d\mathbf{r}' n(\mathbf{r}') \frac{\exp(ik_0 |\mathbf{r}-\mathbf{r}'|)}{k_0 |\mathbf{r}-\mathbf{r}'|} \beta(\mathbf{r}') = \Lambda\beta(\mathbf{r}). \tag{2.28}$$

We consider an infinitely long cylindrical shell of radius R and use cylindrical coordinates $\mathbf{r} = (\rho,\varphi,z)$. The atomic density is $n(\mathbf{r}) = n_0\delta(\rho - R)/2\pi R$, where n_0 is the number of atoms per unit length of the cylinder. For such geometry Eq. (2.28) reads

$$-\frac{i\gamma n_0}{2\pi} \int_0^{2\pi} d\varphi' \int_{-\infty}^{\infty} dz' K(\varphi-\varphi', z-z')\beta(\varphi',z') = \Lambda\beta(\varphi,z), \tag{2.29}$$

where

$$K(\varphi,z) = \frac{\exp[ik_0\sqrt{2R^2 - 2R^2 cos\varphi + z^2}]}{k_0\sqrt{2R^2 - 2R^2 cos\varphi + z^2}}.$$

We look for solution of Eq. (2.29) in the form

$$\beta(\varphi,z) = e^{in\varphi}e^{ik_z z}, \tag{2.30}$$

where n is an integer number and k_z is the wave number of the mode along the cylindrical axis z. Substituting Eq. (2.30) in Eq. (2.29) we obtain the following equation for eigenvalues Λ_n

$$\Lambda_n = -\frac{i\gamma n_0}{2\pi} \int_0^{2\pi} d\varphi' \int_{-\infty}^{\infty} dz' K(\varphi', z') e^{in\varphi'} e^{ik_z z'}. \tag{2.31}$$

Integrating over z' can be done by using the integral

$$\int_{-\infty}^{\infty} dz' \frac{exp[ik_0\sqrt{r^2+z'^2}]}{\sqrt{r^2+z'^2}} e^{ik_z z'} = i\pi H_0^{(1)}(r\sqrt{k_0^2-k_z^2}), \tag{2.32}$$

where $H_0^{(1)}(x)$ is the Hankel function. Then Eq. (2.31) reduces to

$$\Lambda_n = \frac{\gamma n_0}{2k_0} \int_0^{2\pi} d\varphi' H_0^{(1)}(R\sqrt{2-2\cos\varphi'}\sqrt{k_0^2-k_z^2}) e^{in\varphi'}. \tag{2.33}$$

The integration over φ' can be calculated using

$$\int_0^{2\pi} d\varphi' H_0^{(1)}(a\sqrt{2-2\cos\varphi'}) e^{in\varphi'} = 2\pi J_n(a) H_n^{(1)}(a), \tag{2.34}$$

and Eq. (2.33) leads to

$$\Lambda_n = \frac{\pi\gamma n_0}{k_0} J_n(R\sqrt{k_0^2-k_z^2}) H_n^{(1)}(R\sqrt{k_0^2-k_z^2}). \tag{2.35}$$

Hankel functions can be written as a combination of the Bessel functions of the first and the second kind as

$$H_n^{(1)}(x) = J_n(x) + iY_n(x), \tag{2.36}$$

which yields the following answer for the real and imaginary parts of the eigenvalues Λ_n

for $k_z \leq k_0$

$$\Gamma_n = \mathrm{Re}(\Lambda_n) = \frac{\pi\gamma n_0}{k_0} J_n^2(R\sqrt{k_0^2 - k_z^2}), \tag{2.37}$$

$$\Delta_n = \mathrm{Im}(\Lambda_n) = \frac{\pi\gamma n_0}{k_0} J_n(R\sqrt{k_0^2 - k_z^2}) Y_n(R\sqrt{k_0^2 - k_z^2}). \tag{2.38}$$

Eq. (2.37) shows that timed-Dicke state ($n = 0$ and $k_z = k_0$) $\beta(\varphi, z) = e^{ik_0 z}$ has the fastest decay rate $\mathrm{Re}(\Lambda_{\mathrm{TD}}) = \pi\gamma n_0/k_0$. However, collective Lamb shift for such state logarithmically diverges since $Y_0(x) \approx (2/\pi)\ln(x/2)$ for small x. For the states with $R\sqrt{k_0^2 - k_z^2} = A_{nl}$ where A_{nl} is lth zero of the Bessel function $J_n(x)$, such as the state $\beta_{n,k_z}(\varphi, z) = e^{in\varphi} e^{iz\sqrt{k_0^2 - A_{nl}^2/R^2}} \approx e^{i(k_0 - A_{nl}^2/2k_0R^2)z} e^{in\varphi}$, the decay rate and the collective Lamb shift vanish. In Fig. (2.3), we compare the decay of axially symmetric atomic states for continuous and discrete distribution of atoms on cylindrical surface. Namely, we plot the average decay rate $\bar{\Gamma} = -\gamma \ln P(1/\gamma)$ of the state $\beta_{0,k_z}(\phi, z) = e^{ik_z z}$, where $P(t)$ is the probability to find atoms excited, as a function of $R\sqrt{k_0^2 - k_z^2} - A_{01}$, where $A_{01} = 2.404$ is the first zero of $J_0(x)$. The average decay rate approaches zero when $R\sqrt{k_0^2 - k_z^2} = A_{01}$ for a discrete periodic atomic distribution shown in Fig. (2.3). This agrees with the analytical result in the continuous limit in Eq. (2.37) plotted as a dashed line. Cylindrical atomic distribution can be achieved, e.g., by adhering nano diamond with NV centers or SiV centers on a carbon tube.

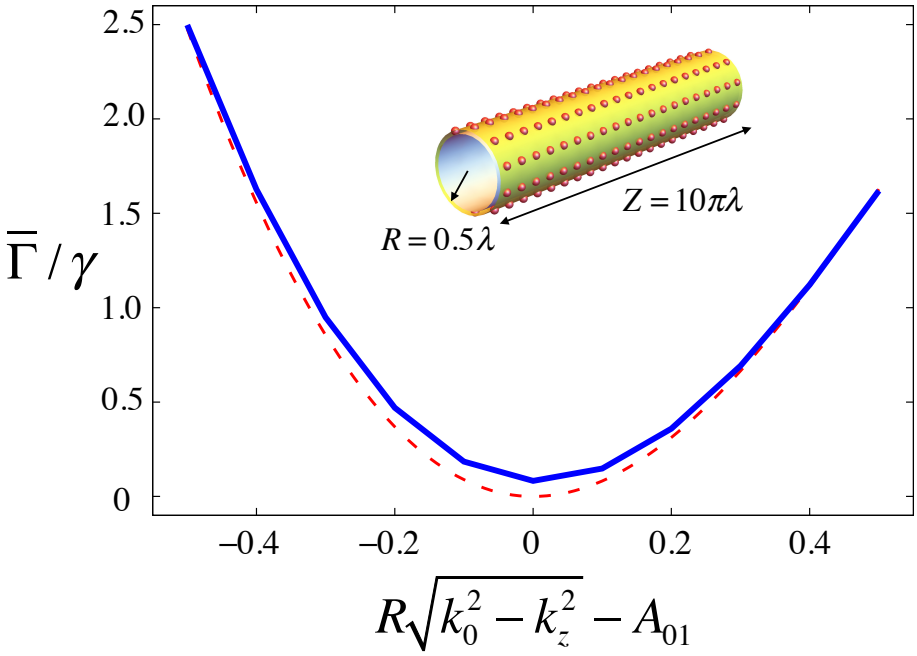

Figure 2.3: Solid line shows the average decay rate $\bar{\Gamma}$ of β_{0,k_z} state for periodic distribution of atoms on cylindrical surface sketched on the top. The cylinder consists of 1000 atoms in 100 layers with 10 atoms per each layer. Radius of the cylinder is $R = 0.5\lambda$ and the distance between adjacent layers is $0.1\pi\lambda$. Analytical result (2.37) for an infinitely long cylindrical shell with $100/\pi\lambda$ atoms per unit length is plotted as dashed line. The horizontal axis is deviation of the $R\sqrt{k_0^2 - k_z^2}$ from the root A_{01} of the Bessel function $J_0(x)$. $\bar{\Gamma} = -\gamma \ln[P(1/\gamma)]$ is defined as average decay rate for time scale of $1/\gamma$.

3.1 Interaction Hamiltonian

We show the lambda-type three-level which is usually used for the EIT in Fig. (3.1). We suppose the energy of the state $|i\rangle$ is ω_i ($i = e, g, m$). The states $|e\rangle$ and $|m\rangle$ are coupled by a strong field, and we weakly probe the optical susceptibility of the transition from $|g\rangle$ to $|e\rangle$. The coupling and probe field have the Rabi frequencies $\Omega_c = \mu_c E_c/\hbar$ and $\Omega_p = \mu_p E_p/\hbar$, E_i and μ_i denote the field strength and the induced dipole between the states, and ν_c and ν_p are the circular frequencies for the probe and coupling fields respectively. The coherence decay rates of ρ_{eg}, ρ_{em} and ρ_{mg} are defined as $\gamma_{eg} = (\Gamma_{eg} + \Gamma_{em})/2 + \gamma_e$, $\gamma_{em} = (\Gamma_{eg} + \Gamma_{em})/2 + \gamma_m$ and $\gamma_{mg} = \gamma_m$, where $\Gamma_{eg}(\Gamma_{em})$ is the spontaneous emission rate out of the state $|e\rangle$ to $|g\rangle(|m\rangle)$ and $\gamma_{e(m)}$ is the energy-conserving dephasing rate of the state $|e\rangle(|m\rangle)$ with respect to the ground state $|g\rangle$. The interaction Hamiltonian is (we set $\hbar = 1$)

$$H = \sum_i \omega_i \sigma_{ii} - \Omega_c e^{-i\nu_c t}\sigma_{em} - \Omega_p e^{-i\nu_p t}\sigma_{eg} + \text{H.c.}, \tag{3.1}$$

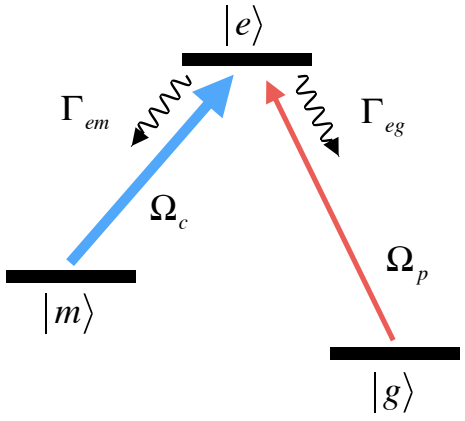

Figure 3.1: The atomic energy scheme of lambda-type EIT.

In the interaction picture, the field-atom coupling term is

$$\begin{aligned} V &= e^{iH_0t}He^{-iH_0t} - H_0, \\ &= \Delta_p\sigma_{ee} + \Delta_{2ph}\sigma_{mm} - \Omega_c\sigma_{em} - \Omega_p\sigma_{eg} + h.c., \end{aligned} \tag{3.2}$$

where $H_0 = \nu_p\sigma_{ee} + (\nu_p - \nu_c)\sigma_{mm}$, $\Delta_p = \omega_{eg} - v_p$, $\Delta_{2ph} = -\Delta_c + \Delta_p$, $\Delta_c = \omega_{em} - v_c$, $\omega_{eg}(\omega_{em})$ is the transition frequency between levels e and $g(m)$ and $\sigma_{ab} = |a\rangle\langle b|$. Plug the interaction Hamiltonian into the master equation, we find the equations of motion of the density matrix elements

$$\begin{aligned} i\dot{\rho}_{eg} &= (\Delta_p - i\gamma_{eg})\rho_{eg} - \Omega_p(\rho_{gg} - \rho_{ee}) - \Omega_c\rho_{mg}, \\ i\dot{\rho}_{em} &= (\Delta_c - i\gamma_{em})\rho_{em} - \Omega_c(\rho_{mm} - \rho_{ee}) - \Omega_p\rho_{gm}, \\ i\dot{\rho}_{mg} &= (\Delta_{2ph} - i\gamma_{mg})\rho_{mg} - \Omega_c\rho_{eg} + \Omega_p\rho_{me}, \end{aligned} \tag{3.3}$$

we look for the steady solution, i.e., $\dot{\rho} = 0$ and we assume that the Rabi frequency probe field is weak enough that most population is still in ground state $\rho_{gg} \approx 1$. The ρ_{eg} in the first order of Ω_p is obtained

$$\rho_{eg} = \frac{\Omega_p}{\Delta_p - i\gamma_{eg} - \frac{\Omega_c^2}{\Delta_{2ph} - i\gamma_{mg}}}. \tag{3.4}$$

The field induced polarization is

$$P = n\mathrm{Tr}[e\mathbf{r}\rho] = n\mu^*\rho_{ge} + n\mu\rho_{eg}, \tag{3.5}$$

where n is the atomic density. We need to work in Schrodinger picture and decompose the positive and negative frequency component [52], according to definition, we have nonlin-

earity χ for probe field as

$$\chi = \frac{P(t)}{\epsilon_0 E_p e^{-iv_p t}} = 3\pi\mathcal{N}\frac{\Gamma_{eg}}{\Delta_p - i\gamma_{eg} - \frac{\Omega_c^2}{\Delta_{2ph} - i\gamma_{mg}}}, \tag{3.6}$$

where $\mathcal{N}$ is the number of atoms in the volume $(\lambda_p/2\pi)^3$, λ_p is the transition wavelength between level $|e\rangle$ and $|g\rangle$, Γ_{eg} is calculated via Weisskopf-Wigner theory, as in Section 2.

3.2 Standing Wave-Coupled EIT and Coupled-Wave Equations

With a standing wave instead of a transient field coupling the states $|e\rangle$ and $|m\rangle$ in the EIT scheme, the probe field sees a spatial periodic modulated susceptibility. The periodicity leads to Bragg scattering of an incident probe light beam, lightwave propagation in such crystals becomes best described in terms of a photonic band structure with band gaps where light does not propagate, akin to the electronic band gaps in crystalline solids. Similar with Eq. (3.4), the coherence of standing-wave EIT is

$$\rho_{eg}(x) = \frac{\Omega_p}{\Delta_p - i\gamma_{eg} - \frac{(2\Omega_c \cos k_c x)^2}{\Delta_{2ph} - i\gamma_{mg}}}, \tag{3.7}$$

where we substitute the Rabi frequency of the transient coupling field Ω_c with the spatial modulated Rabi frequency of the standing wave $2\Omega_c \cos k_c x$. We can describe the fields and polarizations in slow envelope approximation, including components propagating forward and backward

$$\mathbf{E}(t,z) = e^{i\mathbf{k}_p\cdot\mathbf{r} - iv_p t}E_+(z) + e^{i\mathbf{k}_b\cdot\mathbf{r} - iv_p t}E_-(z), \tag{3.8}$$

$$\mathbf{P}(t,z) = e^{i\mathbf{k}_p\cdot\mathbf{r} - iv_p t}\epsilon_0\chi_+ E_+(z) + e^{i\mathbf{k}_b\cdot\mathbf{r} - iv_p t}\epsilon_0\chi_- E_-(z), \tag{3.9}$$

where $\mathbf{k}_b = -\mathbf{k}_p$ is the wavevector of the the backward field. The polarization is $\mathbf{P} = n\mu\rho_{eg}e^{i\mathbf{k}_p\cdot\mathbf{r}-i\nu_p t}$ and we have nonlinearity χ_+ for probe field E_+ as

$$\chi_+ = \frac{\mathbf{P}(x,t)}{\epsilon_0 E_+ e^{i\mathbf{k}_p\cdot\mathbf{r}-iv_p t}} = 3\pi\mathcal{N}\frac{\Gamma_{eg}}{\Delta_p - i\gamma_{eg} - \frac{(2\Omega_c\cos k_c x)^2}{\Delta_{2ph}-i\gamma_{mg}}} = \sum_n \chi^{(2n+1)}e^{-i2nk_c x}. \quad (3.10)$$

Near the phase matching condition $\Delta k = |\mathbf{k}_b - \mathbf{k}_p + \mathbf{k}_c - (-\mathbf{k}_c)| \ll k_p$, a two-mode approximation is justified, and now we consider the probe mode k_p and the 1st order Bragg-mode $-k_p$ generated by 3rd order nonlinearity $\chi(3)$, vise versa, the reflected $-k_p$ could also have feedback to probe mode k_p. As long as we stay in linear regime, i.e., excitation is very weak and most population is in ground state. The nonlinearity generated by probe (forward) and reflected (backward) field is additive. Analytic solution of the nonlinearity $\chi^{(2n+1)}$ is given in next section. Without consider virtual transition induced collective effect, the solution is symmetric for forward and backward fields. Due to the two mode approximation, we have

$$\chi_+ = \chi^{(1)} + \chi^{(3)}e^{-i2n\mathbf{k}_1\cdot\mathbf{r}}, \quad (3.11)$$

$$\chi_- = \chi^{(1)} + \chi^{(3)}e^{i2n\mathbf{k}_1\cdot\mathbf{r}}. \quad (3.12)$$

Then the polarization could be decomposed into two modes

$$\mathbf{P}(t,z) = e^{i\mathbf{k}_p\cdot\mathbf{r}-iv_p t}\epsilon_0\left(\chi_0 E_+ + \chi_{2n}e^{-i\Delta kx}E_-\right) + e^{i\mathbf{k}_b\cdot\mathbf{r}-iv_p t}\epsilon_0\left(\chi_0 E_- + \chi_{-2n}e^{i\Delta kx}E_+\right), \quad (3.13)$$

Plugging the electric field $\mathbf{E}(t,z)$ in Eq. (3.8) and polarization field $\mathbf{P}(t,z)$ in Eq. (3.9) to the Maxwell equation

$$\left(\frac{\partial^2}{\partial y^2} + \frac{\partial^2}{\partial x^2} - \frac{1}{c^2}\frac{\partial^2}{\partial t^2}\right)\mathbf{E} = \frac{1}{\epsilon_0 c^2}\frac{\partial^2}{\partial t^2}\mathbf{P}, \quad (3.14)$$

we can derive coupled wave equation by collecting the k_p and k_b mode from both sides of the equation. For k_p mode

$$[-k_p^2+(ik_p+i\frac{v_p}{c})\left(\frac{\partial}{\partial x}+\frac{1}{c}\frac{\partial}{\partial t}\right)]e^{i\mathbf{k}_p\cdot\mathbf{r}-iv_pt}E_+ = -\frac{v_p^2}{c^2}e^{i\mathbf{k}_b\cdot\mathbf{r}-iv_pt}\epsilon_0\left(\chi^{(1)}E_+ + \chi^{(3)}e^{-i\Delta kx}E_-\right), \tag{3.15}$$

it yields

$$\frac{\partial}{\partial x}E_+ = -\beta_0 E_+ + i\kappa e^{-i\Delta kx}E_-, \tag{3.16}$$

where $\beta_0 = \frac{v_p^2}{2k_pc^2}\mathrm{Im}\chi^{(1)}$ and $\kappa = \frac{v_p^2}{2k_pc^2}\chi^{(3)}$. Similarly, we have equation for $-k_p$ mode

$$\frac{\partial}{\partial x}E_- = \beta_0 E_- - i\kappa e^{i\Delta kx}E_+, \tag{3.17}$$

In order to solve the coupled mode equation, we introduce $\tilde{E}_+ = e^{i\Delta kx/2}E_+$ and $\tilde{E}_- = e^{-i\Delta kx/2}E_-$

$$\begin{aligned}\frac{\partial}{\partial x}\tilde{E}_+ &= -\beta\tilde{E}_+ + i\kappa\tilde{E}_-,\\ \frac{\partial}{\partial x}\tilde{E}_- &= \beta\tilde{E}_- - i\kappa\tilde{E}_+,\end{aligned} \tag{3.18}$$

where $\beta = \beta_0 - i\Delta k/2$. Solve the ODEs with boundary conditions $E_+(0) = \tilde{E}_+(0) = E_0$ and $E_-(L) = \tilde{E}_-(L) = 0$, we obtain the reflection R and transmission T of the probe field

$$R = \left|\frac{\kappa(e^{-\lambda L} - e^{\lambda L})}{(\beta-\lambda)e^{-\lambda L} - (\beta+\lambda)e^{\lambda L}}\right|^2, \tag{3.19}$$

$$T = \left|\frac{2\lambda}{(\beta-\lambda)e^{-\lambda L} - (\beta+\lambda)e^{\lambda L}}\right|^2, \tag{3.20}$$

where $\lambda = \sqrt{\beta^2+\kappa^2}$ and L is the sample length.

3.3 Analytic Solution of the Nonlinearity

The susceptibility of the standing-wave-coupled EIT is periodic by $2\pi/k$ in real space and can be expanded by it's Fourier component,

$$\chi(x) = 3\pi\mathcal{N}\frac{\Gamma_{bc}}{\Delta_p - i\gamma_{eg} - 2\Omega_c^2\frac{1+\cos 2kx}{\Delta_{2ph}-i\gamma_{mg}}} = \sum_m \chi^{(2m+1)}e^{-2mikx}. \tag{3.21}$$

Here we explicitly calculate the closed from of $\chi^{(2m+1)}$,

$$\begin{aligned}\chi^{(2m+1)} &= \frac{k}{\pi}\int_0^{\pi/k} dx e^{2mikx}\chi(x), \\ &= 3\pi\mathcal{N}\Gamma_{bc}\frac{1}{2\pi}\int_0^{\pi/k} d(2kx)\frac{e^{2mikx}}{p - \frac{1+\cos 2kx}{q}}.\end{aligned} \tag{3.22}$$

where $p = \Delta_p - i\gamma_{bc}$ and $q = (\Delta_{2ph} - i\gamma_{ac})/2\Omega_c^2$. In order to calculate the integral, we replace parameter x with $\theta = 2kx$ and introduce complex variable $z = e^{i\theta}$, then we have

$$\begin{aligned}d\theta &= -idz/z, \\ \cos\theta &= (z + 1/z)/2,\end{aligned} \tag{3.23}$$

the integral is written as

$$-i\oint dz\frac{z^{m-1}}{p - \frac{1+(z+z^{-1})/2}{h}} = i\oint dz\frac{2hz^m}{z^2 + 2(1-ph)z + 1} = i\oint dz\frac{2hz^m}{(z-\lambda_1)(z-\lambda_2)}, \tag{3.24}$$

for the determinator, we have two roots $\lambda_{1(2)} = -B \pm \sqrt{B^2 - 1}$ with $B = 1 - ph$. Since we have $\lambda_1\lambda_2 = 1$, we could assume$|\lambda_1| < 1$, in that way we only need to consider residue of $z = \lambda_1$ when $m \geq 0$, therefor it yields

$$i\oint dz\frac{2hz^m}{(z-\lambda_1)(z-\lambda_2)} = 2\pi\frac{2h\lambda_1^m}{(\lambda_2 - \lambda_1)}. \tag{3.25}$$

The upshot that we obtained is the first and third order nonlinearity

$$\chi^{(1)} = 3\pi\mathcal{N}\Gamma_{bc}\frac{2h}{(\lambda_2 - \lambda_1)}, \tag{3.26}$$

$$\chi^{(3)} = 3\pi\mathcal{N}\Gamma_{bc}\frac{2h\lambda_1}{(\lambda_2 - \lambda_1)}. \tag{3.27}$$

This closed form will be useful in the following sections when we use optical nonlinearity to observe novel topological phenomenon in quantum optical system.

4. LATTICE MODEL AND FLOQUET THEORY

4.1 Introduction to the Bloch Theory

The electrons in the crystal feel periodic potential. Without interaction between electrons, the dynamics of the electron in the presence of the lattice background is determined by the single particle Hamiltonian

$$H = \frac{P^2}{2m} + V(x), \tag{4.1}$$

where $V(x+a) = V(x)$. We define the discrete translation operator

$$T : x \to x + a, \tag{4.2}$$

which is commute with Hamiltonian H, i.e., $[T, H] = 0$. Assume the eigenstate $|\psi\rangle$ of H

$$H|\psi\rangle = E|\psi\rangle \tag{4.3}$$

where E is the eigenenergy. We can apply the translational operator T to both sides,

$$TH|\psi\rangle = H(T|\psi\rangle) = ET|\psi\rangle, \tag{4.4}$$

in the non-degenerate case, $T|\psi\rangle = |\psi(x+a)\rangle$ must be the same state with $|\psi(x)\rangle$ only with a phase factor $e^{i\phi}$. Along with the periodic boundary condition, we have the relation

$$|\psi(x+Na)\rangle = e^{iN\phi}|\psi(x)\rangle = |\psi(x)\rangle, \tag{4.5}$$

the phase factor is $\phi = \frac{2\pi}{N}n$, $n = 0, 1...N-1$. We are ready to show that the eigenstate of the Hamiltonian is the Bloch waves

$$|\psi_q(x)\rangle = e^{iqx}|u(x)\rangle. \tag{4.6}$$

Here $q = nb/N$, $n = 0, 1...N-1$, $b = 2\pi/a$ is the reciprocal lattice constant, and $|u\rangle$ is a spatial periodic function with the same periodicity as the lattice, i.e., $|u(x+a)\rangle = |u(x)\rangle$.

4.2 Nearly Free Electron Approximation

In the weak binding (nearly free electron) approximation, we assume that the periodic potential V is sufficiently weak so that the electrons behave as if they were free and the potential could be treated in perturbation theory. According to the Bloch theory, the ansatz wavefunction of the eigenstate is

$$|\psi_q\rangle = \sum_n c_n|q+nb\rangle. \tag{4.7}$$

where $|q+nb\rangle$ is the wavefunction of the free electron with momentum $q+nb$ and n is integer. Plug the ansatz (4.7) into Schrödinger Equation $H\psi_q = \epsilon(q)\psi_q$

$$\begin{pmatrix} ... & & & & \\ & \frac{\hbar^2(q+b)^2}{2m} & \langle q+b|V|q\rangle & \langle q+b|V|q-b\rangle & \\ & \langle q|V|q+b\rangle & \frac{\hbar^2q^2}{2m} & \langle q|V|q-b\rangle & \\ & \langle q+b|V|q-b\rangle & \langle q-b|V|q\rangle & \frac{\hbar^2(q-b)^2}{2m} & \\ & & & & ... \end{pmatrix} |\psi_q\rangle = \epsilon(q)|\psi_q\rangle, \tag{4.8}$$

where $\langle k|V|k'\rangle = \int_{BZ} dx V e^{i(k-k')x}$. We obtain the dispersion relation ϵ for q in the first Brillouin zone (BZ). Since the potential is much weaker than the unit kinetic energy, i.e. $\langle k|V|k'\rangle \ll \hbar^2q^2/2m$, in the weak binding approximation, the eigenstate is almost the

free particle state except near the degenerate points, e.g., $|q+b\rangle$ and $|q\rangle$ at $q=-b/2$ and $|q+b\rangle$ and $|q-b\rangle$ at $q=0$. Typical band gaps are formed at the degenerate points of the free particle states.

4.3 Tight-Binding Model

In order to study the details of the band structure, we can use the tight-binding approximation which captures rich physics and gives good qualitative results in many cases. Since the electrons in the crystal is tightly bound to the atom to which they belong because of the atomic strong attractive potential, the localized bound orbital level in each atom is the unperturbed basis in this approach, . For the sake of simplicity, we only consider one orbital in each atom and denote the wavefunction of the orbital state in nth site at position $x=na$ by $\phi_n(x)=\langle x|n\rangle$. Since the wavefunction of state $|n\rangle$ is the same as the one of $|n\pm1\rangle$ if we have a spatial translation by $\pm a$, we have the relation

$$\phi_n(x)=\phi_{n\pm1}(x\pm a). \tag{4.9}$$

The interaction (it is the kinetic energy here) between the orbitals in neighborhood sites can be discretized

$$\begin{aligned}\frac{p_x^2}{2m}\phi(x) &= -\frac{\hbar^2}{2m}\frac{\partial^2}{\partial x^2}\phi(x),\\ &\approx -\frac{\hbar^2}{2ma^2}[\phi(x+a)+\phi(x-a)-2\phi(x)],\end{aligned} \tag{4.10}$$

it means that the kinetic energy term $K=P^2/2m$ introduce the "hopping" from nearest neighbor (NN) sites in the first order approximation, the hopping constant is defined as

$$t=-\langle n|K|n\pm1\rangle=\frac{\hbar^2}{2ma^2}. \tag{4.11}$$

The last term in the right side of Eq. (4.10) shifts the total energy by a constant and has no other physical contribution (which can be ignored if we are not interested in the total energy). Therefore in the basis of tight-binding states, Eq. (4.1) is

$$H = \sum_n -(t_n c_{n+1}^\dagger c_n + t_n^* c_n^\dagger c_{n+1}) + \sum_n V_n c_n^\dagger c_n, \tag{4.12}$$

where $c_n(c_n^\dagger)$ is the annihilation (creation) operator of the electrons in the nth site.

4.3.1 One-Band Model

Let's consider the simplest 1D lattice with only one type of atoms, $V_n = V$. The last term $\sum_i V_i c_i^\dagger c_i = V \sum_i \hat{n}_i = VN$, which is a constant, can be safely ignored. As we did in Eq. (4.10), we assume the electrons can only hop to the nearest neighbor and t is must be the same for all sites due to the translational symmetry. We also assume the t is real (, which is generally true for the hopping-only models and can introduce profound phenomenon if being complex, as shown in Section 6 and afterwards). The Hamiltonian is simplified to

$$H = -t \sum_n c_{n+1}^\dagger c_n + h.c.. \tag{4.13}$$

Fourier transformation is applied from real space site to a k-space in 1st Brillouin zone (BZ)

$$\begin{aligned} c_n &= \frac{1}{\sqrt{N}} \sum_k c_k e^{ikx_n}, \\ c_k &= \frac{1}{\sqrt{N}} \sum_n c_n e^{-ikx_n}. \end{aligned} \tag{4.14}$$

where $k = -\frac{\pi}{a}, -\frac{\pi}{a} + 1 \times \frac{2\pi}{Na}, -\frac{\pi}{a} + 2 \times \frac{2\pi}{Na} ... \frac{\pi}{a}$. The Hamiltonian in k-space :

$$H = \sum_k \epsilon_k c_k^\dagger c_k, \tag{4.15}$$

where the dispersion relation is $\epsilon_k = -2t\cos ka$, we only have one band.

4.3.2 Two-band Theory

This 1D lattice model contains two type of atoms in a unit cell. The Hamiltonian is

$$H = -t\sum_n (a_n^\dagger b_n + b_n^\dagger a_{n+1} + h.c.) + V_a \sum_n a_n^\dagger a_n + V_b \sum_n b_n^\dagger b_n. \tag{4.16}$$

Position of $a(b)$ type atom in the nth unit cells are $R_{n,a(b)} = an + r_{a(b)}$. Fourier transformation is applied

$$\begin{aligned} a_n &= \frac{1}{\sqrt{N}}\sum_k a_k e^{ikR_{n,a}}, \\ a_k &= \frac{1}{\sqrt{N}}\sum_n a_n e^{-ikR_{n,a}}, \\ b_n &= \frac{1}{\sqrt{N}}\sum_k b_k e^{ikR_{n,b}}, \\ b_k &= \frac{1}{\sqrt{N}}\sum_n b_n e^{-ikR_{n,b}}. \end{aligned} \tag{4.17}$$

We obtain $\sum_n a_n^\dagger b_n = \sum_k a_k^\dagger b_k e^{ika/2}$, $\sum_n b_n^\dagger a_{n+1} = \sum_k b_k^\dagger a_k e^{-ika/2}$, and $\sum_n a_n^\dagger a_n = \sum_k a_k^\dagger a_k$ with the assumption that $r_a - r_b = a/2$. Therefore the Hamiltonian in k-space is

$$H = -\sum_k 2t\cos\frac{ka}{2}(a_k^\dagger b_k + h.c.) + V_a a_k^\dagger a_k + V_b b_k^\dagger b_k, \tag{4.18}$$

it is convenient to write the two-band model into a 2-by-2 matrix in the k-space

$$H = \sum_k \begin{pmatrix} a_k^\dagger & b_k \end{pmatrix} \mathcal{H}(k) \begin{pmatrix} a_k \\ b_k \end{pmatrix}, \tag{4.19}$$

where

$$\mathcal{H}(k) = \begin{pmatrix} V_a & -2t\cos\frac{ka}{2} \\ -2t\cos\frac{ka}{2} & V_b \end{pmatrix} \tag{4.20}$$

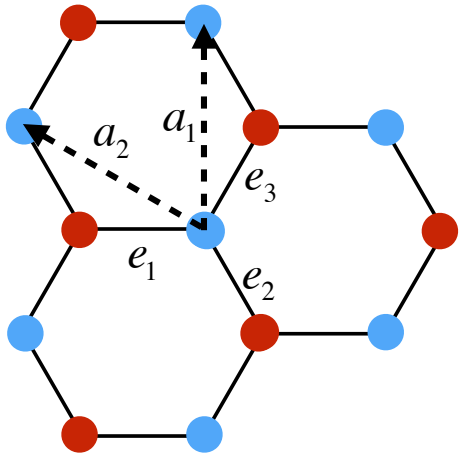

Figure 4.1: The tight-binding model of graphene, each unit cell, defined by the lattice vectors $\mathbf{a}_1$ and $\mathbf{a}_2$, contains two different sublattices, marked by a and b sites. There are three NN interaction along $\mathbf{e}_i$, $i = 1, 2, 3$.

is a Hermitian matrix as a function of k. It is called the Kernel of the Hamiltonian. It contains all the physical information of the corresponding Hamiltonian, but it is NOT a Hamiltonian. However, it is usually called a Hamiltonian in the literature and we will not distinguish them from now on. The dispersion relation for the two bands is obtained by diagonalizing $H(k)$,

$$\epsilon_{k,\pm} = \frac{V_a + V_b}{2} \pm \sqrt{(2t\cos\frac{ka}{2})^2 + (\frac{V_c - V_b}{2})^2}. \tag{4.21}$$

4.3.3 Graphene

Many amazing properties of graphene come from the linear dispersion relation of electron at low energies. The electrons can be described by an equation that is formally equivalent to the massless Dirac equation. This linear dispersion relation is readily derived from two band tight-binding model in Fig. (4.1).

In the graphene, there two sites per unit cell, i.e., two sublattices, red (black) dot is the a (b) type carbon atom. The 2D lattice vectors are $\mathbf{a}_1 = a(\sqrt{3}, 0)$ and $\mathbf{a}_2 = a(-\sqrt{3}/2, 3/2)$.

We only consider the NN interaction, the Hamiltonian is

$$H_{NN} = -t \sum_{\langle i,j \rangle} a_i^\dagger b_j + h.c. \tag{4.22}$$

where $\langle i, j \rangle$ means the pair of the nearest neighbor sites. Since there are three different NN bonds along $\mathbf{e}_i$:$\mathbf{e}_1 = a(-1, 0)$, $\mathbf{e}_2 = a(1/2, -\sqrt{3}/2)$ and $\mathbf{e}_3 = a(1/2, \sqrt{3}/2)$, the Hamiltonian is explicitly written as

$$H_{NN} = -t \sum_i (a^\dagger_{\mathbf{r}_i} b_{\mathbf{r}_i + \mathbf{e}_1} + a^\dagger_{\mathbf{r}_i} b_{\mathbf{r}_I + \mathbf{e}_1} + a^\dagger_{\mathbf{r}_i} b_{\mathbf{r}_i + \mathbf{e}_1}) + h.c. \tag{4.23}$$

where the summation $\sum_i$ sums over all the unit cells while $\mathbf{r}_i$ is the position of the a-type atom in each cell. Apply the 2D Fourier transformation, we obtain the Hamiltonian in k-space

$$H_{NN}(\mathbf{k}) = \begin{pmatrix} 0 & H_{12}(\mathbf{k}) \\ H_{21}(\mathbf{k}) & 0 \end{pmatrix}, \tag{4.24}$$

where the non-diagonal element $H_{12} = H_{21}^* = -t \sum_{j=1}^{3} e^{-i\mathbf{k}\cdot\mathbf{e}_j}$. Diagonalization of the matrix H gives the eigenvalues

$$\epsilon_\pm(\mathbf{k}) = \pm |t| \sqrt{3 + 2\cos(\sqrt{3}k_x a) + 4\cos(\frac{\sqrt{3}}{2}k_x a)\cos(\frac{3}{2}k_y a)}. \tag{4.25}$$

Both the the upper band ϵ_+ and the lower band ϵ_- reach to 0 when k reaches $\mathbf{K}_1 = \frac{4\pi}{3\sqrt{3}}(\frac{\sqrt{3}}{2}, \frac{1}{2})$, $\mathbf{K}_2 = \frac{4\pi}{3\sqrt{3}}(-\frac{\sqrt{3}}{2}, -\frac{1}{2})$. In the whole BZ except that the corners, upper band has positive energy $\epsilon_+ > 0$ and the lower band has negative energy $\epsilon_- < 0$. However the two bands are degenerate at $\mathbf{K}_i$. The non-diagonal element and dispersion relation can be expanded near the corners,

$$H_{12}(\mathbf{K}_1 + \mathbf{q}) = \frac{3}{2} t a e^{i5\pi/6}(q_x + iq_y), \tag{4.26}$$

$$H_{12}(\mathbf{K}_2 + \mathbf{q}) = \frac{3}{2} t a e^{i\pi/6}(q_x - iq_y), \tag{4.27}$$

$$\epsilon_{\pm}(\mathbf{K}_{1(2)} + \mathbf{q}) = \pm \frac{3}{2} |t| \, aq + O(q^2), \tag{4.28}$$

where $\mathbf{q} = \mathbf{k} - \mathbf{K}_i$ and $q = |\mathbf{q}|$. In Eq. (4.28), linear dispersion relation is obtained near $\epsilon = 0$ (i.e., the low energy excitation regime).

4.4 Floquet (Temporal Periodic) Hamiltonian

Driven quantum system is intensively used in the later sections to generate novel topological effect in quantum optics. In order to capture the details of the quantum systems that are exposed to explicit time-dependent external fields, we make a list to compare the temporal periodic Hamiltonian with the spatial one. There are many similarities between the two so that we utilize the method well developed in the Bloch theorem to understand the dynamics of the Floquet system.

	Spatial	Temporal
Hamiltonian	$H(x + a) = H(x)$	$H(t + T) = H(t)$
Bloch theory	$\psi(x) = e^{iqx}u; u(x + a) = u(x)$	$\varphi(t) = e^{-i\varepsilon t}u; u(t + T) = u(t)$
Brillouin zone	quasimomentum $q \in (-\pi/a, \pi/a)$	quasienergy $\varepsilon \in (-\pi/T, \pi/T)$

Table 4.1: The corresponding elements in spatial and temporal periodic system are compared

5. SUPERRADIANCE LATTICE

5.1 Introduction of Superradiance Lattice

5.1.1 Timed-Dicke state and Directional Emission

Consider a single photon with wavevector $\mathbf{k}_p$ absorbed by a N-atom ensemble, the Hamiltonian in the interaction picture (with the $-E \cdot r$ gauge) is

$$V_p = \sum_j \hbar g \sigma_j^+ a e^{i\mathbf{k}_p \cdot \mathbf{r}_j} e^{-i(\nu-\omega)t} + h.c. \tag{5.1}$$

where $\sigma_j^+ = |e_j\rangle\langle g_j|$ is the atomic transition operator, a is the photon annihilation operator, $\nu(\omega)$ is the frequency of the incident radiation (atomic transition of two atomic levels e and g), and g is the coupling constant. We define the states

$$|G\rangle = |g_1 ... g_N\rangle \otimes |1\mathbf{k}_p\rangle, \tag{5.2}$$

$$|e_{\mathbf{k}_p}\rangle = \frac{1}{\sqrt{N}} \sum_j e^{i\mathbf{k}_p \cdot \mathbf{r}_j} |e_j\rangle, \tag{5.3}$$

where $|G\rangle$ is the collective ground state and $|e_{\mathbf{k}_p}\rangle$ is the TDS [7] generated by a photon incidence with $\mathbf{k}_p$ wavevector. In order to study the direction of the spontaneous emission, we calculate the matrix element of interaction Hamiltonian between the timed-Dicke state $|e_{\mathbf{k}_p}\rangle$ and atomic ground state with a $\mathbf{k}$ wavevector photon being emitted $|G; 1\mathbf{k}\rangle$.

$$\begin{aligned} \langle G; 1\mathbf{k}|V|e_{\mathbf{k}_p}\rangle &\propto \frac{1}{\sqrt{N}} \sum_j e^{i(\mathbf{k}_p - \mathbf{k}) \cdot \mathbf{r}_j}, \\ &\propto \frac{(2\pi)^3 \sqrt{N}}{V} \delta^3(\mathbf{k}_p - \mathbf{k}), \end{aligned} \tag{5.4}$$

with V being the volume of the gas. Thus, the emitted photon is directed along the exciting photon. The directional emission can be understood that the phase match condition is fulfilled by the atomic correlation and the vacuum mode with the same wavevector of the exciting photon, i.e., $\mathbf{k} = \mathbf{k}_p$.

The Hamiltonian in Eq. (5.1) can be rewritten

$$V_p = \hbar\sqrt{N}g|e_{\mathbf{k}_p}\rangle\langle G|ae^{-i(\nu-\omega)t} + h.c. \tag{5.5}$$

The cooperative interaction between N-atom and the single photon behaves like a two-level system interaction with the incident field. When the size of the atomic sample approaches infinity, N-atoms can always reabsorb the directional emitted photon. Therefore the dynamics of the system yields a Rabi oscillation with the effective Rabi frequency $\Omega = \hbar\sqrt{N}$g [17], which has a factor of $\sqrt{N}$ enhancement with respect to an isolated single atom interaction with a single photon.

5.1.2 Generalized TDS

With the help of an ancillary atomic level m in Fig. (3.1), the system can be driven from $|e_{\mathbf{k}_p}\rangle$ to the generalized TDS. The concept of TDS is generalized from its origin [7], it is a single-excitation N-atom state $|\sigma_{\mathbf{k}}\rangle$ ($\sigma = e, m$) with a quasimomentum $\mathbf{k}$. If the driving field coupling level m and e has the wavevector $\mathbf{k}_1$ and π pulse area, its phase $e^{-i\mathbf{k}_1\cdot\mathbf{r}}$ is imprinted onto the atomic phase correlation upon stimulated emitting a photon into the mode of the driving field.

$$|e_{\mathbf{k}_p}\rangle \rightarrow |m_{\mathbf{k}_p-\mathbf{k}_1}\rangle = \frac{1}{\sqrt{N}}\sum_j e^{i(\mathbf{k}_p-\mathbf{k}_1)\cdot\mathbf{r}_j}|e_j\rangle, \tag{5.6}$$

By applying a π pulse with a different wavevector $\mathbf{k}_2$ to drive system from m to e, the photon absorption leads to a contribution of the conjugate phase $e^{i\mathbf{k}_2\cdot\mathbf{r}}$

$$|m_{\mathbf{k}_p-\mathbf{k}_1}\rangle \rightarrow |e_{\mathbf{k}_p-\mathbf{k}_1+\mathbf{k}_2}\rangle = \frac{1}{\sqrt{N}}\sum_j e^{i(\mathbf{k}_p-\mathbf{k}_1+\mathbf{k}_2)\cdot\mathbf{r}_j}|e_j\rangle. \tag{5.7}$$

The pulse manipulations can be done many times within the atomic decoherence time. By implementing the interaction of any two levels in the context with Raman configuration, the decoherence time is proved to be as long as 1 minute in solid [60]. One remark is that state $|e_{\mathbf{k}}\rangle$ does not have directional emission nor superradiance provided that $|\mathbf{k}| \neq \omega/c$. Second remark is that recoil motion of the atoms can be ignored by fixing the atomic system in solids, since the Lamb-Mossbauer effect [61, 62] yields an infinite mass of the atoms.

5.1.3 Standing-Wave EIT

Replacing the π pulses sequence with two counter-propagating coherent field with the wavevectors $\mathbf{k}_1$ and $\mathbf{k}_2 = -\mathbf{k}_1$, we can write the interaction Hamiltonian

$$V_s = -\sum_j \hbar(\Omega_1 e^{i\mathbf{k}_1\cdot\mathbf{r}_j} + \Omega_2 e^{-i\mathbf{k}_1\cdot\mathbf{r}_j})|e_j\rangle\langle m_j| + h.c.. \tag{5.8}$$

We define the creation operators

$$\begin{aligned} e_n^\dagger &= \tfrac{1}{\sqrt{N}}\textstyle\sum_n e^{i(\mathbf{k}_p+2n\mathbf{k}_1)\cdot\mathbf{r}_j}|e_j\rangle\langle g_j|, \\ m_n^\dagger &= \tfrac{1}{\sqrt{N}}\textstyle\sum_n e^{i[\mathbf{k}_p+(2n-1)\mathbf{k}_1]\cdot\mathbf{r}_j}|m_j\rangle\langle g_j|. \end{aligned} \tag{5.9}$$

with the superradiant states $|e_{\mathbf{k}_p}\rangle = e_0^\dagger|G\rangle$. Upon the transformation, the Hamiltonian in Eq. (5.8) can be rewritten into a tight-binding form

$$V_s = -\sum_n \hbar\Omega_1 e_n^\dagger m_n + \hbar\Omega_2 m_{n+1}^\dagger e_n + h.c.. \tag{5.10}$$

The Hamiltonian in Eq. (5.10) is also valid for few excitation if the excitation number is much less than the atom number, as long as the operators are approximately bosonic. The commutation relation of these operators are

$$\begin{aligned}
[e_n, e_{n'}^\dagger] &= \frac{1}{N}\sum_j e^{-2i(n-n')\mathbf{k}_1\cdot\mathbf{r}_j}(|g_j\rangle\langle g_j| - |e_j\rangle\langle e_j|), \\
[m_n, m_{n'}^\dagger] &= \frac{1}{N}\sum_j e^{-2i(n-n')\mathbf{k}_1\cdot\mathbf{r}_j}(|g_j\rangle\langle g_j| - |m_j\rangle\langle m_j|), \\
[e_n, m_{n'}^\dagger] &= 0.
\end{aligned} \tag{5.11}$$

under the EIT condition $\Omega_1, \Omega_2 \gg \Omega_p$ (we replace the single photon in the probe mode with a weak coherent field with the Rabi frequency Ω_p, forming a λ-scheme EIT), the population are mainly in the ground state $|g\rangle$, $\mathrm{Tr}(\rho|g_j\rangle\langle g_j||) \approx 1$, $\mathrm{Tr}(\rho|e_j\rangle\langle e_j|) \approx 0$, and $\mathrm{Tr}(\rho|m_j\rangle\langle m_j|) \approx 0$. Therefore, we obtain

$$\begin{aligned}
[e_n, e_{n'}^\dagger] &= \delta_{nn'}, \\
[m_n, m_{n'}^\dagger] &= \delta_{mm'}.
\end{aligned} \tag{5.12}$$

Eq. (5.10) is exactly the same form with Eq. (4.16). This lattice, named Superradiance Lattice (SL), is formally a two band tight-binding model. The corresponding elements of the two models are compared in Table. (5.1)

	SL	two-band superlattice
lattice space	momentum space	position space
reciprocal space	position space	momentum space
lattice site	TDS $\|e_\mathbf{k}\rangle, \|m_\mathbf{k}\rangle$	atomic orbital
coupling	Ω Rabi frequency	t hopping constant

Table 5.1: The corresponding elements in SL and two-band superlattice are compared

The tight-binding model in momentum space is diagonal in the reciprocal space of k-space, i.e., position space. The dispersion relation is, according to Eq. (4.21),

$$\varepsilon_{\pm}(\mathbf{r}) = \pm 2\hbar\Omega \cos(\mathbf{k}_1 \cdot \mathbf{r}), \tag{5.13}$$

where we let $\Omega_1 = \Omega_2 = \Omega$ for simplicity. This result can be obtained directly from the interference pattern of the coupling standing wave in position space. Besides the dispersion relation, SL is able to reproduce many well known phenomenons, e.g., the Wannier-Stark ladder, dynamics band collapsing [49], making it a promising new platform to test novel and rich physics in modern condensed matter physics.

5.2 Experimental Demonstration

We measure the quantum transportation in a one-dimensional (1D) SL of a Bose-Einstein condensate (BEC) based on a configuration of standing-wave EIT. Resonantly excited to a superradiant state, the BEC is further transported to other collective excited states, which form a 1D SL, by the two coupling fields of the EIT. The directional emission of one of the superradiant excited state in the 1D SL is measured. The quantum transportation depends on the band structure in Eq. (5.13), which can be controlled by the frequency and intensity of the standing-wave coupling laser fields.

5.2.1 Experimental Scheme

The experiment is arranged as following such that the transportation of the excitation in the BEC can be measured. We use a weak probe pulse to pump the ground state BEC into the state $|e_0\rangle$, which is further transported to other states in the superradiance lattice via the coupling fields. The wavevectors of the coupling fields are arranged such that the state $|e_1\rangle$ satisfies the requirement of superradiance radiation, $|\mathbf{k}_1| = |\mathbf{k}_p|$, as shown in Fig. (5.1a). This superradiance radiation is detected and its difference from the ordinary Bragg

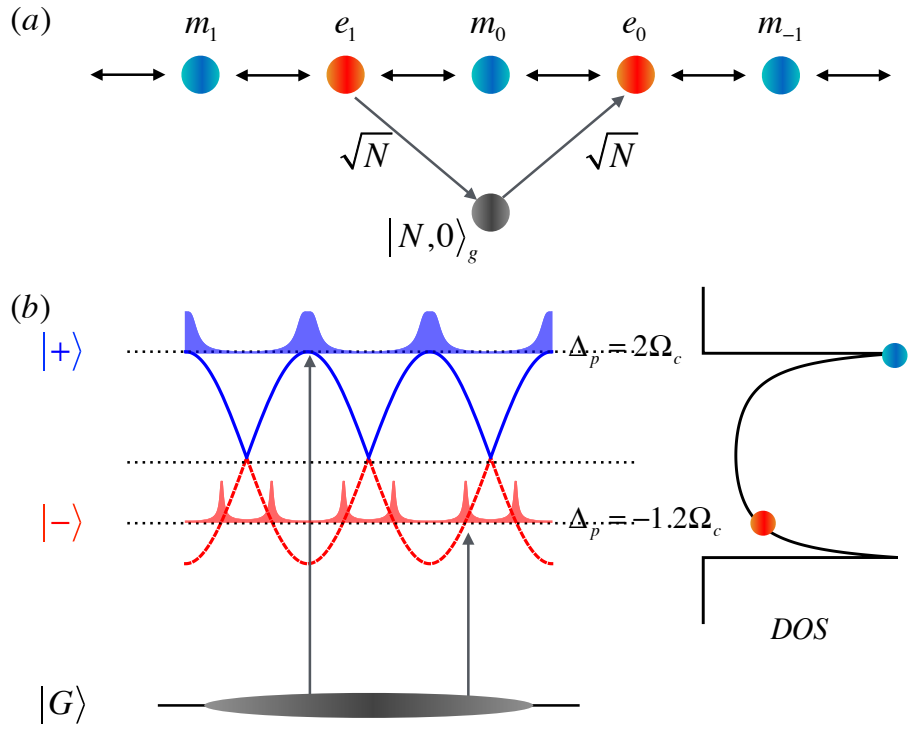

Figure 5.1: Band structure of the superradiance lattice in BEC.(a) In the picture of the superradiance lattice, the pump laser populates $|e_0\rangle$, which is further connected to other TDSs. Among these states, only $|e_1\rangle$ is superradiantly coupled to the ground states and its directional emission is measured in the experiments. (b) The atoms dressed by the standing wave have different energies of their eigenstates $|\pm\rangle = (|e\rangle \pm |m\rangle)\sqrt{2}$ at different positions. The excitation probabilities of the BEC atoms at different positions is plotted for two different pump frequencies. The total excitation probabilities are proportional to the density of states of a tight-binding model of collectively excited states.

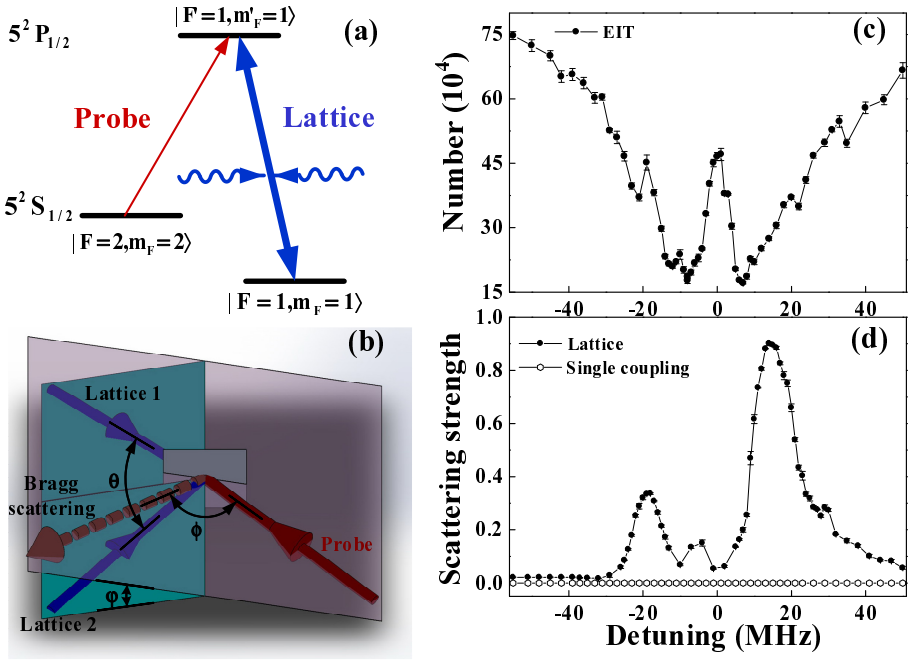

Figure 5.2: Experimental configuration of the 1D superradiance lattice in BEC. (a) Energy diagram of the $5^2S_{1/2} - 5^2P_{1/2}$ transition of ^{87}Rb. A pair of strong coupling laser beams form a 1D optical lattice and drive the transition between $|e\rangle = |F' = 1, m'_F = 1\rangle$, $|m\rangle = |F = 1, m_F = 1\rangle$. The weak probe light drives the transition between the ground state $|g\rangle = |F = 2, m_F = 2\rangle$ and excited state $|e\rangle$. Atoms are initially prepared in the free reservoir spin state $|g\rangle$. (b) The experimental geometry and the laser configuration. There are three planes, the plane of the two coupling beams, the plane of the probe-superradiant beams, and the equal intensity plane of the coupling beams. (c) EIT spectrum for remaining the atoms with only one coupling laser and probe light. The power of the coupling laser is 200 μW and on resonance ($\Delta_c = 0$). The power of the probe light is 25 μW. (d) Superradiant spectra with a pair of coupling beams. Each of the coupling laser is 200 μW and the other parameters are the same as in (c).

scattering and four-wave-mixing will be discussed later.

A pure BEC with typically 5×10^5 ^{87}Rb atoms is prepared in the $|g\rangle \equiv |F = 2, m_F = 2\rangle$ hyperfine ground state sublevel confined in a cross-beam dipole trap at a wavelength near 1064 nm. The geometric mean of trapping frequencies is $\overline{\omega} \simeq 2\pi \times 80$ Hz. The atomic size is estimated in the Thomas-Fermi regime to be 20 μm, when the scattering length for $|g\rangle$ state at zero magnetic field is about $100a_0$. The D_1 line (around 795 nm) of ^{87}Rb atom is considered as a simple three-level Λ-type model as shown in Fig. (5.2a) due to the large hyperfine splitting of 816.8 MHz between the two excited states. We choose the other two relevant hyperfine levels $|e\rangle \equiv |F' = 1, m'_F = 1\rangle$, $|m\rangle \equiv |F = 1, m_F = 1\rangle$. A homogeneous bias magnetic field along the z axis (gravity direction) is provided with $B_0 = 2$ G by a pair of coils operating in the Helmholtz configuration. A pair of strong coupling laser beams with the intersecting angle $\theta = 124^o$ drive the transition between $|e\rangle$ and $|m\rangle$, as shown in Fig. (5.2b). The coupling laser beams have the waist ($1/e^2$ radius) about 280 μm at the atom position. The standing wave pattern formed by the coupling fields have about 50 layers in the atomic gases. The weak light used to pump the atoms from $|g\rangle$ to $|e\rangle$ has a waist about 600 μm. The coupling and probe lasers illuminate atoms simultaneously with 80 μs. The intersecting angle between the superradiant emission and the incident pumping light is about $\phi \sim 180^o - \theta = 56^o$. In order to obtain the dark background and high signal-noise ratio for detecting the superradiant emission, the intersecting angle between the plane of the two coupling beams and the plane of the pump-superradiant beams is $\varphi = 11^o$, as shown in Fig. (5.2b). The resulting superradiant emission is measured with EMCCD.

If we only have one coupling laser, the two states $|e_0\rangle$ and $|m_0\rangle$ and the ground state form an EIT configuration, which is measured as shown in Fig. (5.2c). Since the probe (pump) beam has a waist much larger than the coupling beam and the size of the BEC, we measure the remaining atoms by the time flight absorption image after turning on the

coupling and probe pulse for 80 μs, rather than directly measure the absorption through the transmitted probe beam. The frequency of the probe beam is swept through resonance while the frequency of the pump beam is fixed on resonance $\Delta_c = 0$. Fig. (5.2c) shows the EIT spectrum for the remaining atoms with a transparency window at the centre. As a comparison to the latter experiment with two coupling beams, the superradiant emission in this case is measured to be zero, as shown in Fig. (5.2d) (circle point). In contrast, Fig. (5.2d) (solid dot) shows a typical superradiant emission when we have two coupling lasers. Two peaks characterized by the density of states (DOS) of the 1D tight-binding lattice (see Fig. (5.1a)) were observed.

5.2.2 Theoretical Model

A two-level system with states $|e\rangle$ and $|m\rangle$ coupled by a standing wave has two important parameters, the Rabi frequency Ω=$\mu E/\hbar$ with E the electric field amplitude of the coupling laser and μ the transition dipole moment, the single photon recoil energy $E_r = \hbar^2 Q^2/2m$ where $\hbar Q = 2\pi\hbar/\lambda_0$ is the single photon recoil momentum and λ_0 is the atomic transition wavelength. The Hamiltonian includes two parts, $H = K + V$, where $K = \hbar^2 k^2/2m$ is the recoil energy and $V = 2\Omega \cos Qx|e\rangle\langle m| + h.c.$ is the interaction Hamiltonian. From simplicity, the momentum is denoted in unit of Q. Due to the spatial periodicity of the coupling fields, the Hamiltonian can be written in the Bloch basis of

$|k+2n\rangle_m$and $|k+(2n+1)\rangle_e$ where n is an integer,

$$H = \Psi^+ \begin{pmatrix} \dots & \Omega & & & & & & \\ \Omega & E_r(k-2)^2 & \Omega & & & & & \\ & \Omega & E_r(k-1)^2 & \Omega & & & & \\ & & \Omega & E_r k^2 & \Omega & & & \\ & & & \Omega & E_r(k+1)^2 & \Omega & & \\ & & & & \Omega & E_r(k+2)^2 & \Omega & \\ & & & & & \Omega & \dots & \end{pmatrix} \Psi, \tag{5.14}$$

where $\Psi^\dagger = (\dots |k-2\rangle_m, |k-1\rangle_e, |k\rangle_m, |k+1\rangle_e, |k+2\rangle_m, \dots)$

This Hamiltonian is for a one-dimensional tight-binding (TB) lattice in momentum space with a lattice constant $2Q$, a nearest neighbor hopping amplitude Ω, and a harmonic potential $E_r k^2$. Compared with real space lattices, the potential energy and kinetic energy exchange their roles [63] in a momentum space lattice. The real space potential energy V contributes to the hopping term in a momentum space lattice, while the real space kinetic energy $\hbar^2 k^2/2m$ contributes to a harmonic potential, as shown in Fig. (5.3).

5.2.2.1 Subrecoil Coupling Regime $\Omega < E_r$

The eigenstates of the spatially periodic Hamiltonian are Bloch wavefunctions which have the lattice momenta k as good quantum numbers. For the momenta at the boundary of the Brillouin zone, $k = \pm 0.5$, $|k\rangle_m$ and $|k \mp 1\rangle_e$ has the same energy, as shown in Fig. (5.4b), and the model can be simplified to a two-level system. The effective Hamiltonian can be written as

$$H = \hat{\sigma} \cdot \mathbf{B} + \frac{E_r}{4}\mathbf{I}, \tag{5.15}$$

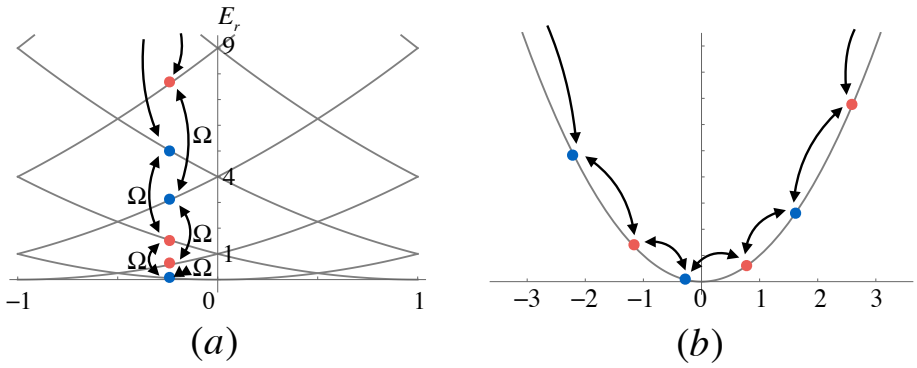

Figure 5.3: (a) Solid lines show the free particle dispersion relation. For $k = -0.25$, states with opposite spin (atomic state) couples with each other, where blue (red) dots denote $|m\rangle(|e\rangle)$ atomic state. (b) The equivalent model, a TB lattice in the background of a harmonic potential for $k = -0.25$ in Fig. (5.3a).

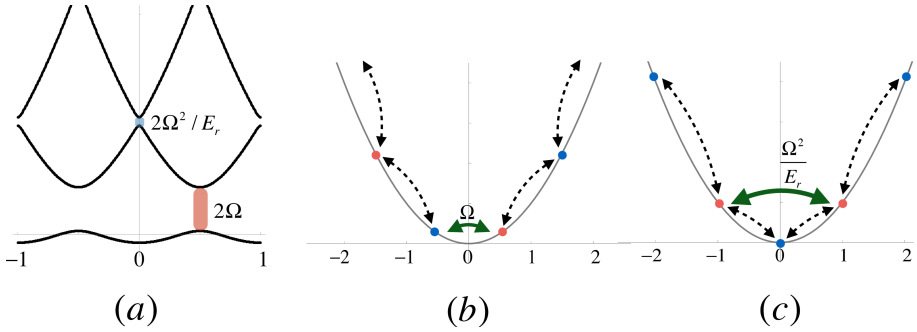

Figure 5.4: (a) The band structure of the TB lattice for $\Omega = 0.2E_r$. (b) The TB model when $k = 0.5$ is shown. Sold and dash lines denote the on-resonant and off-resonant coupling between $|k\rangle_m$ and $|k-1\rangle_e$. (c) The TB model when $k = 0$ is shown.

where $\mathbf{B} = (\Omega, 0, -E_r k)$, $\hat{\sigma}$ is the spin operator of $|\uparrow\rangle = |k-1\rangle_e$ and $|\downarrow\rangle = |k\rangle_m$. We could observe spin oscillations [64, 65] and the 1st order atomic Bragg scattering [66] when atom is pumped into this two-level system. A second-order coupling strength opens the gap between the second and third bands, which is the strongest near $k = 0, \pm 1$, where the effective coupling between $|k-1\rangle_e$ and $|k+1\rangle_e$is $V_{2nd} =_e \langle k-1|V\frac{1}{E_e-E_m}V|k+1\rangle_e = \frac{\Omega^2}{E_r}$, as shown in Fig. (5.4c). The 2nd order Bragg scattering could be observed [66] at this point. In this subrecoil regime, i.e., $\Omega < E_r$ we could always treat the system as an effective two-level system decoupled from other states at the momenta where gaps open. The experiments on atom laser, atom interferometry and spin-orbit coupling [64, 65] are mostly done in this subrecoil regime.

5.2.2.2 Superrecoil Coupling Regime $\Omega \gg E_r$

In the regime of $\Omega \gg E_r$, which is the case in our experiment, we define a length scale $\eta = \sqrt{\Omega/E_r}$ within which the potential energy is negligible compared with the hopping energy. The states inside this length form a tight-binding lattice structure in momentum space [49]. The real space kinetic energy is a shallow parabolic potential background in momentum space [67, 68]. It is reasonable to neglect the shallow harmonic potential in our experiment considering the finite decay rate and the large $\eta \approx 100$. After the atom is pumped into the lattice, the number of sites it can hop before it decays is Ω/Γ. If this number is much smaller than η, we can neglect the effect of the harmonic potential. This requires $\Gamma \gg \sqrt{\Omega E_r}$ which is satisfied in our experiment.

5.2.2.3 TDS in BEC

The atoms are initially prepared in a BEC of the ground state $|g\rangle$. We approximate this state as $|G\rangle \equiv |N, \mathbf{q} = 0\rangle_g$ which means N atoms in the state $|g\rangle$ with zero momentum. This is a good approximation for the current investigation although the atoms are in a trap and the ground state contains other momentum components. A single photon resonantly

absorbed by the BEC results in the state $|1,\mathbf{k_p}\rangle_e|N-1,0\rangle_g$ where $\mathbf{k}_p$ is the wavevector of the probe photon, i.e., one atom is excited from $|g\rangle$ to $|e\rangle$ and acquires a recoil momentum $\mathbf{k}_p$. We first analyse the spontaneous emission of this excited state. The interaction Hamiltonian between the atoms and the vacuum modes is ($\hbar = 1$)

$$H_1 = \sum_{\mathbf{k},\mathbf{q}} g_{\mathbf{k}} a^\dagger_{\mathbf{k}} b^\dagger_g(\mathbf{q}-\mathbf{k}) b_e(\mathbf{q}) + h.c., \tag{5.16}$$

where $a_{\mathbf{k}}$ is the annihilation operator of the photon with wavevector $\mathbf{k}$, $g_{\mathbf{k}}$ is the coupling constant between the photon and atoms, $b_i(\mathbf{q})$ is the annihilation operator of the atoms in the inner state $|i\rangle$ with momentum $\mathbf{q}$.

One particular vacuum mode with wave vector $\mathbf{k}_p$ dominates the spontaneous emission in the excited BEC. It is easy to find that the coupling between the single photon excited state $|1,\mathbf{k_p}\rangle_e|N-1,0\rangle_g$ and the ground state is

$$\langle 0,0|_e\langle N,0|_g H_1 |1,\mathbf{k_p}\rangle_e|N-1,0\rangle_g = \sqrt{N} g_{\mathbf{k_p}} a^\dagger_{\mathbf{k}_p}, \tag{5.17}$$

accompanied by the radiation of a photon with wavevector $\mathbf{k}_p$. The interaction is enhanced by $\sqrt{N}$ times, which is a signature of the superradiance. Instead, if the atoms radiate a photon with momentum $\mathbf{k} \neq \mathbf{k}_p$, the coupling strength is

$$\langle 0,0|_e\langle 1,\mathbf{k}_p-\mathbf{k};N-1,0|_g H_1 |1,\mathbf{k_p}\rangle_e|N-1,0\rangle_g = g_{\mathbf{k}} a^\dagger_{\mathbf{k}}, \tag{5.18}$$

without superradiant enhancement. Here $\langle 1,\mathbf{k}_p-\mathbf{k};N-1,0|_g$ means in the final state we have one atom with momentum $\mathbf{k}_p-\mathbf{k}$ and $N-1$ atoms with zero momentum in the state $|g\rangle$. Therefore, the spontaneous decay of the state $|1,\mathbf{k_p}\rangle_e|N-1,0\rangle_g$ is dominated by the superradiance emission in the mode $\mathbf{k}_p$. The state $|1,\mathbf{k_p}\rangle_e|N-1,0\rangle_g$ is a BEC version of the timed Dicke state $|e_{\mathbf{k}_p}\rangle = \frac{1}{\sqrt{N}}\sum_j e^{i\mathbf{k}_p\cdot\mathbf{r}_j}|g_1,g_2,...,e_j,...,g_N\rangle$ [7], where $|i_j\rangle$ ($i=e,g$)

and $\mathbf{r}_j$ are the internal states and position of the jth atom.

5.2.2.4 Excitation Transport in SL

However, such a radiation is difficult to observe in the experiment, since the excitation and radiation signals are in the same direction. In order to observe the directional radiation, we need to change the wavevector of the excited state before it can radiate. This can be done by introducing two coherent fields that drive the transition between the excited state $|e\rangle$ and another ground state $|m\rangle$. The interaction Hamiltonian is

$$H_c = \sum_{\mathbf{q},j} \Omega_j b_m^\dagger(\mathbf{q}+\mathbf{k}_{cj}) b_e(\mathbf{q}) + h.c., \tag{5.19}$$

where Ω_j are the Rabi frequency of the coupling field with the wavevector $\mathbf{k}_{cj}$ ($j = 1, 2$). We introduce a short-hand notation $|e_l\rangle \equiv |1, \mathbf{k}_l\rangle_e |N-1, 0\rangle_g$ and $|m_l\rangle \equiv |1, \mathbf{k}_l - \mathbf{k}_{c1}\rangle_m |N-1, 0\rangle_g$ with $\mathbf{k}_l = \mathbf{k}_p - l(\mathbf{k}_{c1} - \mathbf{k}_{c2})$ and l an integer. Through the Hamiltonian in Eq. (5.19), $|e_l\rangle$ are connected via $|m_l\rangle$ to form a 1D tight-binding chain, as shown in Fig. (5.1a). Considering the on-site potential induced by the detuning of the coupling field $\Delta_c \equiv \nu_c - \omega_{em}$ with ν_c the coupling field frequency and ω_{em} the transition frequency between $|e\rangle$ and $|m\rangle$, we can write down the interaction Hamiltonian in the subspace expanded by $|e_l\rangle$ and $|m_l\rangle$ in a tight-binding form,

$$\begin{aligned} H_I = &\sum_l \frac{\Delta_c}{2}(|m_l\rangle\langle m_l| - |e_l\rangle\langle e_l|) \\ &+ (\Omega_1 |m_l\rangle\langle e_l| + \Omega_2 |e_{l-1}\rangle\langle m_l| + h.c.). \end{aligned} \tag{5.20}$$

In this lattice, if $|\mathbf{k}_f| = |\mathbf{k}_p|$ for a certain $|e_f\rangle$, a vacuum mode with wavevector $\mathbf{k}_f$ can couple the excited state $|e_f\rangle$ back to the ground state via directional superradiant emission in $\mathbf{k}_f$. Other states with $|\mathbf{k}_l| \neq |\mathbf{k}_p|$ cannot find a vacuum mode to achieve a superradiant enhancement in their spontaneous emission. The kinetic energy due to the recoil of the

BEC atoms $\hbar \mathbf{k}_l^2/2m$ introduces a parabolic potential in momentum space, a BEC version of the superradiance lattice. In our experiment, this recoil energy is much smaller than Ω_j and can be neglected, as mentioned in subsection. (5.2.2.2).

5.2.3 Hamiltonian

The Hamiltonian of the BEC atoms interacting with the probe and coupling light beams is (with $\hbar = 1$),

$$\begin{aligned} H = \int d\mathbf{q}(\Delta_p + \frac{\hbar^2 k^2}{2m}) b_e^\dagger(\mathbf{q}) b_e(\mathbf{q}) + (\Delta_{\text{2ph}} + \frac{\hbar^2 k^2}{2m}) b_m^\dagger(\mathbf{k}) b_m(\mathbf{k}) \\ + \Omega_1 b_e^\dagger(\mathbf{q}) b_m(\mathbf{q} - \mathbf{k}_1) + \Omega_2 b_e^\dagger(\mathbf{q}) b_m(\mathbf{q} + \mathbf{k}_1) + \sqrt{N}\Omega_p b_e^\dagger(\mathbf{k}_p) b_g(0) + \text{H.c.}, \end{aligned} \tag{5.21}$$

where $\Delta_p = \omega_{eg} - \nu_p$ is the detuning of the probe field which has frequency ν_p, $\Delta_{\text{2ph}} = \omega_{mg} + \nu_c - \nu_p$ is the two-photon detuning. A source term $\Omega_p b_e^\dagger(\mathbf{k}_p) b_g(0)$ loads atoms from zero momentum ground state (BEC state) to the $|e\rangle$ state with k_p momentum. The excitations are further transported via the coupling fields to $|m_l\rangle$ and $|e_l\rangle$ (l is an integer). Since most of the atoms are in the BEC ground state, we can rewrite the Hamiltonian as

$$H = H_k + H_0 + H_{\text{NN}} + H_{\text{source}},$$

$$H_k = \sum_l \frac{\hbar^2(\mathbf{k}_p + 2l\mathbf{k}_1)^2}{2m} |e_l\rangle\langle e_l| + \frac{\hbar^2(\mathbf{k}_p + (2l-1)\mathbf{k}_1)^2}{2m} |m_l\rangle\langle m_l|, \tag{5.22}$$

$$H_0 = \sum_l \Delta_p |e_l\rangle\langle e_l| + \Delta_{\text{2ph}} |m_l\rangle\langle m_l, | \tag{5.23}$$

$$H_{\text{NN}} = \sum_n (\Omega_1 |e_l\rangle\langle m_l| + \Omega_2 |e_{l-1}\rangle\langle m_l|) + \text{H.c.}, \tag{5.24}$$

$$H_{\text{source}} = \sqrt{N}\Omega_p |e_0\rangle\langle N|_g + \text{H.c.}, \tag{5.25}$$

where H_0 is the on-site energy of the states in superradiance lattice [49], H_{NN} contains the nearest neighboring (NN) terms and H_{source} loads atoms from ground state $|N\rangle_g$ to the

BEC timed-Dicke state $|e_0\rangle$ [7]

For a weak probe field, we assume the steady state is $|\phi_s\rangle = |N\rangle_g - O(A^2) - O(B^2) + \sum_l A_l|e_l\rangle + B_l|m_l\rangle$, where $|A_n|(|B_n|) \ll 1$. The density matrix can be assumed as $\rho_s = |N\rangle_g\langle N|_g + (\sum_l A_l|e_l\rangle\langle N|_g + B_l|m_l\rangle\langle N|_g) + h.c.$ which satisfies the Liouville equation,

$$i\frac{\partial}{\partial t}\rho_s = [H, \rho_s] + \mathcal{L}(\rho_s), \tag{5.26}$$

In the steady state, $\frac{\partial}{\partial t}\rho_s = 0$, which results in

$$\begin{pmatrix} \dots & \Omega_2 & & & & & \\ \Omega_2 & \Delta_{\text{2ph}} & \Omega_1 & & & & \\ & \Omega_1 & \Delta_p - i\Gamma & \Omega_2 & & & \\ & & \Omega_2 & \Delta_{\text{2ph}} & \Omega_1 & & \\ & & & \Omega_1 & \Delta_p - i\Gamma & \Omega_2 & \\ & & & & \Omega_2 & \dots & \end{pmatrix} \cdot \begin{pmatrix} \dots \\ B_{-1} \\ A_0 \\ B_0 \\ A_1 \\ \dots \end{pmatrix} = \begin{pmatrix} \dots \\ 0 \\ \Omega_p \\ 0 \\ 0 \\ \dots \end{pmatrix}, \tag{5.27}$$

where $\Gamma = \gamma/2$ is the decoherence rate between $|e\rangle$ and $|g\rangle$. This equation can be solved numerically with a reasonable cutoff of its dimension. The solution of A_l and B_l are going to be used in the coupled-wave equation, as shown in the following.

5.2.4 Experimental Result & Numerical Simulation

In the numerical simulation, we also included the energy level of $|5^2S_{1/2}, F = 2, m_F = 1\rangle$, which is coupled by the probe field to the excited state $|e\rangle$. In addition, at the node of the standing wave, the EIT condition that the coupling field is stronger than the probe field fails. We need to consider the population pumped into the state $|m\rangle$, which results in the little peak at the middle of the spectra. Theoretical fitting is performed with the experimental parameters in Fig. (5.5) and (5.6).

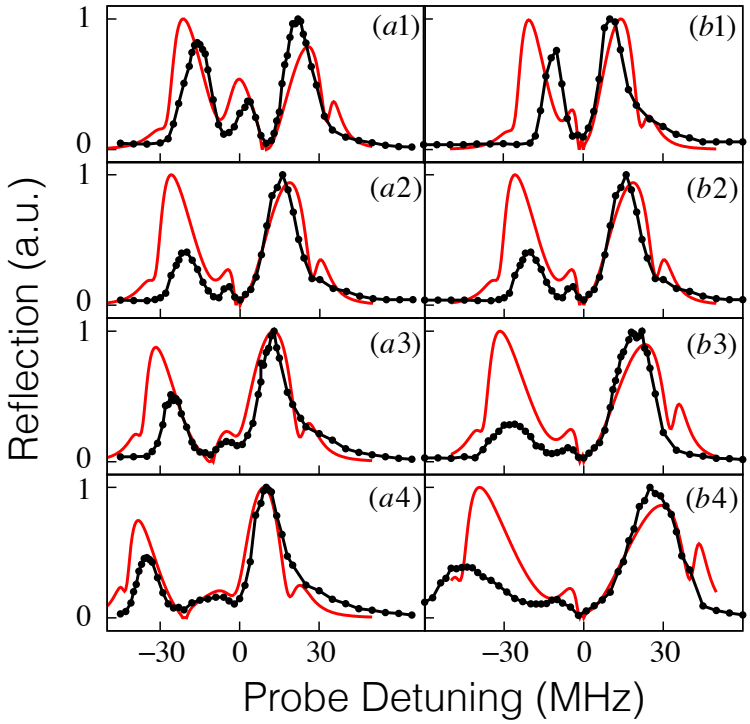

Figure 5.5: Superradiance emission spectra for the different detuning and intensity of the coupling laser. The black line is experiment data, red line is numerical simulation with experimental parameters. (a1)- (a4), The detuning Δ_c of the coupling laser are $10MHz$, $0MHz$, $-10MHz$, and $-20MHz$, respectively. The power of each coupling laser is $200\mu W$ and the probe light is $25\mu W$. (b1)- (b4), The intensity of the coupling laser are $100\mu W$, $200\mu W$, $400\mu W$, and $800\mu W$ for respectively. The coupling laser is on resonance and the power of the probe light is $25\mu W$.

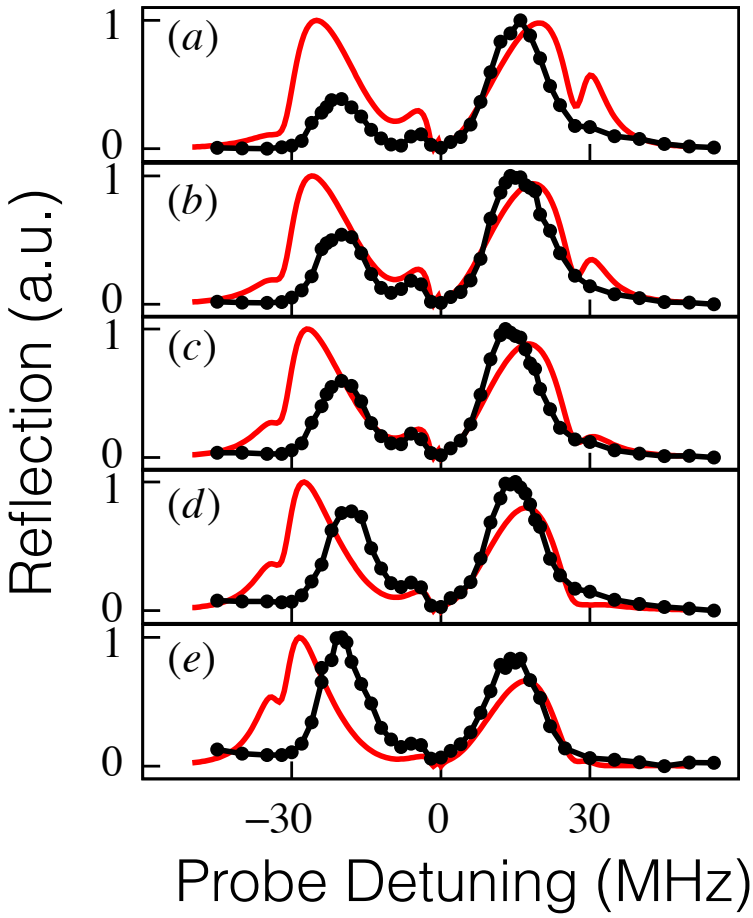

Figure 5.6: Superradiant spectra for the different angles of the incident probe beam. The black line is experiment data, red line is numerical simulation with experimental parameters. The angles of the incident probe beam deviated from $\phi = 56^\circ$ are (a) -0.2°, (b) 0°, (c) 0.2°, (d) 0.4° and (e) 0.8°. The power of each coupling laser is $200\mu W$ and $\Delta_c = 0$. The power of the probe light is $25\mu W$.

The two peaks in most of the figures are asymmetric. Both of the asymmetry can be attributed to the phase mismatch Δk. The finite size L of the BEC brings a finite resolution of the momentum, $\delta k = 2\pi/L$. For an infinitely long BEC, the phase matching is achieved in a unique direction. On the other hand, if the BEC is much smaller than the wavelength of the light, there is no preferred direction of the superradiant emission. In our experiment, within the size of the BEC there are around 50 periods of the standing wave. Instead of determining the position of a reflection band with near unity reflectance around the phase matching point for a much longer sample, the dispersion only introduces a slight bias between the heights of the two reflection peaks, similar to the optical Bragg scattering experiment of cold atomic gases in optical lattices.

The major discrepancy between the experimental data and the theoretical fitting is that the left peak in the experiment is generally lower than predicted in the theory. In addition, when the power of the coupling field increases, the left peak shifts to the red side further than predicted. These two inconsistencies may be attributed to the collective decay rate and Lamb shift, as well as the non-zero momentum component in the BEC.

6.1 Integer Quantum Hall Effect (IQHE)

6.1.1 Hall Effect

Consider electrons in a two-dimensional (2D) plane (x-y plane), we get some current j by applying an electric field. Typically, the direction of the current is the same as the electric field, which can be assumed in the x axis. Therefore we obtain the resistivity $\rho_{xx} = E_x/j_x$.

Now a magnetic field is applied in the z direction, perpendicular with the plane; Lorentz force drives the charge accumulation on the top and bottom edge. The charge on the edges produces an electric field in y direction. Then we obtain the Hall resistivity $\rho_{xy} = E_y/j_x$. It can be derived from classical mechanics,

$$\begin{aligned} eE_y &= evB, \\ j_x &= envv, \\ \rho_{xy} &= \frac{E_y}{j_x} = \frac{B}{en}. \end{aligned} \tag{6.1}$$

6.1.2 Landau Levels

Turn to quantum mechanical picture, we have the Hamiltonian of a charged particle in a magnetic field,

$$H = \frac{(\mathbf{p} + e\mathbf{A})^2}{2m}, \tag{6.2}$$

with Landau gauge $A_y = Bx$ and $A_x = 0$, $\mathbf{A} = p_x\hat{x} + p_y\hat{y}$ is the vector potential, $\hat{x}(\hat{y})$ is the unit vector in the $x(y)$ direction, m is the particle mass. There is no y dependence in

Eq. (6.2), therefore we act the eigenfunction ansatz $\psi(x,y) = e^{iky}u(x)$ on the Hamiltonian

$$H\psi(x,y) = [\frac{p_x^2}{2m} + \frac{1}{2}m\omega_B(x + kl_B^2)^2]e^{iky}u(x) = e^{iky}H_k u(x), \tag{6.3}$$

with the cyclotron frequency $\omega_B = eB/m$ and the magnetic length $l_B = \sqrt{\hbar/eB}$. The reduced Hamiltonian H_k is actually a harmonic oscillator in the x direction, with a center displacement $x_0 = -kl_B^2$ from the origin and the frequency is the cyclotron frequency ω_B. The eigenenergy is

$$E_n = \hbar\omega_B(n + \frac{1}{2}), \tag{6.4}$$

the wavefunction of the eigenstate is

$$\psi_{n,k}(x,y) \sim e^{iky}H_n(x - x_0)e^{-(x-x_0)^2/2l_B^2}. \tag{6.5}$$

Consider the wavefunction in the finite region of $x - y$ plane (say a rectangle with length L_x and L_y), the center of the Harmonic oscillator is localized between 0 and L_x. We would expect that the allowed k ranges from $-L_x/l_B^2$ to 0. The number of states in each Landau level is

$$\mathcal{N} = \frac{L_x}{2\pi}\int_{-L_x/l_B^2}^{0} dk = \frac{A}{2\pi l_B^2} = \frac{\Phi}{\Phi_0}, \tag{6.6}$$

where $A = L_xL_y$ is the area of the 2D plane, $\Phi = AB$ is the flux penetrate the sample and $\Phi_0 = h/e$ is the quantum flux.

6.1.3 Turning On an Electric Field

The Hamiltonian is slightly modified by adding the electric potential

$$\begin{aligned} H &= \frac{p_x^2}{2m} + \frac{(p_y + eBx)^2}{2m} - eEx, \\ &= \frac{p_x^2}{2m} + \frac{[p_y + eB(x - x_1)]^2}{2m} - eEx_1 + \frac{m}{2}\frac{E^2}{B^2}, \end{aligned} \tag{6.7}$$

where $x_1 = -kl_B^2 + eE/m\omega_B^2$ is the new center offset of the wavefunction. The eigenenergy and wavefunction are

$$E_{n,k} = \hbar\omega_B(n + \frac{1}{2}) - eEx_1 + \frac{m}{2}\frac{E^2}{B^2}, \tag{6.8}$$

$$\psi_{n,k}(x, y) \sim e^{iky} H_n(x - x_1) e^{-(x-x_1)^2/2l_B^2}. \tag{6.9}$$

The group velocity of the states in the y direction is

$$v_y = \frac{1}{\hbar}\frac{\partial E_{n,k}}{\partial k} = \frac{E}{B}. \tag{6.10}$$

6.1.4 The Conductivity Quantization

The current operator $\mathbf{I}$ is given by

$$\mathbf{I} = -\frac{e}{m}\frac{d}{dt}\mathbf{x} = -\frac{e}{m}\frac{i}{\hbar}[H, \mathbf{x}] = -\frac{e}{m}(\mathbf{P} + eA), \tag{6.11}$$

where $\mathbf{P} = p_x\hat{x} + p_y\hat{y}$ is the canonical momentum. The expectation value of the current in x and y direction is

$$\langle I_x \rangle = -\frac{e}{m}\langle\psi| - i\hbar\frac{\partial}{\partial x}|\psi\rangle = 0, \tag{6.12}$$

$$\langle I_y \rangle = -\frac{e}{m}\langle\psi| - i\hbar\frac{\partial}{\partial y} + eBx|\psi\rangle = -en_f\sum_k \frac{E}{B} = -\frac{en_f A}{\Phi_0}, \tag{6.13}$$

where n_f is the number of the filled Landau levels and the sum over momentum k is the degeneracy $\mathcal{N}$ in (6.6). We divide through by the area to get the current density $\langle \mathbf{j} \rangle = \langle \mathbf{I} \rangle / A$. Compare with the definition of the conductivity tensor in 2D

$$\begin{pmatrix} j_x \\ j_y \end{pmatrix} = \begin{pmatrix} \sigma_{xx} & \sigma_{xy} \\ \sigma_{yx} & \sigma_{yy} \end{pmatrix} \begin{pmatrix} E_x \\ E_y \end{pmatrix}, \tag{6.14}$$

we have $\sigma_{xx} = \sigma_{yy} = 0$ and $\sigma_{xy} = \sigma_{yx} = -en_f/\Phi_0 = -n_f e^2/h$. It shows that the Hall conductivity is quantized in unit of e^2/h and proportional with the number of the filled Landau levels.

6.2 Towards Topology

6.2.1 Kubo Formula

In order to justify the connection between the quantum Hall effect with topology, we need to take a little detour about Kubo formula. We seek the generalized expression for the electrical conductivity of a solid.

We start by dividing the Hamiltonian for the system H into two parts: H_0 is the the zero-field part and δH is the perturbation part induced by the external field. We can expand the Hamiltonian in Eq. (6.2)

$$H = H_0 + H' = H_0 + \frac{e}{m}\mathbf{A}(t) \cdot \mathbf{p}, \tag{6.15}$$

$$\rho = \rho_0 + \delta\rho, \tag{6.16}$$

where we assume that the external field is an AC field with the frequency ω, i.e., $\mathbf{A}(t) = \mathbf{A}_0 e^{-i\omega t + i\eta t}$, ρ_0 is the equilibrium state of the zero-field Hamiltonian H_0 (It's the Fermi distribution for electrons f_0). Since the field is adiabatically turned on at $t = -\infty$, we have $\eta \to 0^+$. The expectation value of the current operator is $\langle \mathbf{j} \rangle = \text{Tr}[\mathbf{j}\delta\rho]$ where the current operator is given by $\mathbf{j} = e\mathbf{v}$. By using $E(t) = -\dot{A}(t)$, we have $E(\omega) = i\omega A(\omega)$. We obtain

$$H' = \frac{\hbar e}{im}\mathbf{A} \cdot \boldsymbol{\nabla} = -\frac{\hbar e}{m\omega}\mathbf{E} \cdot \boldsymbol{\nabla}, \tag{6.17}$$

In the presence of the time-dependence external perturbation H', we have the Schrödinger

equation and collect terms in the first order of perturbation

$$i\hbar\frac{d}{dt}\delta\rho = [H_0, \delta\rho] + [H', \rho_0], \tag{6.18}$$

Since $\delta\rho$ should have the same time dependence with H' (in slow changing envelope approximation), we have $\dot{\delta\rho} = (-i\omega + \eta)\delta\rho$. In order to obtain the matrix element in the basis of equilibrium state $|\mathbf{k}\rangle$

$$\begin{aligned} i\hbar\langle\mathbf{k}'|\dot{\delta\rho}|\mathbf{k}\rangle &= \langle\mathbf{k}'|H_0\delta\rho - \delta\rho H_0|\mathbf{k}\rangle + \langle\mathbf{k}'|H'\rho_0 - \rho_0 H'|\mathbf{k}\rangle, \\ &= [E(\mathbf{k}') - E(\mathbf{k})]\langle\mathbf{k}'|\delta\rho|\mathbf{k}\rangle - [f_0(\mathbf{k}') - f_0(\mathbf{k})]\langle\mathbf{k}'|H'|\mathbf{k}\rangle, \end{aligned} \tag{6.19}$$

therefore the matrix elements read

$$\langle\mathbf{k}'|\delta\rho|\mathbf{k}\rangle = \frac{f_0(\mathbf{k}') - f_0(\mathbf{k})}{E(\mathbf{k}') - E(\mathbf{k}) + i\hbar(i\omega - \eta)}\langle\mathbf{k}'|H'|\mathbf{k}\rangle, \tag{6.20}$$

combined with current operator, we have the Hall conductivity

$$\begin{aligned} \sigma_{xy} = \frac{\langle j_y\rangle}{E} &= \sum_{\mathbf{k}\mathbf{k}'}\langle\mathbf{k}|j_y|\mathbf{k}'\rangle\langle\mathbf{k}'|\delta\rho|\mathbf{k}\rangle, \\ &= \sum_{\mathbf{k}\mathbf{k}'}\frac{e^2}{i\omega}\frac{f_0(\mathbf{k}') - f_0(\mathbf{k})}{E(\mathbf{k}') - E(\mathbf{k}) + i\hbar(i\omega - \eta)}\langle\mathbf{k}|v_y|\mathbf{k}'\rangle\langle\mathbf{k}'|v_x|\mathbf{k}\rangle, \\ &= \sum_{\mathbf{k}\mathbf{k}'}\frac{e^2}{i\omega}f_0(\mathbf{k}')[\frac{\langle\mathbf{k}|v_y|\mathbf{k}'\rangle\langle\mathbf{k}'|v_x|\mathbf{k}\rangle}{E(\mathbf{k}') - E(\mathbf{k}) + i\hbar(i\omega - \eta)} + \frac{\langle\mathbf{k}|v_x|\mathbf{k}'\rangle\langle\mathbf{k}'|v_y|\mathbf{k}\rangle}{E(\mathbf{k}') - E(\mathbf{k}) - i\hbar(i\omega - \eta)}]. \end{aligned} \tag{6.21}$$

We are interested by the DC field response with $\omega \to 0$ and $\eta = 0$. Provided with the relation

$$\frac{1}{E(\mathbf{k}') - E(\mathbf{k}) \pm \omega} = \frac{1}{E(\mathbf{k}') - E(\mathbf{k})}(1 \mp \frac{1}{E(\mathbf{k}') - E(\mathbf{k})}), \tag{6.22}$$

we separate the conductivity σ_{xy} into two parts, $\sigma_{xy} = \sigma_1 + \sigma_2$,

$$\sigma_1 = \sum_{\mathbf{k}\mathbf{k}'} \frac{e^2}{i\omega} f_0(\mathbf{k}') \frac{\langle \mathbf{k}|v_y|\mathbf{k}'\rangle\langle \mathbf{k}'|v_x|\mathbf{k}\rangle + \langle \mathbf{k}|v_x|\mathbf{k}'\rangle\langle \mathbf{k}'|v_y|\mathbf{k}\rangle}{E(\mathbf{k}') - E(\mathbf{k})}, \tag{6.23}$$

$$\sigma_2 = \sum_{\mathbf{k}\mathbf{k}'} \frac{\hbar e^2}{i} f_0(\mathbf{k}') \frac{-\langle \mathbf{k}|v_y|\mathbf{k}'\rangle\langle \mathbf{k}'|v_x|\mathbf{k}\rangle + \langle \mathbf{k}|v_x|\mathbf{k}'\rangle\langle \mathbf{k}'|v_y|\mathbf{k}\rangle}{[E(\mathbf{k}') - E(\mathbf{k})]^2}, \tag{6.24}$$

Although σ_1 appears divergent when $\mathbf{k} = \mathbf{k}'$, it can be eliminated using the Heisenberg equation of motion

$$\langle \mathbf{k}|v_y|\mathbf{k}'\rangle = \langle \mathbf{k}|\frac{i}{\hbar}[H_0, y]|\mathbf{k}'\rangle = \frac{i}{\hbar}[E(\mathbf{k}) - E(\mathbf{k}')]\langle \mathbf{k}|y|\mathbf{k}'\rangle.$$

It yields

$$\sigma_1 = \sum_{\mathbf{k}\mathbf{k}'} \frac{e^2}{\hbar\omega}[\langle \mathbf{k}|y|\mathbf{k}'\rangle\langle \mathbf{k}'|v_x|\mathbf{k}\rangle - \langle \mathbf{k}|y|\mathbf{k}'\rangle\langle \mathbf{k}'|v_x|\mathbf{k}\rangle] = 0. \tag{6.25}$$

In the limitation of zero Temperature, the Fermi distribution is simplified to $f_0(E) = 1(0)$ when the energy E is lower (higher) than the Fermi energy E_F. We can further simplify the Kubo formula (see Appendix A) and use $|u(\mathbf{k})\rangle$ to denote the eigenstate of zero-field Hamiltonian with quasimomentum $\mathbf{k}$ in BZ to avoid confusion.

$$\sigma_{xy} = \sum_{n_f} \frac{e^2}{h} C, \tag{6.26}$$

where

$$C = -i\frac{1}{2\pi}\int_{BZ} d\mathbf{k}\langle \frac{\partial u}{\partial k_y}|\frac{\partial u}{\partial k_x}\rangle - \langle \frac{\partial u}{\partial k_x}|\frac{\partial u}{\partial k_y}\rangle, \tag{6.27}$$

The dimensionless quantity C is a number known as the first Chern number. It is always an integer.

6.2.2 Berry Connection, Berry Curvature and Chern Number

For the Bloch wave function $|\psi\rangle = e^{i\mathbf{k}\cdot\mathbf{r}}|u_\mathbf{k}\rangle$ in 2D, we define Berry connection

$$\mathbf{A}(\mathbf{k}) = -i\langle u_\mathbf{k}|\boldsymbol{\nabla}|u_\mathbf{k}\rangle, \tag{6.28}$$

and Berry curvature

$$F(\mathbf{k}) = \boldsymbol{\nabla}\times\mathbf{A}|_z = -i\epsilon_{ij}\langle\partial_i u_\mathbf{k}|\partial_j u_\mathbf{k}\rangle, \tag{6.29}$$

where ∇ is the partial derivative operator in momentum space and $\epsilon_{xy} = -\epsilon_{yx} = 1$ is the Levi-Civita symbol in 2D. The Berry quantities, the magnetic quantities, and differential geometry quantities are compared in Table. (6.1). The following items are quantized due

Berry	Magnetic	Differential Geometry
Berry connection $\mathbf{A}(\mathbf{k})$	Vector potential $\mathbf{A}$	Connection on a bundle
Berry curvature $\mathbf{F} = \nabla\times\mathbf{A}$	Magnetic field $\mathbf{B} = \boldsymbol{\nabla}\times\mathbf{A}$	Gaussian curvature
Chern Number C	magnetic charge $q_m = n\frac{c\hbar}{2q_e}$	Euler characteristic χ_M

Table 6.1: The corresponding quantities of Berry, magnetic, and differential geometry are compared

to topological reasons, which is known as topological quantization: the Chern number C is quantized, which measures the quantized Hall conductivity

$$C = \frac{1}{2\pi}\int_{BZ} F d^2\mathbf{k} = \frac{1}{2\pi}\oint_{BZ}\mathbf{A}\cdot d\mathbf{k}, \tag{6.30}$$

the n is quantized, which measures the number of magnetic monopole inside a closed surface M

$$n = \int_M \mathbf{B}\cdot ds, \tag{6.31}$$

and the Euler characteristic χ_M is quantized, which measures the topological nature of a closed manifold M. The idea of the topology originates from the description of three-dimensional manifold. χ_M is directly related to the genus g of the manifold, $\chi_M = 2(1 - g)$. The genus measures the number of "handles" on a object. For instance, sphere has no handle, so $g = 0$ and $\chi_M = 2$. For torus in $g = 1$ and $\chi_M = 2$. For double torus $g = 2$ and $\chi_M = -2$. χ_M will remain the same if we deform any manifold in real space adiabatically. The concept is generalized to quantum physics, giving the IQHE a topological nature.

6.3 Chern Insulator

6.3.1 Aharonov-Bohm (AB) Effect

The AB effect is a quantum phenomenon. If a charged particle moves around a closed contour, the phase difference $\Delta\phi$ between the final and initial states is proportional to the magnetic flux penetrating the contour $\Phi = \int \mathbf{B}\cdot ds = \oint \mathbf{A}\cdot dl$, $\Delta\phi = \Phi e/\hbar$. The magnetic flux is invariant under gauge transformation

$$\begin{aligned} \mathbf{A}' &\to \mathbf{A} + \boldsymbol{\nabla}\chi, \\ V' &\to V - \frac{\partial\chi}{\partial t}, \end{aligned} \tag{6.32}$$

therefore it yields the gauge invariance of $\Delta\phi$

$$\Delta\phi' = \frac{e}{\hbar}\oint \mathbf{A}'\cdot dl = \frac{e}{\hbar}\oint(\mathbf{A} + \boldsymbol{\nabla}\chi)\cdot dl = \frac{e}{\hbar}\oint \mathbf{A}\cdot dl + (\chi_0 - \chi_0) = \Delta\phi. \tag{6.33}$$

For the discrete version of AB effect in the lattice, let us consider three sites a, b and c for simplicity. The hopping constant between these three sites are t_{ab}, t_{bc} and t_{ca} respectively. If a particle hops along the trajectory of $a \to b \to c \to a$, the hopping strength around the closed loop is

$$t_{ab}t_{bc}t_{ca} = |t_{ab}t_{bc}t_{ca}|\, e^{i(\phi_{ab}+\phi_{bc}+\phi_{ca})}. \tag{6.34}$$

The phase picked up by the particle is $\phi_{ab} + \phi_{bc} + \phi_{ca} = 2\pi\Phi/\Phi_0$, where $\Phi_0 = h/e$ is the unit quantum flux. Since the phase of any segment of the trajectory ϕ_{ij} is gauge dependent, $\phi'_{ij} \to \phi_{ij} = \phi_{ij} + (\chi_i - \chi_j)e/\hbar$, the phase picked up by the particle for any open trajectory is not a physical observable and has no physical meaning, which is different from the one for a closed loop. The phase ϕ_{ij} is directional, t_{ij} and t_{ji} have opposite complex phases, i.e., $\phi_{ij} = -\phi_{ji}$, because of the Hermitian condition. The complex hopping constant induced by the magnetic field breaks the time-reversal symmetry because magnetic field changes its direction $B \to -B$ in the time reversal transformation. In other words, all the phases should flip their sign.

However, if the system contains the intrinsic mechanism (instead of external field) to induce the complex hopping constant with nonzero phase accumulation over some closed loops, the particle interacts with an effective magnetic field which is defined by the phase, or the effective magnetic flux.

6.3.2 The Haldane Model

Surprisingly, the non-trivial Chern number may not involve with any magnetic field. Haldane [26] designed the first system which has the Hall-like response, insulating bulk and conductive edge, without the existence of external magnetic field and the Landau levels.

In the basis of the tight-binding model of graphene, let us add some next nearest neighbor (NNN) interaction with complex hopping constant. In Fig. (6.1), we choose the amplitude t_2 and complex phase ϕ to be the same for all the NNN bonds. If the particle hopping direction is along the arrow marked, it picks up a phase of ϕ. If the hopping direction is

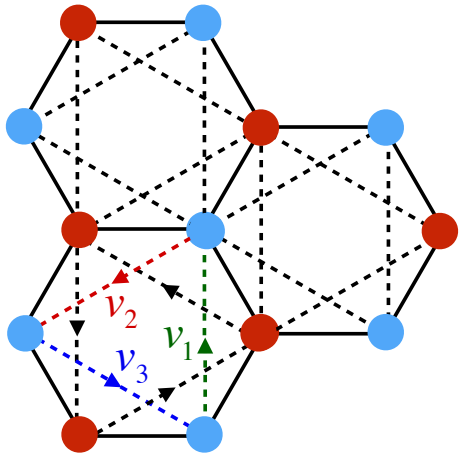

Figure 6.1: The Haldane model, showing NN bonds (solid lines) and NNN bonds (dashed lines). Arrows on the NNN bonds indicate the direction of the positive phase picked up by particle hopping along the bonds.

opposite with arrow, the phase is $-\phi$. There are three types of NNN bonds along

$$\begin{aligned}
\mathbf{v}_1 &= \mathbf{e}_3 - \mathbf{e}_2 = a(0, \sqrt{3}), \\
\mathbf{v}_2 &= \mathbf{e}_1 - \mathbf{e}_3 = a(-\frac{3}{2}, -\frac{\sqrt{3}}{2}), \\
\mathbf{v}_3 &= \mathbf{e}_2 - \mathbf{e}_1 = a(\frac{\sqrt{3}}{2}, -\frac{3}{2}).
\end{aligned} \tag{6.35}$$

The interaction term of the NNN bonds is

$$H_{NNN} = -t_2 e^{i\phi} \sum_i (a^\dagger_{\mathbf{r}_i} a_{\mathbf{r}_i+\mathbf{v}_1} + a^\dagger_{\mathbf{r}_i} a_{\mathbf{r}_i+\mathbf{v}_2} + a^\dagger_{\mathbf{r}_i} a_{\mathbf{r}_i+\mathbf{v}_3}) + h.c. + (a \to b, \phi \to -\phi). \tag{6.36}$$

Apply the 2D Fourier transformation, we obtain

$$\begin{aligned}
H_{NNN} = &-2t_2 \sum_{\mathbf{k}} a^\dagger_{\mathbf{k}} a_{\mathbf{k}} [\cos(\mathbf{k}\cdot\mathbf{v}_1 - \phi) + \cos(\mathbf{k}\cdot\mathbf{v}_2 - \phi) + \cos(\mathbf{k}\cdot\mathbf{v}_3 - \phi)] \\
&- 2t_2 \sum_{\mathbf{k}} b^\dagger_{\mathbf{k}} b_{\mathbf{k}} [\cos(\mathbf{k}\cdot\mathbf{v}_1 + \phi) + \cos(\mathbf{k}\cdot\mathbf{v}_2 + \phi) + \cos(\mathbf{k}\cdot\mathbf{v}_3 + \phi)].
\end{aligned} \tag{6.37}$$

Together with the NN bonds Hamiltonian in Eq. (4.23), the Hamiltonian of Haldane model $H = H_{NN} + H_{NNN}$ is

$$H(\mathbf{k}) = \begin{pmatrix} H_{11}(\mathbf{k}) & H_{12}(\mathbf{k}) \\ H_{21}(\mathbf{k}) & H_{22}(\mathbf{k}) \end{pmatrix}, \tag{6.38}$$

where the non-diagonal terms are the same with the graphene model and the diagonal terms are

$$\begin{aligned} H_{11} &= -2t_2[\cos(\mathbf{k}\cdot\mathbf{v}_1 - \phi) + \cos(\mathbf{k}\cdot\mathbf{v}_2 - \phi) + \cos(\mathbf{k}\cdot\mathbf{v}_3 - \phi)], \\ H_{22} &= -2t_2[\cos(\mathbf{k}\cdot\mathbf{v}_1 + \phi) + \cos(\mathbf{k}\cdot\mathbf{v}_2 + \phi) + \cos(\mathbf{k}\cdot\mathbf{v}_3 + \phi)]. \end{aligned} \tag{6.39}$$

The Hamiltonian in Eq. (6.38) is convenient to write in the Pauli matrices $H = \sum_i H_i\sigma_i$ (formally equivalent to a magnetic field interaction with a spin 1/2), where $\sigma_0 = I$ is the identity matrix and $\sigma_{x,y,z}$ is the corresponding Pauli matrices and the effective magnetic field is

$$H_0 = -2t_2\cos\phi(\cos\mathbf{k}\cdot\mathbf{v}_1 + \cos\mathbf{k}\cdot\mathbf{v}_2 + \cos\mathbf{k}\cdot\mathbf{v}_3), \tag{6.40}$$

$$H_z = -2t_2\sin\phi(\sin\mathbf{k}\cdot\mathbf{v}_1 + \sin\mathbf{k}\cdot\mathbf{v}_2 + \sin\mathbf{k}\cdot\mathbf{v}_3), \tag{6.41}$$

$$H_x = -t(\cos\mathbf{k}\cdot\mathbf{e}_1 + \cos\mathbf{k}\cdot\mathbf{e}_2 + \cos\mathbf{k}\cdot\mathbf{e}_3), \tag{6.42}$$

$$H_y = -t(\sin\mathbf{k}\cdot\mathbf{e}_1 + \sin\mathbf{k}\cdot\mathbf{e}_2 + \sin\mathbf{k}\cdot\mathbf{e}_3). \tag{6.43}$$

The energy dispersions for eigenstates are

$$\epsilon_\pm(\mathbf{k}) = H_0(\mathbf{k}) \pm \left|\vec{H}(\mathbf{k})\right|, \tag{6.44}$$

where $\left|\vec{H}\right| = \sqrt{H_x^2 + H_y^2 + H_z^2}$. We have $H_x = H_y = 0$ at $\mathbf{k} = \mathbf{K}_{1(2)}$ which is the band touching point of the graphene model. Without losing generality, the lower band ϵ_- is

studied in details in the following. Its eigenvector is

$$u_{-}^{(1)}(\mathbf{k}) = \frac{1}{\mathcal{N}^{(1)}} \begin{pmatrix} H_z - \left|\vec{H}\right| \\ H_x + iH_y \end{pmatrix}, \tag{6.45}$$

with $\mathcal{N}^{(1)}$ being the normalization factor. This wavefunction of ϵ_- is singular if $H_x(\mathbf{k}) = H_y(\mathbf{k}) = 0$ and $\mathcal{H}z > 0$

$$u_{-}^{(1)}(\mathbf{k}) = \frac{1}{\mathcal{N}^{(1)}} \begin{pmatrix} H_z - \sqrt{H_z^2} \\ 0 \end{pmatrix} = \frac{1}{\mathcal{N}^{(1)}} \begin{pmatrix} 0 \\ 0 \end{pmatrix}. \tag{6.46}$$

We can also write the eigenvector in a different gauge

$$u_{-}^{(2)}(\mathbf{k}) = \frac{1}{\mathcal{N}^{(1)}} \begin{pmatrix} H_z - \left|\vec{H}\right| \\ H_x + iH_y \end{pmatrix} \times \frac{\frac{H_z+\left|\vec{H}\right|}{H_x+iH_y}}{\left|\frac{H_z+\left|\vec{H}\right|}{H_x+iH_y}\right|} = \frac{1}{\mathcal{N}^{(2)}} \begin{pmatrix} -H_x + iH_y \\ H_z + \left|\vec{H}\right| \end{pmatrix}. \tag{6.47}$$

This wavefunction is well defined at the point $\mathbf{k}$ when $H_x = H_y = 0$ and $H_z > 0$. The singular point, nevertheless, appears when $H_x = H_y = 0$ and $H_z < 0$. Therefore we have to define the Bloch waves in the whole BZ with two different gauges, the wavefunction and Berry connection of two regions are connected by the gauge transformation

$$\begin{aligned} u_{-}^{(2)}(\mathbf{k}) &= u_{-}^{(1)}(\mathbf{k}) e^{i\varphi(\mathbf{k})}, \\ \mathbf{A}^{(2)}(\mathbf{k}) &= \mathbf{A}^{(1)}(\mathbf{k}) + \boldsymbol{\nabla}\varphi(\mathbf{k}), \end{aligned} \tag{6.48}$$

where the local phase $e^{i\varphi} = \frac{H_z+\left|\vec{H}\right|}{H_x+iH_y} \Big/ \left|\frac{H_z+\left|\vec{H}\right|}{H_x+iH_y}\right| = |H_x + iH_y| \,/(H_x + iH_y)$. One way to choose the boundary of two regions is to be very close to the point $\mathbf{K}_1$

$$e^{i\varphi} = \frac{|q_x - iq_y|}{q_x - iq_y} = e^{i\theta}, \tag{6.49}$$

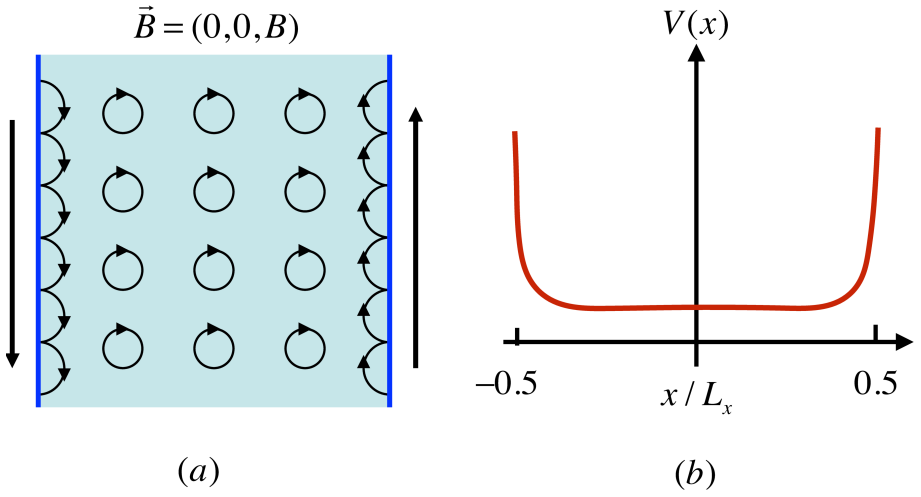

Figure 6.2: (a)Classical picture of the edge state in the IQHE. (b) The potential $V(x)$ along the finite dimension. It is flat in the within the bulk and has sharp slope in the both edges.

where $\mathbf{q} = \mathbf{k} - \mathbf{K}_1$. The Chern number C_- of the lower band in Eq. (6.30) is ready to be calculated

$$C_- = \frac{1}{2\pi}[\varphi(\theta = 2\pi) - \varphi(\theta = 0)] = 1. \tag{6.50}$$

6.4 Edge States

The Hall effect can be understood in a classical picture involving the concept of "edge states" in Fig. (6.2a) . In the 2D sample, the behavior of the electrons in magnetic field is dependent upon their locations, which can be generally separated into two regions: the bulk and the edge. Electrons in the bulk region are in cyclotron motion (say clockwisely), while near the edge of the sample, the orbits of motion must collide with the boundary. Since the motion has to be clockwise, the only option of the electron is to bounce back. The average result of the bouncing back motion is a uni-directional motion upwards (downwards) for the electron in the right (left) edge.

Consider a 2D sample with a finite dimension in x direction and an infinite dimension in y direction, we can model the sample by a potential $V(x)$ in Fig. (6.2b), which is flat

within the bulk and has sharp arise in the both edges. The potential can be expanded around the location x_0 of the LL,

$$V(x) \approx V(x_0) + \frac{\partial V}{\partial x}(x - x_0), \tag{6.51}$$

the slope $\partial V/\partial x$ plays exactly the same role of the electric field in Eq. (6.10). The drift velocity in the y direction can be obtained

$$v_y = -\frac{1}{eB}\frac{\partial V}{\partial x}. \tag{6.52}$$

In particular, we can read from the Fig, (6.2b), the states localized at both edges have opposite velocity, $v_y > 0$ on the left and $v_y < 0$ on the right. By introducing a chemical potential μ, states are filled into the available states. We label the states for the same LL with different momentum k, in other words the position of the states in the x direction, in Fig. (6.2b). In order to obtain the expectation value of the drifted velocity, we need to sum over all the filled states

$$\langle I_y \rangle = -e \int \frac{dk}{2\pi} v_y = \frac{e}{2\pi l_B^2} \int dx \frac{1}{eB}\frac{\partial V}{\partial x} = \frac{e}{h}\Delta\mu. \tag{6.53}$$

The Hall voltage $eE_x = \Delta\mu$, giving the Hall conductivity for a single Landau level

$$\sigma_{xy} = \frac{\langle I_y \rangle}{E_x} = \frac{e^2}{h}, \tag{6.54}$$

which is exactly the expected result of the Hall conductivity. In this picture, the current is totally carried by the edge states, which is metallic, instead of the insulating bulk states. The states on the two edge have opposite velocities and can be cancelled out in average without the external electric field. The applied electric field actually breaks the balance

and generates the non-vanishing Hall current.

In previous sections, we derive the charged particle response in 2D material without boundary. Both the translational operator in x direction T_x and y direction T_y commute with the system Hamiltonian, therefore the momentums k_x and k_y are good quantum numbers. We analysis the topological property of the Bloch states via Eqs. (6.26) & (6.30), which is the intrisic feature of the bulk band. This is the bulk approach. We can also understand the system in a finite size and study the edge states, which is the edge approach. Both pictures yield to the same physical phenomenon, which is so-called the bulk-edge correspondence [69].

7. THE HALDANE MODEL IN SUPERRADIANCE LATTICE*

7.1 The Haldane Hamiltonian

The 1D SL can be extended to a higher dimension lattice by increasing the mode number of the coupling field in the EIT scheme. Especially, we could introduce a three-mode coupling field to construct a 2D honeycomb lattice. The wavevectors of the three coupling modes are $\mathbf{k}_1 = -k_c\hat{x}$, $\mathbf{k}_2 = k_c(\hat{x} - \sqrt{3}\hat{y})/2$ and $\mathbf{k}_3 = k_c(\hat{x} + \sqrt{3}\hat{y})/2$, as shown in Fig. (7.1c) . The Dirac point is exactly the EIT point in the 2D SL. The hopping constant is the Rabi frequency of the coupling field while the on-site potential, the energy difference between the two sites in a unit cell, can be tuned by its frequency. Interesting physics based on the honeycomb lattice structure, the Haldane model for instance, can be studied upon the 2D SL.

In order to introduce the complex NNN interaction, like the ones in Eq. (6.37), we consider periodically modulated Rabi frequencies $\Omega_{1,2,3}$ of coupling fields,

$$\Omega_l = \Omega_s + 2\Omega_d \cos(\nu_d t + \phi_l) \tag{7.1}$$

where $l = 1, 2, 3$, $\Omega_s(\Omega_d)$ is the static (dynamic) components of the Rabi frequency Ω_l along $\mathbf{k}_l$, ν_d is the modulation frequency, and ϕ_l is the modulation phase for each mode respectively. The Hamiltonian of these TDS is (similar with the 1D lattice in Eq. (5.19))

$$H_I = \hbar \sum_{\mathbf{k}} [\frac{\Delta_c}{2}(|e_{\mathbf{k}}\rangle\langle e_{\mathbf{k}}| - |m_{\mathbf{k}-\mathbf{k}_1}\rangle\langle m_{\mathbf{k}-\mathbf{k}_1}|) + \sum_{l=1}^{3} \Omega_l |e_{\mathbf{k}}\rangle\langle m_{\mathbf{k}-\mathbf{k}_1}| + h.c.]. \tag{7.2}$$

where $\mathbf{k} = \mathbf{k}_p + r(\mathbf{k}_2 - \mathbf{k}_1) + s(\mathbf{k}_3 - \mathbf{k}_1)$ with integers r and s. Here we have assumed the

*Reprinted with permission from "Topological phase transitions in superradiance lattices," by D.-W. Wang, H. Cai, L. Yuan, S.-Y. Zhu, and R.-B. Liu, 2015, Optica, 2, 712-715 [70], Copyright 2017 by OSA

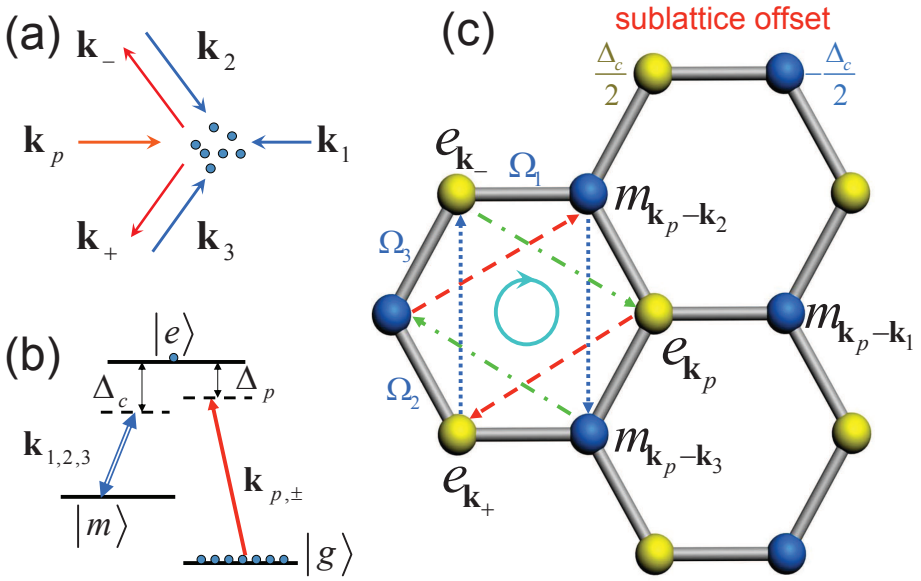

Figure 7.1: Realization of the Haldane model in a superradiance lattice of timed Dicke states in electromagnetically induced transparency. (a) Schematic configuration of the probe field $\mathbf{k}_p$, EIT coupling fields along $\mathbf{k}_{1,2,3}$, and diffraction fields along $\mathbf{k}_+ \equiv \mathbf{k}_1 - \mathbf{k}_3$and $\mathbf{k}_- \equiv \mathbf{k}_1 - \mathbf{k}_3$ (b) the energy level diagram of the EIT coupling, probe, and scattering fields, (c) honeycomb structure of the SL. $|e_{\mathbf{k}}\rangle$ and $|m_{\mathbf{k}}\rangle$ correspond to the two sublattices. The NNN hopping Ω_{31} (red solid arrows), Ω_{23} (blue dotted arrows), and Ω_{12} (green dashed– dotted arrows) enclose a nonzero effective magnetic flux in momentum space. The arrow on the circle denotes the direction of the excitation current when the Chern number $C = 1$.

size of the atomic ensemble to be much smaller than c/ν_d (where c is the speed of light) and hence neglected the position dependence of the modulation. On the other hand, the ensemble size is much larger than c/ν_c and the number of atoms $N \gg 1$ such that the TDSs in the SL are approximately orthogonal to each other, i.e., $\langle e_{\mathbf{k}}|e_{\mathbf{k}'}\rangle = \delta_{\mathbf{k}\mathbf{k}'}$ in Eq. (5.12). We assume the atoms be randomly distributed and their number is large enough to cover all possible points in the real space BZ. The size of the SL can be treated as infinite.

We expand the Hamiltonian in (7.2) by their temporal frequency, into static, positive and negative frequency components,

$$H = H_0 + H_+ e^{i\nu_d t} + H_- e^{-i\nu_d t} \tag{7.3}$$

where

$$H_0 = \hbar \sum_{\mathbf{k}} [\frac{\Delta_c}{2}(|e_{\mathbf{k}}\rangle\langle e_{\mathbf{k}}| - |m_{\mathbf{k}-\mathbf{k}_1}\rangle\langle m_{\mathbf{k}-\mathbf{k}_1}|) - \Omega_s \sum_{l=1}^{3} |e_{\mathbf{k}}\rangle\langle m_{\mathbf{k}-\mathbf{k}_1}| + h.c.], \tag{7.4}$$

$$H_+ = -\hbar\Omega_d \sum_{\mathbf{k}} (\sum_{l=1}^{3} \Omega_l e^{i\phi_l} |e_{\mathbf{k}}\rangle\langle m_{\mathbf{k}-\mathbf{k}_1}| + h.c.], \tag{7.5}$$

$$H_- = -\hbar\Omega_d \sum_{\mathbf{k}} (\sum_{l=1}^{3} \Omega_l e^{-i\phi_l} |e_{\mathbf{k}}\rangle\langle m_{\mathbf{k}-\mathbf{k}_1}| + h.c.]. \tag{7.6}$$

Note that $H_\pm$ are not Hermitian themselves, but H_+ is the Hermitian conjugate of H_-. It is the phase factor $e^{\pm i\phi_l}$ that plays the crucial role of generating the complex NNN interaction hopping term in SL.

The dynamics of the system is a Floquet problem. According to Floquet theorem (in Table. (5.1)), the wave function can be written as (similar with the Bloch theory)

$$|\Psi\rangle = e^{-i\varepsilon t/\hbar}|\psi(t)\rangle, \tag{7.7}$$

where ε is the quasi-energy. Due to the periodicity $\psi(t + 2\pi/\nu_d) = \psi(t)$,

$$|\psi(t)\rangle = \sum_n e^{in\nu_d t}|\psi_n\rangle. \tag{7.8}$$

Substituting the Eq. (7.2-7.8) to the Schrodinger equation, $i\hbar\partial|\Psi\rangle/\partial t = H|\Psi\rangle$, and collecting the terms with the same time evolution, We obtain

$$(\varepsilon - \hbar n\nu_d)|\psi_n\rangle = H_0|\psi_n\rangle + H_+|\psi_{n-1}\rangle + H_-|\psi_{n+1}\rangle. \tag{7.9}$$

The quasi-eigenenergy can be obtained by diagonalizing the above Hamiltonian.

For the sake of simplicity,we assume the separation between the Floquet sidebands is much larger than the bandwidth, $\nu_d \gg \Omega_{s,d}, \Delta_c$, where the perturbation theory can be applied [71]. When the probe field is near resonance, $\Delta_p = \omega_{eg} - \nu_p \ll \Omega_s$, where ω_{eg} is the transition frequency between e and g and ν_p is the probe field frequency, only the Floquet band with $n = 0$ in Eq. (7.9) is relevent. In other words, we ignore the side-band generation. For states with eigenfrequencies near $\varepsilon = 0$, the effective Hamiltonian can be obtained by standard second-order perturbation as

$$\varepsilon|\psi_0\rangle = H_{eff}|\psi_0\rangle \tag{7.10}$$

where $H_{eff} = H_0 + H'$ with NNN interaction

$$\begin{aligned} H' &= \frac{1}{\hbar\nu_d}(H_+H_- - H_-H_+), \\ &= \sum_{\mathbf{k}}\sum_{l\neq j}\hbar\Omega_{lj}|e_{\mathbf{k}+\mathbf{k}_l-\mathbf{k}_j}\rangle\langle e_{\mathbf{k}}| + h.c. + (e \to m, \mathbf{k} \to \mathbf{k} - \mathbf{k}_1), \end{aligned} \tag{7.11}$$

where $\Omega_{lj} = 2i\Omega'\sin(\phi_l - \phi_j)$ with $\Omega' = \Omega_d^2/\nu_d$. The crucial factor $i = e^{i\pi/2}$ comes from the quantum interference between the two pathways shown in Fig. (7.2a)

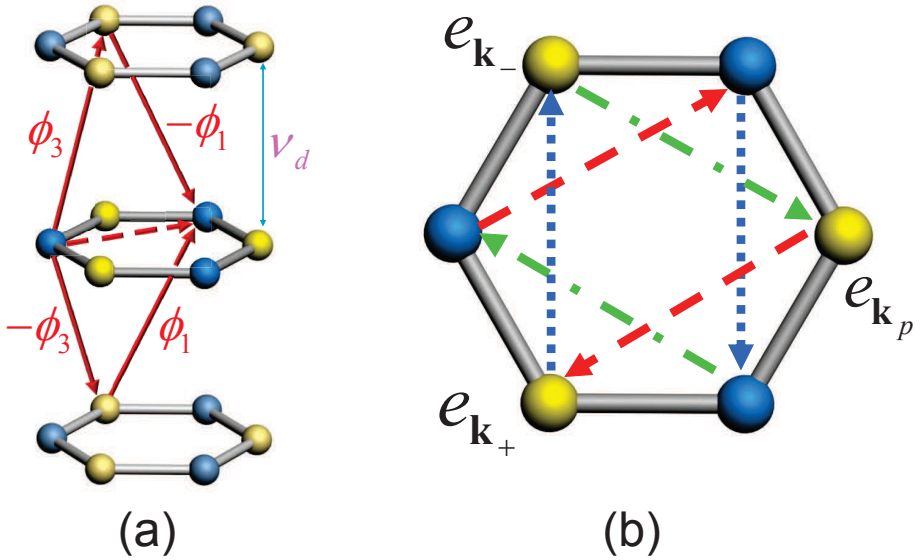

Figure 7.2: Complex next-nearest-neighbor hopping induced by Rabi frequency modulation. (a) The Floquet sidebands of the SL and the NNN transition Ω_{13} (dashed arrow) induced by the interference between two second-order inter-sideband transitions (solid arrow). Phases are labelled for each step. (b) The effective NNN transitions in a unit cell. The NNN hopping Ω_{31} (red arrow), Ω_{23} (blue dot arrow) and Ω_{12} (green dash dot arrow) enclose a nonzero effective magnetic flux.

The effective Hamiltonian is greatly simplified in the real-space representation. We denote the real-space basis states as

$$\begin{aligned} |e_{\mathbf{r}_i}\rangle &= |g_1, g_2 ... e_j ... g_N\rangle, \\ |m_{\mathbf{r}_i}\rangle &= |g_1, g_2 ... m_j ... g_N\rangle. \end{aligned} \tag{7.12}$$

The effective Hamiltonian can be written as

$$H_{eff} = \sum_j \mathbf{h}(\mathbf{r}_j) \cdot \boldsymbol{\sigma}_j \tag{7.13}$$

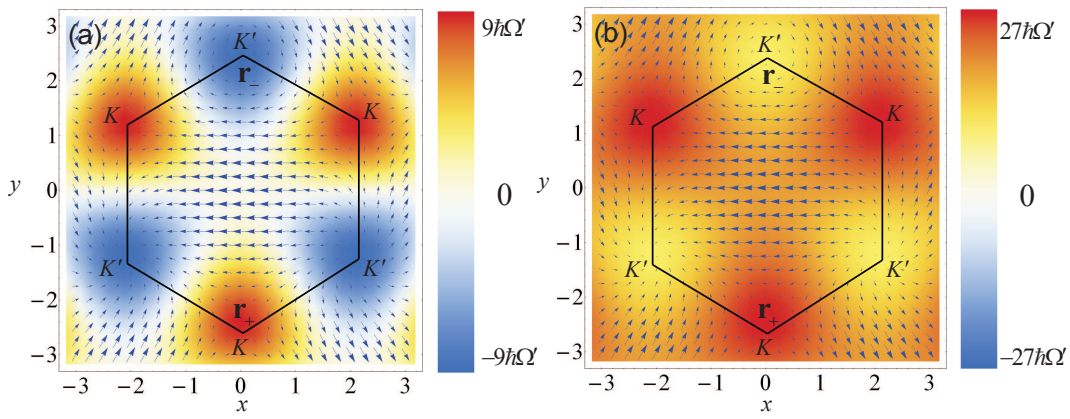

(a) (b)

Figure 7.3: Effective magnetic fields in a Brillouin zone for topological and trivial SL's. (a) A topological SL with $\Delta_c = 0$. (b) A trivial SL with $\Delta_c = 36\Omega'$. The arrows show the vector $h_x\hat{x} + h_y\hat{y}$ and the colours show h_z. The x and y axis are in unit of k_c^{-1}. The phase of the coupling field $\mathbf{k}_l$ is $\phi_l = (l-1)4\pi/3$ and $\alpha = 3\sqrt{3}/2$. Note that the K_1/K_2 points at the boundaries of the first Brillouin zone are equivalent.

where the effective magnetic field $\mathbf{h}(\mathbf{r}_j) = (h_x, h_y, h_z)$ with

$$h_x = -\hbar\Omega_s \sum_{l=1}^{3} \cos(\mathbf{r}_j \cdot \mathbf{k}_l) \tag{7.14}$$

$$h_y = \hbar\Omega_s \sum_{l=1}^{3} \sin(\mathbf{r}_j \cdot \mathbf{k}_l), \tag{7.15}$$

$$h_z = \frac{\hbar\Delta_c}{2} + 2i\hbar \sum_{l=1}^{3} \Omega_{(l+1)l} \sin[\mathbf{r}_j \cdot (\mathbf{k}_{l+1} - \mathbf{k}_l)] \tag{7.16}$$

and the pseudo spin $\boldsymbol{\sigma}_j = (\sigma_j^x, \sigma_j^y, \sigma_j^z)$ with the Pauli matrices for the jth atom defined as $\sigma_j^x = |e_{\mathbf{r}_j}\rangle\langle m_{\mathbf{r}_j}| + h.c.$, $\sigma_j^y = -i|e_{\mathbf{r}_j}\rangle\langle m_{\mathbf{r}_j}| + h.c.$ and $\sigma_j^z = |e_{\mathbf{r}_j}\rangle\langle e_{\mathbf{r}_j}| - |m_{\mathbf{r}_j}\rangle\langle m_{\mathbf{r}_j}|$. The effective magnetic field is exactly the ones in Haldane model in Eq. (6.41-6.43)

7.2 Chern Number

In Fig. (7.3) , we plot the effective magnetic field $\mathbf{h}$ for both (a) topological non-trivial

whose band gap is opened by the NNN hopping and (b) trivial SL by the on-site potential. At the K_1 point $\mathbf{r}_+ = -\frac{4\pi}{3\sqrt{3}k_c}(\frac{\sqrt{3}}{2}\hat{x} + \frac{1}{2}\hat{y})$ and K_2 point $\mathbf{r}_- = \frac{4\pi}{3\sqrt{3}k_c}(\frac{\sqrt{3}}{2}\hat{x} + \frac{1}{2}\hat{y})$, the band gaps are minimized, where

$$\sum_{l=1}^{3} e^{i\mathbf{r}_\pm \cdot \mathbf{k}_l} = 0 \tag{7.17}$$

and hence $h_x = h_y = 0$. At the symmetry points of the BZ the Hamiltonian is diagonalized

$$\mathcal{H}\mathbf{r}_\pm) = (\frac{\hbar\Delta_c}{2} \pm 2\sqrt{3}\Omega'\hbar\alpha)\sigma_z \tag{7.18}$$

where $\alpha = -\sum_{l=1}^{3}\sin(\phi_{l+1} - \phi_l)$. If we go from the K_1 point to K_2 point, $\mathbf{h}$ flip its sign, i.e., $\left|2\sqrt{3}\Omega'\hbar\alpha\right| > |\hbar\Delta_c/2|$. Then $\mathbf{h}$ moves from the north pole to the south pole of the Bloch sphere and we can't use one gauge to describe the whole BZ, therefore we obtain the non-trivial Chern number as 1 (following the argument in 6.3.2). If the onsite offset is large enough that the band gap is opened by the Δ_c, i.e., $\left|2\sqrt{3}\Omega'\hbar\alpha\right| < |\hbar\Delta_c/2|$, h_z keeps the same sign from K_1 point to K_2 point. $\mathbf{h}$ only covers a patch on the Bloch sphere and we can describe the whole BZ with one gauge, thus the single-valued Berry connection A has no singularities on a closed surface and the Chern number is zero. Generally, the Chern number of the upper band can be written as

$$C = \frac{1}{2}[\text{sign}(\Delta_c + 4\sqrt{3}\Omega'\alpha) - \text{sign}(\Delta_c - 4\sqrt{3}\Omega'\alpha)], \tag{7.19}$$

Specifically, when $\Delta_c = 0$, $C = \text{sign}(\alpha)$. The Chern number of the upper and lower bands C and C' are opposite. In Fig. (7.4a) , we plot α with $\phi_1 = 0$ and $0 \leq \phi_{2,3} \leq 2\pi$. The topological property of this SL Haldane model can be represented by the distribution of ϕ_l on a unit circle. There are two distinct topological configurations, counter-clockwise ϕ_1, ϕ_2 and ϕ_3 for $C = -1$ and clockwise ϕ_1, ϕ_2 and ϕ_3 for $C = 1$, as shown in Fig. (7.4b). The time reversal $t \to -t$ in Eq. (7.1) is equivalent to $\phi_l \to -\phi_l$, which leads to $C \to -C$.

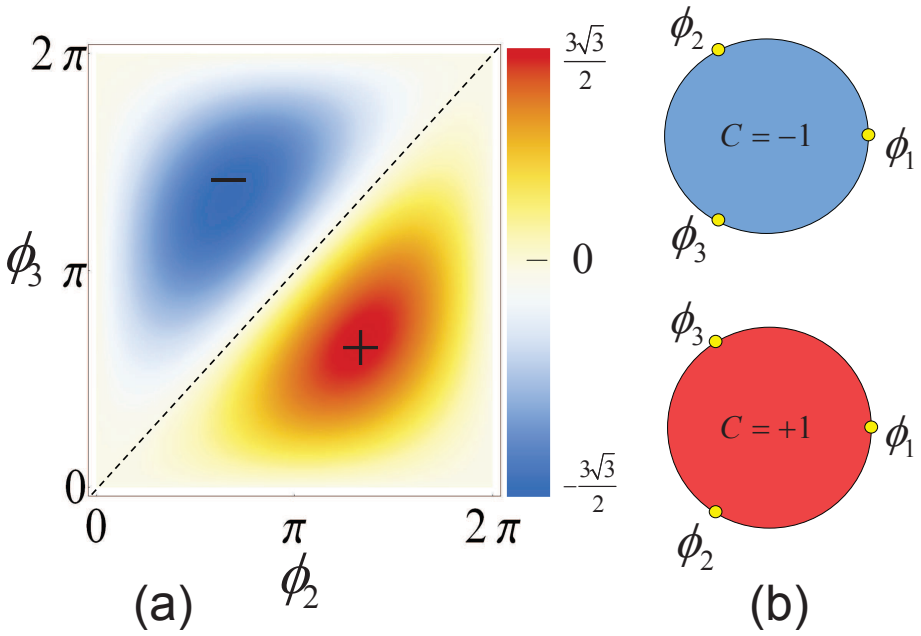

Figure 7.4: Topological phases of the superradiance lattice. (a) The value of α as a function of the modulation phases of the coupling fields ϕ_2 and ϕ_3. $\phi_1 = 0$. The $\pm$ signs are for the Chern numbers $C = \pm 1$. The dashed line separates the two topological phases. (b) The two Chern numbers corresponding to two topologically distinctive configurations of the three phase angles ϕ_1, ϕ_2, and ϕ_3 on a unit circle.

7.3 Optical Observable

Unlike TIs [29, 31], topological superradiance lattice (TSLs) have no outer edges in the semi-classical limit of the coupling fields. Neither do TSLs have Fermi surfaces. Nevertheless, the TSL has its unique topological properties that are observable. Some of the TDSs have directional superradiance emission. Of all the TDSs in the SL, only those $|e_{\mathbf{k}}\rangle$ with $|\mathbf{k}| = \omega_{eg}/c$ can satisfy momentum conservation, and have directional emission in $\mathbf{k}$ [7]. We call these states superradiant TDSs and the other ones subradiant TDSs. We can regard these superradiant TDSs as an inner edge of a honeycomb lattice of subradiant TDSs [72]. The topological orders lead to different light emissions from different superradiant TDSs. Alternatively, we can also tune the probe field frequency to test the topological band properties at certain energy, which is analogous to tuning the Fermi surface in a fermionic system.

7.3.1 Steady State

In the scheme of the three coupling field in Fig. (7.1a), we set the probe field vector to be $\mathbf{k}_p = -\mathbf{k}_1$. In this case we have only three superradiant TDSs with wavevectors $\mathbf{k}_p$, $\mathbf{k}_+ = -\mathbf{k}_3$ and $\mathbf{k}_- = -\mathbf{k}_2$. The excitation $|e_{\mathbf{k}_p}\rangle$ flows to $|e_{\mathbf{k}_\pm}\rangle$ and emits photons along $\mathbf{k}_\pm$. We denote the steady state probability amplitudes of states $|e_{\mathbf{k}_\pm}\rangle$ as $c_{\mathbf{k}_\pm}$, which can be obtained by solving the dynamic evolution of the system. Consider the total Hamiltonian including the probe field in real space,

$$\begin{aligned} H = &\sum_{j=1}^{N}(h_z - \hbar\tilde{\nu}_p)|e_{\mathbf{r}_j}\rangle\langle e_{\mathbf{r}_j}| - (h_z + \hbar\tilde{\nu}_p)|m_{\mathbf{r}_j}\rangle\langle m_{\mathbf{r}_j}| \\ &+ [(h_x - ih_y)|e_{\mathbf{r}_j}\rangle\langle m_{\mathbf{r}_j}| + h.c.] - [\hbar\Omega_p e^{i\mathbf{k}_p\cdot\mathbf{r}_j}|e_{\mathbf{r}_j}\rangle\langle G| + h.c.], \end{aligned} \tag{7.20}$$

with $\tilde{\nu}_p = \Delta_c/2 - \Delta_p$ being the probe detuning with respect to the middle of the band gap and Ω_p the probe field Rabi frequency. The wavefunction in the real space

$$|\Psi\rangle = c_G|G\rangle + \sum_{j=1}^{N} c_e(\mathbf{r}_j)|e_{\mathbf{r}_j}\rangle + \sum_{j=1}^{N} c_m(\mathbf{r}_j)|m_{\mathbf{r}_j}\rangle. \tag{7.21}$$

The dynamic equations of the probability amplitudes are

$$\begin{aligned}
\dot{c}_e(\mathbf{r}_j) &= [-\frac{i}{\hbar}(h_z - \hbar\tilde{\nu}_p) - \gamma_e]c_e(\mathbf{r}_j) \\
&\quad - \frac{i}{\hbar}(h_x - ih_y)c_m(\mathbf{r}_j) + i\Omega_p e^{i\mathbf{k}_p\cdot\mathbf{r}_j}c_G, \\
\dot{c}_m(\mathbf{r}_j) &= [\frac{i}{\hbar}(h_z + \hbar\tilde{\nu}_p) - \gamma_m]c_m(\mathbf{r}_j) \\
&\quad - \frac{i}{\hbar}(h_x + ih_y)c_m(\mathbf{r}_j),
\end{aligned} \tag{7.22}$$

where $\gamma_{e(m)}$ is the decoherence rate of $|e(m)\rangle$ states. In the limit of weak probe field $\Omega_p \ll \gamma_e$, we have $c_G \approx 1$. In the steady state, $\dot{c}_m = \dot{c}_e = 0$. Then we obtain

$$c_e(\mathbf{r}_j) = \frac{\hbar\Omega_p e^{i\mathbf{k}_P\cdot\mathbf{r}_j}}{h_z - \hbar\tilde{\nu}_p - i\hbar\gamma_e + \frac{h_x^2+h_y^2}{h_z+\hbar\tilde{\nu}_p+i\hbar\gamma_m}}. \tag{7.23}$$

In the SL coordinates, the wavefunction can be written as

$$|\Psi\rangle = c_G|G\rangle + \sum_{\mathbf{k}} c_{\mathbf{k}}|e_{\mathbf{k}}\rangle + c_{\mathbf{k}-\mathbf{k}_1}|m_{\mathbf{k}-\mathbf{k}_1}\rangle. \tag{7.24}$$

where the probability amplitude

$$c_{\mathbf{k}} = \langle e_{\mathbf{k}}|\Psi\rangle = \frac{1}{\sqrt{N}}\sum_{j=1}^{N} e^{-i\mathbf{k}\cdot\mathbf{r}_j}c_e(\mathbf{r}_j) \tag{7.25}$$

For uniformly distributed atoms, we can assume all points in the real space BZ are occupied by atoms, so the summation can be written as integration in the 1st BZ

$$c_k = \frac{\sqrt{N}}{S} \oiint_{BZ} c_e(\mathbf{r}) e^{-i\mathbf{k}\cdot\mathbf{r}} ds, \tag{7.26}$$

where S is the area of the first BZ.

7.3.2 Diffraction Contrast

We define the superradiance contrast

$$\eta = \frac{\left|c_{\mathbf{k}_+}\right|^2 - \left|c_{\mathbf{k}_-}\right|^2}{\left|c_{\mathbf{k}_+}\right|^2 + \left|c_{\mathbf{k}_-}\right|^2}. \tag{7.27}$$

For $C = 1$, the excitation current flows along $|e_{\mathbf{k}_P}\rangle \rightarrow |e_{\mathbf{k}_+}\rangle \rightarrow |e_{\mathbf{k}-}\rangle$ [72], as shown in the arrow direction of the blue circle in Fig. (7.1c). Since each TDS $|e_{\mathbf{k}}\rangle$ or $|m_{\mathbf{k}}\rangle$ has a decoherence rate γ_e or γ_m respectively, the excitation decays while flowing, and it is more probable in state $|e_{\mathbf{k}_+}\rangle$ than in state $|e_{\mathbf{k}_-}\rangle$. We therefore have $\eta > 0$. Similarly, for $C = -1$, $\eta < 0$. Thus the sign changes of the superradiance contrast signatures the topological phase transition, as seen in Fig. (7.5a) . The superradiance contrast in Fig. (7.5a) is consistent with Fig. (7.4b), except for the two diagonal corners where the topological currents are weak and the local effect inside a unit cell dominates.

We quantitatively compare the contrast between $\left|c_{\mathbf{k}_+}\right|^2$ and $\left|c_{\mathbf{k}_-}\right|^2$ in topological nontrivial and trivial SL. We assume $\tilde{\nu}_p = \gamma_m = 0$. Then Eq. (7.23) becomes

$$c_e(\mathbf{r}) = \frac{h_z}{h^2 - i\hbar h_z \gamma_e} \hbar \Omega_p e^{i\mathbf{k}_P \cdot \mathbf{r}}. \tag{7.28}$$

We assume $\Omega', \Delta_c \ll \Omega_s$ and thus $c_e(\mathbf{r})$ is highly centered at K_1 and K_2 points, where we

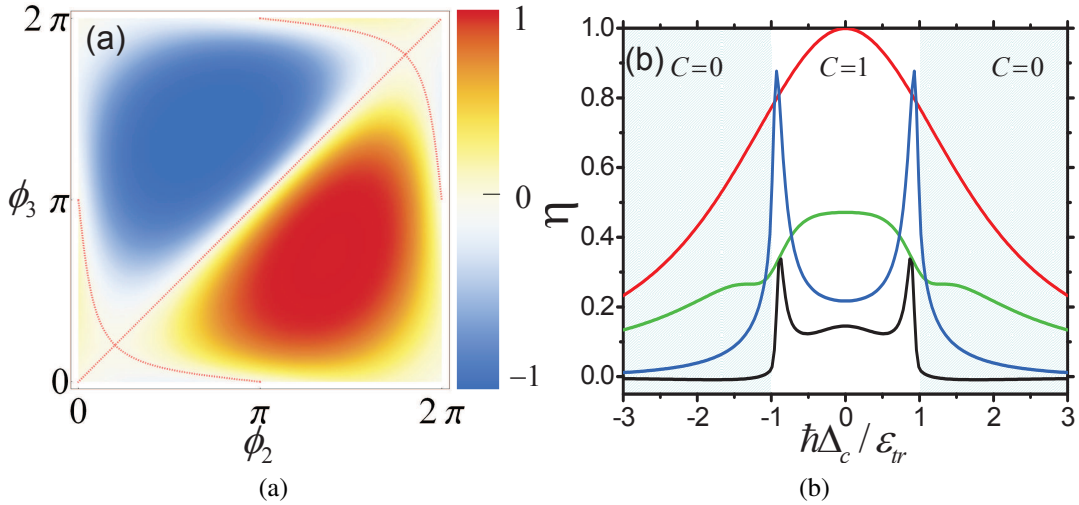

(a) (b)

Figure 7.5: Topological phase transition signatured by superradiance contrast. (a) The contrast η as a function of the modulation phases ϕ_2 and ϕ_3 with $\phi_1 = 0$. The red dotted lines are zero points. $\Delta_p = \Delta_c = 0$, $\Omega' = 0.01$. (b) The topological phase transition between $C = 1$ and 0. $\Delta_p = \Delta_c/2$, $\Omega' = 0.01$(red), 0.1(green), 0.5 (blue) and 1.0 (black). $\phi_1 = 0$, $\phi_2 = 4\pi/3$ and $\phi_3 = 2\pi/3$. For both figures, $\Omega_s = 3$, $\gamma_e = 1$, and $\gamma_m = 0.1$.

have $h_x = h_y = 0$ and

$$c_e = \frac{\hbar\Omega_p}{h_z - i\hbar\gamma_e} e^{i\mathbf{k}\cdot\mathbf{r}}, \tag{7.29}$$

The probability amplitude $c_{\mathbf{k}}$ can be approximately calculated by the integration of $c_e(\mathbf{r})$ in small areas near $\mathbf{r}_\pm$

$$c_{\mathbf{k}} \approx \frac{\sqrt{N}\hbar\Omega_p}{S}[e^{i(\mathbf{k}_p-\mathbf{k})\cdot\mathbf{r}_+}\int_{\mathbf{r}_+}\frac{dxdy}{h_z - i\hbar\gamma_e} + e^{i(\mathbf{k}_p-\mathbf{k})\cdot\mathbf{r}_-}\int_{\mathbf{r}_+}\frac{dxdy}{h_z - i\hbar\gamma_e}], \tag{7.30}$$

where the phase factor have been taken out of the integration since they do not have significant change in the small areas. For a topological non-trivial SL, where $\Omega' > 0$ and $\Delta_c = 0$, h_z has opposite sign at $\mathbf{r}_\pm$, We denote $\int_{\mathbf{r}_\pm}(h_z - i\hbar\gamma_e)^{-1}dxdy = \pm p + iq$. Thus

$$c_{\mathbf{k}} \approx 2i\frac{\sqrt{N}\hbar\Omega_p}{S}\{p\sin[(\mathbf{k}_p - \mathbf{k})\cdot\mathbf{r}_+] + q\cos[(\mathbf{k}_p - \mathbf{k})\cdot\mathbf{r}_+]\}. \tag{7.31}$$

For $\mathbf{k}_p = -\mathbf{k}_1$, $\mathbf{k}_+ = -\mathbf{k}_3$ and $\mathbf{k}_- = \mathbf{k}_2$, we have

$$\eta \approx \frac{2\sqrt{3}pq}{3p^2 + q^2}. \tag{7.32}$$

However, for a topological trivial SL, where $\Omega' = 0$ and $\Delta_c \neq 0$, h_z has the same sign at $\mathbf{r}_\pm$. We have $\int_{\mathbf{r}_\pm}(h_z - i\hbar\gamma_e)^{-1}dxdy = p + iq$ and

$$c_{\mathbf{k}} \approx 2i\frac{\sqrt{N}\hbar\Omega_p}{S}(p + iq)\cos[(\mathbf{k}_p - \mathbf{k}) \cdot \mathbf{r}_+]. \tag{7.33}$$

Therefore $c_{\mathbf{k}_+} = c_{\mathbf{k}_-}$ and $\eta = 0$.

7.3.3 Transient Light Propagation

The TSLs have unique features in transient light propagation under pulse probe. In Fig. (7.6) , we compare the pulse propagation in a trivial SL with zero Ω' and that in a TSL. For a weak probe pulse, the linear susceptibility is $\chi^{(1)} \propto c_{\mathbf{k}_p}$ and the linear absorption is $\mathrm{Im}\chi^{(1)}$. The two multiwave mixing signals along $\mathbf{k}_\pm$ correspond to the nonlinear susceptibilities $\chi_\pm \propto c_{\mathbf{k}_\pm}$ and can be understood as a result of optical grating[49]. We simulate the pulse propagation for the three modes along $\mathbf{k}_{p,\pm}$; using coupled wave equations (see section 3.2 and Appendix B). For a trivial SL without modulation, the light propagating along k is symmetric, while for a TSL with $C = 1$, the topological currents drive the probe pulse to $\mathbf{k}_+$, even if the NNN hopping is two orders of magnitude smaller than the nearest-neighbor hopping.

7.4 Experimental Proposal

TSLs can be readily realized in experiments for cold alkali atoms. Taking a 85Rb D1 line, for example, we can have $|g\rangle = |5^2S_{1/2}, F = 2\rangle$, $|e\rangle = |5^2P_{1/2}, F = 2\rangle$ and $|m\rangle = |5^2S_{1/2}, F = 3\rangle$, $\gamma_e = 2.9MHz$, and γ_m is controllable via an inhomogeneous

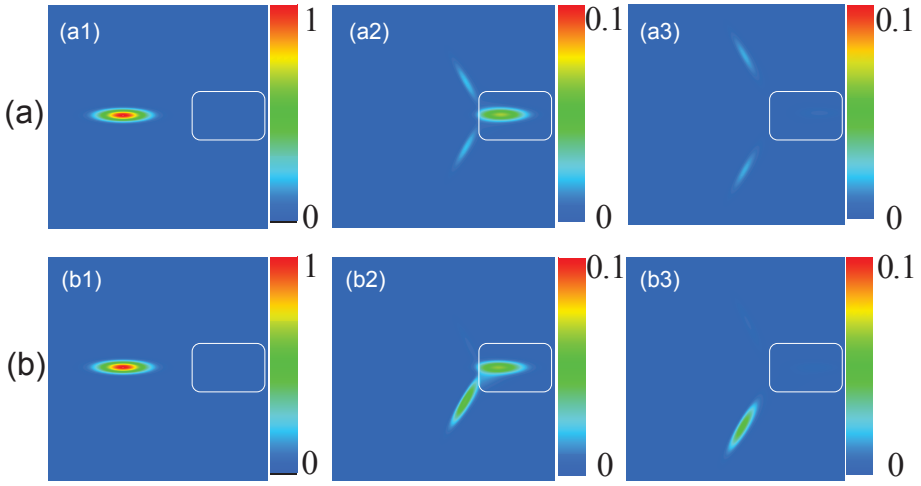

Figure 7.6: Real-space propagation of a light pulse through an atom ensemble driven into trivial or topological superradiance lattices. Diffraction of a weak Gaussian probe pulse in the $x-y$ plane for (a) a trivial SL with $\Omega_d = 0$ and (b) a TSL with $C = 1$. $\phi_1 = 0$, $\phi_2 = 4\pi/3$, $\phi_3 = 2\pi/3$, and $\Omega; = 0.01$. The derived linear and nonlinear susceptibilities are $\chi^{(1)} = i0.1410$, $\chi_+ = \chi_- = -i0.0522$ in (a) and $\chi^{(1)} = i0.1410$, $\chi_+ = -i0.1057$n $\chi_- = -i0.0021$ in (b). The parameters are such that $\Omega_s = 3$, $\Delta_p = \Delta_c = 0$, $\gamma_e = 1$, and $\gamma_m = 0.01$. The square denotes the area occupied by atoms. The three figures in each group are for scaled time $t = 1, 80, 100$, successively. We assume the group velocity to be uniform everywhere.

magnetic field. The Rabi frequency $\Omega_s = 3\gamma_e = 8.6MHz$ (intensity $25mW/cm^2$). The modulation frequency can be $\nu_d = 10\gamma_e = 28.8MHz$, which is large enough to separate the Floquet bands. One can trap 10^6 atoms in $1mm^3$ such that $N \gg 1$ and the size L of the ensemble $c/\nu_c \ll L \ll c/\nu_d$. In the μK regime, the thermal random motions have negligible Doppler shifts (approximately kilohertz). Another possible type of physical system is rare earth atoms doped in solids. One should first optically pump nearly all the population to $|g\rangle$ and then turn on three optical fields coupling $|e\rangle$ to $|m\rangle$, send in a weak field probing the $|g\rangle$ to $|e\rangle$ transition, and detect the diffraction signals.

8. MESOSCOPIC SUPERPOSITION STATES GENERATION IN FOCK-STATE LATTICES *

8.1 NOON State Generation

Deterministic generation of NOON states up to $N = 3$ was achieved by first creating entanglement between two resonators and then increasing their photon numbers [74]

$$|10\rangle \rightarrow |10\rangle + |01\rangle \rightarrow |20\rangle + |02\rangle \rightarrow |30\rangle + |03\rangle \tag{8.1}$$

However, once entanglement is created, decoherence accompanies the remaining process, which hinders the scaling up to high NOON states. Therefore, it is favorable to first create high photon number states before generating entanglement.

$$|10\rangle \rightarrow |20\rangle \rightarrow ...|N0\rangle \tag{8.2}$$

Then apply a beam-splitter-like operation $\mathcal{B}$

$$\mathcal{B} : |N0\rangle \rightarrow |N0\rangle + |0N\rangle. \tag{8.3}$$

The operation in (8.3) for $N = 1$ is well known for a 50-50 beam splitter. However, the case with $N \geq 2$ is absent as far as in our knowledge. We realize that, with the help of an ancillary control qubit (two-level atom), the following transformation that can implement

*Reprinted with permission from "Mesoscopic Superposition States Generated by Synthetic Spin-Orbit Interaction in Fock-State Lattices," by D.-W. Wang, H. Cai, R.-B. Liu, and M. O. Scully, 2016, Phys. Rev. Lett. 116, 220502 [73], Copyright 2017 by APS

the operation $\mathcal{B}$ and generate NOON states from number states:

$$a_0 \rightarrow a_1|e\rangle\langle e| + a_2|g\rangle\langle g| \tag{8.4}$$

where a_j ($j = 0, 1, 2$) are the annihilation operators of three cavities, and $|e\rangle$ and $|g\rangle$ are the excited and ground states of a two-level atom. The photon state of a cavity is transferred to either one of two other cavities depending on the atomic states.

The significance of this transformation is manifested in achieving various types of mesoscopic superposition states from number states or coherent states. We initially prepare an unentangled state

$$|\psi\rangle = \frac{1}{\sqrt{2}}|N, 0, 0\rangle(|e\rangle + |g\rangle), \tag{8.5}$$

where $|N, 0, 0\rangle$ indicates that the first cavity contains N photons, while the other two cavities are in the vacuum state. After the transformation in Eq. (8.4), the state becomes

$$\mathcal{B} : |\psi\rangle \rightarrow \frac{1}{\sqrt{2}}(|0, N, 0\rangle|e\rangle + |0, 0, N\rangle|g\rangle), \tag{8.6}$$

which is a micro-macro entangled state [75, 76]. Applying a $\pi/2$ pulse to the above state yields $[(|0, N, 0\rangle - |0, 0, N\rangle)|e\rangle + (|0, N, 0\rangle + |0, 0, N\rangle)|g\rangle]/2$, in which the cavities are in different NOON states for different atomic states. If initially the first cavity is in a coherent state $|\alpha, 0, 0\rangle$, the final photon state are $(1/\sqrt{2})(|0, \alpha, 0\rangle \pm |0, 0, \alpha\rangle)$, i.e., entangled coherent states [77].

NOON states can also be realized without being entangled with the atom at the end, as shown in Fig. (8.1). We first prepare the state $|\psi_0\rangle = |g\rangle|N, 0, 0\rangle$, and all of the cavities but a_0 are initially out of resonance. After a $\pi/2$ Rabi rotation between a_0 and the atom, $|\psi_1\rangle = (1/\sqrt{2})(|g\rangle|0, 0, N\rangle - |e\rangle|N - 1, 0, 0\rangle)$. Then we modulate the cavity

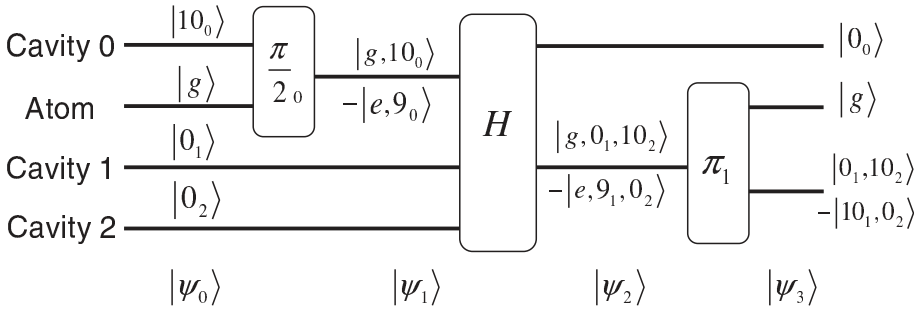

Figure 8.1: Quantum circuit of the scheme preparing NOON states. The scheme is valid for an arbitrary N and we take $N = 10$ here. Each line represents an inseparable quantum state. n_j is the n Fock state of the cavity mode j. The blocks θ_j represent the θ Rabi rotation of the atom interacting with the cavity j. H represents the evolution with the interaction Hamiltonian in Eq. (8.7) for time T. $|\psi\rangle$ is the direct product of the quantum states at each stage. We omit the normalization factors for superposition states.

frequencies and, after time T, $|\psi_2\rangle = (1/\sqrt{2})(|g\rangle|0,0,N\rangle - |e\rangle|0,N-1,0\rangle)$. We then tune all cavities but a_1 out of resonance. After a π Rabi rotation between a_1 and the atom, the final state is $|\psi_3\rangle = (1/\sqrt{2})|g\rangle(|0,0,N\rangle - |0,N,0\rangle)$. If we replace the number state $|N,0,0\rangle$ with the coherent state $|\alpha,0,0\rangle$, we can prepare the entangled coherent state $(1/\sqrt{2})(|0,0,\alpha\rangle - |0,\alpha,0\rangle)$ with small discrepancies due to the different Rabi frequencies of different number states, which can be neglected when α is large (see the Appendix C for the discrepancy and the cat state preparation).

8.2 Hamiltonian

8.2.1 Effective Hamiltonian

The transformation in Eq. (8.4) can be obtained by the following Hamiltonian:

$$H = i\hbar\kappa\sigma_z \sum_{j=0}^{2} a_{j+1}^{\dagger} a_j + h.c., \tag{8.7}$$

where the cavity index is cyclic, $\hbar$ is the reduced Planck constant, κ is a real-number coupling constant, and $\sigma_z = |e\rangle\langle e| - |g\rangle\langle g|$ is the z component of the pseudospin Pauli

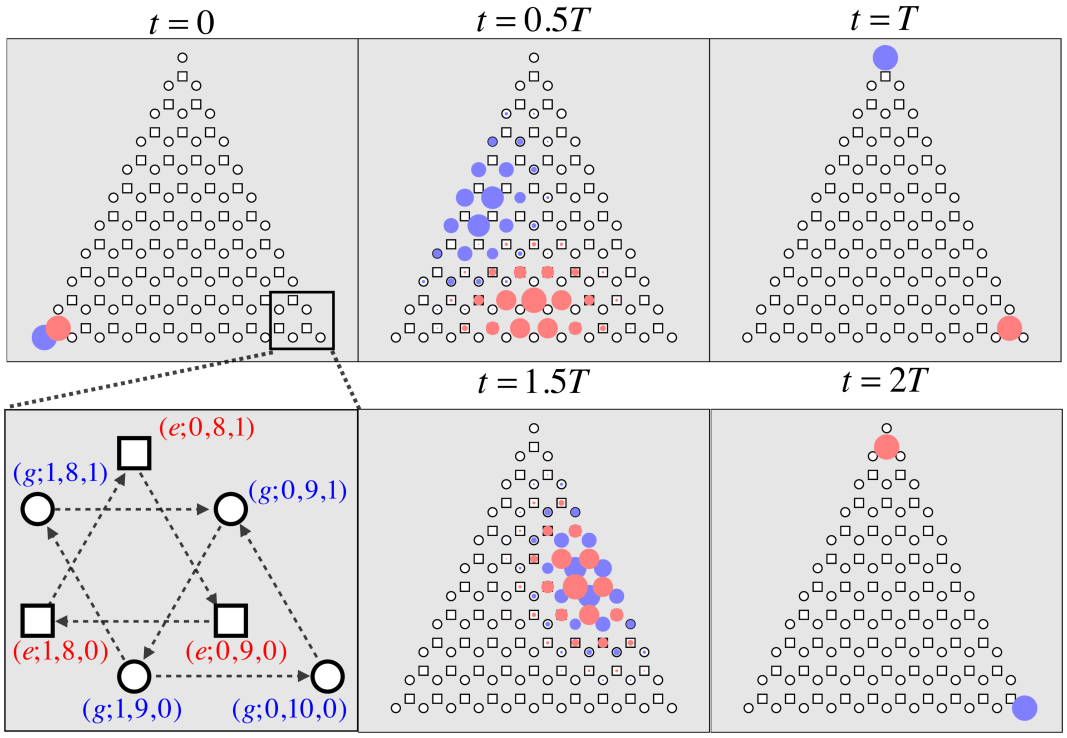

Figure 8.2: The dynamic evolution of a quantum state in the Fock-state lattice. The empty circles (squares) denote the $|g\rangle(|e\rangle)$ sublattice. The radius of the blue (red) filled circles denote the probabilities (rescaled in each frame) of the quantum states on the $|g\rangle(|e\rangle)$ sublattice. The photon numbers of the states are as denoted in the enlarged figure. The arrows denote the transitions attached with the phase factor $-i$. Up and down triangles in the same sublattice have opposite fluxes. Up triangles in the two sublattices also have opposite fluxes. The lattice contains ten excitations; i.e., $N = 10$. The initial state $|\psi\rangle$ i at $t = 0$ is a superposition of $|g\rangle|10, 0, 0\rangle$ and $|e\rangle|9, 0, 0\rangle$, which travel in opposite directions on the two sublattices

matrices of the atom. H can be regarded as a spin-orbit-coupled Hamiltonian of a Fock-state lattice, in the left-down corner of Fig. (8.2), where the directions of photon currents depend on the pseudospin state of the atom, as will be shown later. The Hamiltonian can be diagonalized,

$$H = -2\hbar\kappa\sigma_z \sum_{j=0}^{2} \sin(\frac{2j\pi}{3}) b_j^\dagger b_j, \tag{8.8}$$

with $b_j = (1/\sqrt{3}) \sum_{j=0}^{2} \exp(ijj'2\pi/3) a_{j'}$. The eigenfrequencies of the eigenmodes $b_{0,1,2}$ are linearized, i.e., $\omega_0 = 0$, $\omega_1 = -\sqrt{3}\kappa\sigma_z$ and $\omega_2 = \sqrt{3}\kappa\sigma_z$. The evolution of a_0 is

$$\begin{aligned} a_0(t) &= \frac{1}{\sqrt{3}} \sum_{j=0}^{2} e^{-i\omega_j t} b_j(0), \\ &= \frac{1}{3} \sum_{j=0} [1 + 2\cos(\sqrt{3}\kappa\sigma_z t + \frac{2j\pi}{3})] a_j(0), \end{aligned} \tag{8.9}$$

which yields $a_0(T) = a_1(0)|g\rangle\langle g| + a_2(0)|e\rangle\langle e|$ at $T \equiv 2\pi/3\sqrt{3}$. Similar equations of a_1 and a_2 lead to $a_0(0) = a_1(T)|e\rangle\langle e| + a_2(T)|g\rangle\langle g|$, i.e., Eq. (8.4).

One important feature of H that realizes the above transformation rests in the complex coupling coefficient $i\kappa$, which introduces an effective magnetic field in the pseudolattice formed by the Fock states of the three cavities, as shown in Fig. (8.2) and discussed later. This synthetic magnetic field for photons breaks the time reversal symmetry and creates an optical circulator, which can be generated in circuit QED architectures [78, 79] and parametrically modulated coupled resonators [80]. Another key feature of our scheme is that the chirality of the circulator is the opposite for $|e\rangle$ and $|g\rangle$ states due to the factor σ_z in Eq. (8.7). If $\kappa > 0$, the ground state mode is b_1 for the $|e\rangle$ state and b_2 for the $|g\rangle$ state. b_1 and b_2 are photonic modes with opposite quasimomenta, which drive the rotation in Eq. (8.9).

8.2.2 Effective Hamiltonian Realization

The Hamiltonian H in (8.8) can be realized in three cavities with modulated frequencies $\nu_j = \nu + \Delta \sin(\nu_d t - 2j\pi/3)$ coupled to the same two-level system. The Hamiltonian under the rotating wave approximation is

$$V = \frac{\hbar\omega}{2}\sigma_z + \sum_{j=0}^{2} \hbar\nu_j(t) a_j^\dagger a_j + \sum_{j=0}^{2} (\hbar g_v \sigma^+ a_j + h.c.), \tag{8.10}$$

with ω being the atomic transition frequency, $\nu_j(t)$ the time-dependent cavity frequency, g_v the vacuum Rabi frequency between the cavities and the atom, and $\sigma^+ = |e\rangle\langle g|$ the atomic raising operator. The frequency of the cavity j is periodically modulated $\nu_j(t) = \nu + \Delta \sin(\nu_d t + \phi_j)$ with Δ being the modulating amplitude, ν_d the modulating frequency and ϕ_j the modulating phase. We transform the wave function $|\psi\rangle$ into a rotating frame,

$$|\psi_I\rangle = U_0(t)|\psi\rangle \tag{8.11}$$

where

$$U_0(t) = e^{i/\hbar \int V_0(t')dt'} = \exp(i\frac{\omega}{2}t\sigma_z + i\sum_{j=0}^{2}[\nu_j t - f\cos(\nu_d t + \phi_j)]a_j^\dagger a_j), \tag{8.12}$$

with the $V_0(t) = \hbar\nu\sigma_z/2 + \sum_{j=0}^{2} h\nu_j(t) a_j^\dagger a_j$. The Schrödinger equation of $|\psi_I\rangle$ is $i\hbar\partial|\psi_I\rangle/\partial t = H_I|\psi_I\rangle$ with the interaction Hamiltonian

$$H_I = U_0(t) V U_0^{-1}(t) - V = \hbar\delta\frac{\sigma_z}{2} + \sum_{j=0}^{2} \hbar g_v \sigma^+ a_j e^{if\cos(\nu_d t + \phi_j)} + h.c., \tag{8.13}$$

where $\delta = \omega - \nu$ being the detuning of the field and the atom and $f = \Delta/\nu_d$ is a dimensionless parameter. Using the relationship

$$e^{if\cos(\nu_d t+\phi_j)} = \sum_{-\infty}^{\infty} i^n J_n(f) e^{in(\nu_d t+\phi_j)}, \tag{8.14}$$

where $J_n(f)$ is the nth order Bessel function of the first kind, we expand the interaction Hamiltonian by the temporal frequency $H_I = H_0 + \sum_n H_n e^{in\nu_d t}$, and

$$H_0 = \hbar\delta\frac{\sigma_z}{2} + \hbar g_v J_0(f)\sum_{j=0}^{2}\sigma^+ a_j + h.c., \tag{8.15}$$

$$H_n = \hbar g_v i^n J_n(f)\sum_{j=0}^{2}[\sigma^+ a_j + (-1)^n a_j^+\sigma^-]e^{in\phi_j}. \tag{8.16}$$

Note that H_n is the Hermitian conjugate of H_{-n} instead of itself. Then we use the similar approximation in Sec. (7.1). If the separation between the Floquet sidebands is large $\nu_j \gg \sqrt{N}g_v, \delta$, the second order perturbation theory is applied. The effective Hamiltonian is

$$H_I = H_0 + H, \tag{8.17}$$

and

$$H = \sum_{n=1}^{\infty}\frac{1}{n\hbar\nu_d}[H_n, H_{-n}] = i\hbar\sigma_z\sum_{j=0}^{2}\kappa a_{j+1}^\dagger a_j + h.c., \tag{8.18}$$

where $\kappa = g_v^2\beta(f)/\nu_d$ and $\beta(f) = \sum_{n=1}^{\infty} 2J_n^2(f)\sin[n(\phi_j - \phi_{j+1})]/n$. Given $\phi_j = -2\pi j/3$, $\delta = 0$ and $J_0(f) = 0$ with $f = 2.40$, we obtain $\beta \approx 0.307$ and $H_I = H$ is the desired effective Hamiltonian in Eq. (8.8).

Other than modulating the cavity frequencies (FM), we can alternatively modulate the coupling strength (AM) between the cavity j and the atom, $g_j(t) = 2g_v\cos(\nu_d t + \phi_j)$. There are only two Fourier components of the Hamiltonian, i.e., $H_n = H_1\delta_{1n} + H_{-1}\delta_{-1n}$.

Substitute $H_{\pm 1}$into Eq. (8.18), we obtain H with $\kappa = \sqrt{3} g_v^2/\nu_d$.

8.3 Chirality and Haldane Model

Helical currents exist in the lattice composed of the photon number states of the three cavities, as shown in Fig. (8.2). The effective Hamiltonian $H_I = H_0 + H$ conserves the total excitation number $N = \sum_{j=0}^{2} n_j + (\sigma_z + 1)/2$, where $n_j = a_j^\dagger a_j$. The quantum states with constant N form a finite triangular lattice. One of the n_j's is zero on each of the three triangular boundaries. This lattice has a similar structure to the Haldane model ([26] and Sec. (7.1)), with site-varying coupling coefficients. For example, there are periodic magnetic fluxes, which are the key for topological insulators and helical edge states [27]. The up and down triangles in the same sublattice have the opposite effective magnetic flux. Because of the triangular boundaries, up triangles outnumber down triangles by the total number of photons and there are net fluxes in each of the whole sublattices, which are particularly obvious near the edges. The quantum states $|e\rangle|N-1,0,0\rangle$ and $|g\rangle|N,0,0\rangle$ travel near the edges in opposite directions, which results from the opposite net local effective magnetic field in the two sublattices.

We can understand the helical transportation from the dispersion relation in the eigenspace of normal modes. The initial state is $|N,0,0\rangle = (a_0^\dagger)^N |vac\rangle/\sqrt{N!}$, where $|vac\rangle$ is the vacuum state. Since $a_0 = (1/\sqrt{3}) \sum_{j=0}^{2} b_j$, we expand $|N,0,0\rangle$ in the basis of the normal modes b_j,

$$\begin{aligned} |N,0,0\rangle &= \frac{1}{\sqrt{N! 3^N}} (b_0^\dagger + b_1^\dagger + b_2^\dagger)^N |vac\rangle, \\ &= \sum_{m_i} \sqrt{\frac{N!}{3^N m_0! m_1! m_2!}} |m_0, m_1, m_2\rangle_b, \end{aligned} \tag{8.19}$$

where $|m_0, m_1, m_2\rangle_b$ constrained by $\sum_{j=0}^{2} m_j = N$ are the photon number states in b_j mode. The factor $N!/m_0!m_1!m_2!$ reaches its maximum at $m_0 \approx m_1 \approx m_2 \approx N/3$. The states with these photon number are concentrated near the corners and edges of the

photon number lattice of the a_j mode. The energy and the quasimomentm of the state $|m_0, m_1, m_2\rangle_b$ are $E = \sqrt{3}\hbar\kappa\sigma_z(m_2 - m_1)$ and $p = 2\pi\hbar(m_2 - m_1)/3$, where the direction in $a_0 \to a_1 \to a_2$is defined as positive and the distance between two a_j mode is one.

The group velocity is, therefore,

$$v_g = \frac{\partial E}{\partial p} = \frac{3\sqrt{3}\kappa\sigma_z}{2\pi} = \frac{\sigma_z}{T}. \tag{8.20}$$

After time T, the photons are transported from mode a_0 to a_1 when $\sigma_z = 1$ and to a_2 when $\sigma_z = -1$, which is consistent with the conclusion of Eq. (8.9).

In our previous study on topological superradiance lattices in Section 7, plane wave modes were coupled with extended ensemble of atoms and the superradiance momentum states of atoms formed the approximately infinite lattice structures. Here, we have a single atom coupled with cavity modes. Cavity photon number states form the lattice structures, which contain edges determined by quantum electrodynamics (no negative photon number states exist). In this finite lattice, the hopping rates depend on the sites, which is an inherit property of the annihilation operators. However, the helical currents are robust to the site-varying coupling strength. Moreover, this results in the synchronized and nondispersive ($\partial E/\partial p = E/p$ and $\partial^2 E/\partial p^2 = 0$) transportation of different number states. At $t = mT$, with m being an integer, the excitation concentrates on one lattice site at one of the three corners, while in a lattice with homogeneous coupling strengths, the excitation is scattered by the corners and distributed all over the lattice for a large t. In order to see the effect of this inhomogeneity, we use a Hamiltonian $H(x)$ defined as

$$\begin{aligned}
\langle n_1 - 1, n_2, n_3|H(x)|n_1, n_2 - 1, n_3\rangle &= i\hbar\kappa\sigma_z[x\sqrt{n_1 n_2} + (1-x)N/3], \\
\langle n_1, n_2 - 1, n_3|H(x)|n_1, n_2, n_3 - 1\rangle &= i\hbar\kappa\sigma_z[x\sqrt{n_2 n_3} + (1-x)N/3], \\
\langle n_1, n_2, n_3 - 1|H(x)|n_1 - 1, n_2, n_3\rangle &= i\hbar\kappa\sigma_z[x\sqrt{n_3 n_1} + (1-x)N/3],
\end{aligned} \tag{8.21}$$

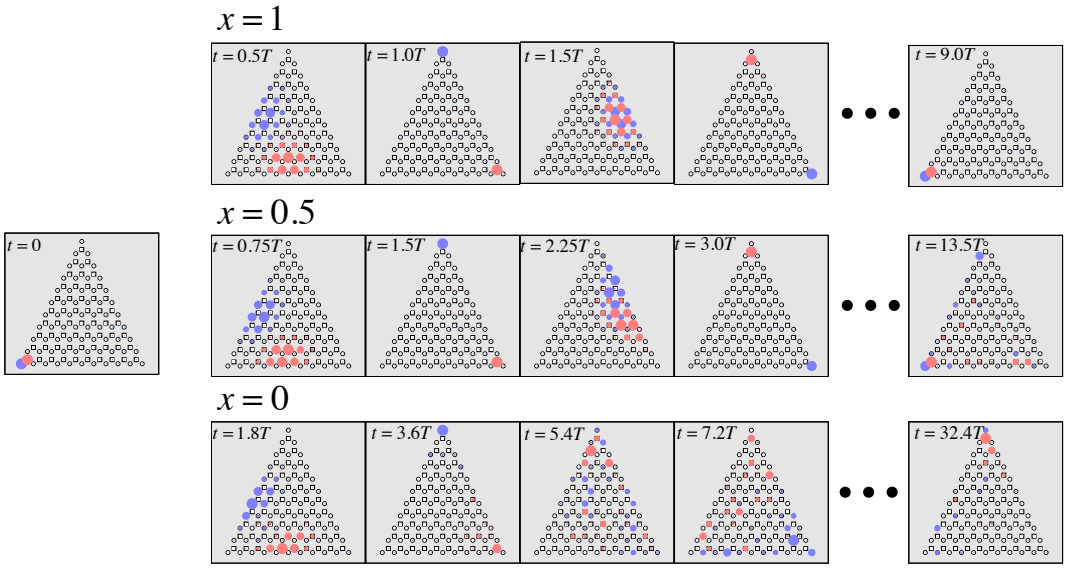

Figure 8.3: The effect of the inhomogeneous coupling strength in the helical transportation. Top: $x = 1$ for the Hamiltonian in Eq. (8.7). Bottom: $x = 0$ for a lattice with homogeneous coupling strengths. Middle: $x = 0.5$. The probabilities of the quantum states are proportional to the radius of the circles on the corresponding sites (rescaled for each frame), blue for the $|g\rangle$ and red for the $|e\rangle$ states.

where $N/3$ is the average coupling strength. We use a parameter $0 \leq x \leq 1$ to tune the inhomogeneity. When $x = 0$, it is the lattice with homogeneous coupling strength $N/3$. When $x = 1$, it is the photon number lattice of the Hamiltonian in Eq. (8.7).

In Fig. (8.3) , we plot the evolution of the initial state $(|10, 0, 0\rangle|g\rangle + |9, 0, 0\rangle|e\rangle)/\sqrt{2}$ with $x = 1$, 0.5, and 0. While the helicity of the transportation is maintained for different x, the inhomogeneity of the coupling strengths has two effects. First, the excitation periodically concentrates on one of the three corner sites for $x = 1$ (when $t = mT$ with m an integer). This is due to the linear dispersion in the energy spectrum, i.e., $\partial E/\partial p = E/p$ is a constant as shown in Eq. (8.20). On the other hand, when $x = 0$, the excitation is scattered by the corners and tends to distribute all over the lattice. Second, the transportation concentrates more on the edge for the homogeneous coupling strengths when $x = 0$. The inhomogeneity shifts the transportation into the bulk area of the lattice.

8.4 Experimental Proposal

We analyze the experimental feasibility and the robustness of this scheme against noises. High number Fock states can be prepared on demand in various cavity systems [81, 82, 83, 74, 84, 85]. For example, we can couple three superconductor resonators to the same superconducting phase qubit, where Fock states up to photon number 15 can be achieved [74]. The qubit relaxation and dephasing times are typically tens of microseconds [86, 87]. The coupling strength between the qubit and the resonators can be hundreds of megahertz [88, 89]. The single photon relaxation time of fixed frequency resonators can be milliseconds [90]. Tunable resonators based on kinetic inductance can also have a relaxation time as long as $6\mu s$ [91]. The time modulation of the resonator frequencies can be realized by tuning a superconducting quantum interference device coupled to the resonators as those in the dynamic Casimir effect [92, 93] or by permittivity modulation in parametrically modulated resonators [80].We adopt parameters that are typically achievable in superconductor circuit experiments [83, 64] and simulate the same process as in Sec. (8.2) but with dissipation. The evolution of the density matrix components on the target state $\langle\psi_2|\rho(t)|\psi_2\rangle$ is plotted in Fig. (8.4) . It is clear that at time $t = T$, the density matrix has a major overlap with the target state $|\psi_2\rangle$.

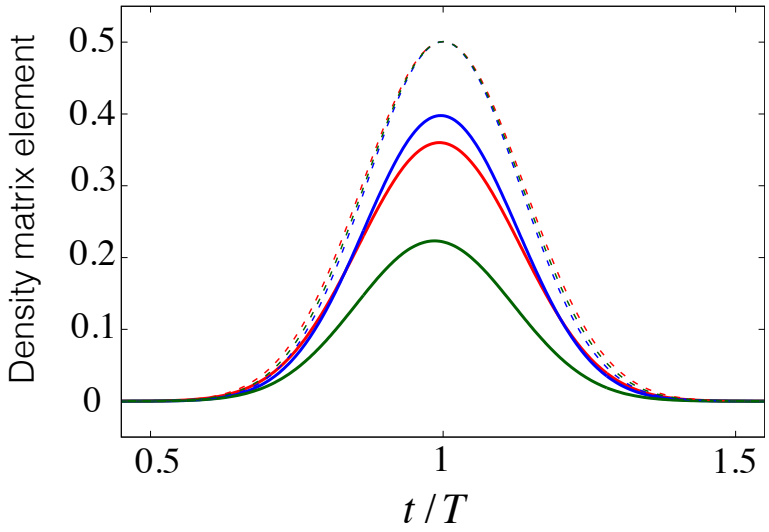

Figure 8.4: Evolution of the density matrix elements with (solid lines) and without (dashed lines) dissipation, $\langle e;0,9,0|\rho(t)|e;,0,9,0\rangle$ (red lines), $\langle g;0,0,10|\ \rho(t)|e;,0,0,10\rangle$ (blue lines), and $|\langle e;0,9,0|\rho(t)|g;,0,0,10\rangle|$ (green lines). The relaxation and pure dephasing times of the two-level system are 650 and $150ns$, respectively. The cavity relaxation time is $3.47\mu s$. $T = 80ns$.

9. SYNTHETIC MAGNETIC FIELD IN THERMAL VAPOR

9.1 Introduction

Charged particles in a gauge field such as a magnetic field have fascinating quantum properties like the quantum Hall effect [94], which reveals a new class of matter, namely, the topological insulators [26, 27, 28] that have an insulating bulk and conducting edges. The existence of the defect-immune edge states is guaranteed by a topological property, i.e., the Chern numbers of a gauge field. Neutral particles such as atoms, when trapped and dressed by light, can also be subjected to a synthetic gauge field [95, 96] with tunable physical parameters. Chiral edges states with synthetic gauge field for neutral fermions [97] and bosons [98, 99] have been recently observed in ultracold atoms.

Here we investigate the chiral currents of edge states in hot atoms, which are usually thought unsuitable because of the thermal effects. The triangular lattice structure we utilized is very similar to well studied two [100] or three [97, 99] lag ladder structure and zigzag optical lattice [101]. Different from the lattices in previous studies, spatial dimension is absent in our quantum Hall ribbon [102], which is usually fulfilled by optical lattice to introduce periodicity into atomic spatial distribution. The ribbon is a quasi one-dimensional lattice structure solely composed by two infinite edges, which is the simplest model that can be studied for chiral edge states. Our ribbon is a superradiance lattice [49], the hybrid lattice has two synthetic dimensions from two different origins: lattices along the edge indicate the number of momentum quanta transferred from photons to atoms; the internal degree freedom of atomic states are used to encode an extra dimension in the short axis. The effective magnetic field is introduced by the spatial phases difference of two standing waves, i.e., the relative positions of their nodes. The chiral transportation is robust to both the Doppler shift and the collisional broadening induced by the atomic

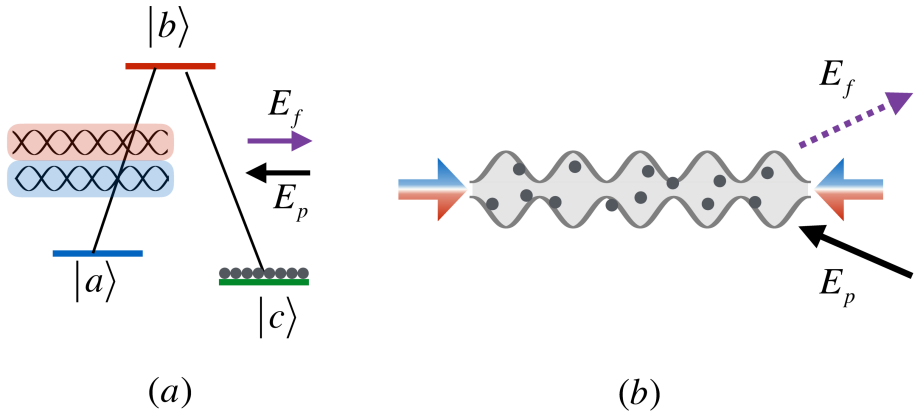

Figure 9.1: (a) Atomic level scheme of EIT. (b) Schematic figure of the wave-mixing process.

motion in our calculation. It can be tested by the reflectance of a probe field sent to atoms.

9.2 Hamiltonian

The simplest structure of EIT is an ensemble of Λ-type three-level atoms with the ground state $|c\rangle$, the excited state $|b\rangle$ and the metastable state $|a\rangle$. In order to generate synthetic magnetic field within the superradiance lattice, the states $|b\rangle$ and $|c\rangle$ are coupled by two standing waves with different frequency, the field of the near-resonant standing wave is $2E_1 \sin\nu_1 t \cos k_1 x$ while the far-detuning one is $2E_2 \sin\nu_2 t \cos(k_2 x + \theta/2)$. Their spatial periodicity has a phase difference $\theta/2$. With resonant probe and coupling fields, the effective Hamiltonian is (see Appendix D, $\hbar = 1$),

$$\begin{aligned} H_{\text{eff}} = &\sum_m (2\kappa \cos(2\mathbf{k}_c \cdot \mathbf{r}_m + \theta))(|b_m\rangle\langle b_m| - |a_m\rangle\langle a_m|) \\ &+ \sum_m 2\Omega_1 \cos(\mathbf{k}_c \cdot \mathbf{r}_m)(|b_m\rangle\langle a_m| + h.c.) \\ &+ \sum_m \Omega_p e^{i\mathbf{k}_p \cdot \mathbf{r}_m} |b_m\rangle\langle c_m| + h.c.. \end{aligned} \tag{9.1}$$

where $\mathbf{k}_{p(c)}$ is the probe (coupling) field wavevector with magnitude $k_{p(c)} = \nu_{p(c)}/c$ and $\nu_{p(c)}$ is the probe (coupling) field frequency, we could treat the wavevector of the two standing wave the same, i.e., $k_c = \nu_1/c \approx \nu_2/c$, provided that negligible spatial phase difference is accumulated in the region of atomic sample, i.e., $(\nu_1 - \nu_2)L/c \ll \pi$ with L being the length of the cell. It is justified with $\nu_1 - \nu_2 = 2\pi \times 300MHz$ and $L = 6cm$, $(\nu_1 - \nu_2)L/c = 0.12\pi \ll \pi$. $|i_m\rangle$ $(i = a, b, c)$ is the corresponding quantum state of the mth atom at position $\mathbf{r}_m$, $\Omega_p = \mu E_p/\hbar$ and $\Omega_{1(2)} = \mu E_{1(2)}/\hbar$ are the Rabi frequencies of the probe field and the near-resonant (far-detuning) standing wave, respectively, and $\kappa = 2\Omega_2^2/\omega_{ba} - \nu_2$ is the amplitude of a position-dependent Stark shift induced by far-detuning coupling field.

To reveal the lattice structure, we define the collective creation operators

$$\begin{aligned} b_j^\dagger =& \frac{1}{\sqrt{N}} \sum_m e^{i(\mathbf{k}_p + 2j\mathbf{k}_c)\cdot\mathbf{r}_m} |b_m\rangle\langle c_m|, \\ a_j^\dagger =& \frac{1}{\sqrt{N}} \sum_m e^{i[\mathbf{k}_p + (2j-1)\mathbf{k}_c]\cdot\mathbf{r}_m} |b_m\rangle\langle c_m|, \end{aligned} \tag{9.2}$$

which are approximately bosonic ($[b_j, b_{j'}^\dagger] = \delta_{jj'}$ with $\delta_{jj'}$ being the Kronecker delta function) under the EIT condition, $\Omega_1 \gg \Omega_p$ and thus $\mathrm{Tr}(|c_m\rangle\langle c_m|) \approx 1$. Substituting the inverse transformation of Eq. (9.2) to Eq. (9.1), we obtain $H_{\text{eff}} = H + H_p$ with $\delta = 0$ and $\theta = \pi/2$ (we use this phase for simplicity), where

$$H = \sum_j \Omega(a_j^\dagger b_j + a_j^\dagger b_{j-1}) + i\kappa(a_j^\dagger a_{j+1} - b_j^\dagger b_{j+1}) + h.c., \tag{9.3}$$

is a tight-binding Hamiltonian of superradiance lattice and $H_p = \sqrt{N}\Omega_p(b_0^\dagger + b_0)$ is a pumping Hamiltonian at the 0th lattice site of state b, we ignore the suffix of Ω_1. The single excitation states in the superradiance lattice of Eq. (9.3) are the TDSs, for example, $|b_j\rangle \equiv b_j^\dagger|c_1, c_2, ..., c_N\rangle = (1/\sqrt{N})\sum_j e^{i(\mathbf{k}_p + 2j\mathbf{k}_c)\cdot\mathbf{r}_m}|c_1, c_2, ..., b_j, ..., c_N\rangle$ and simi-

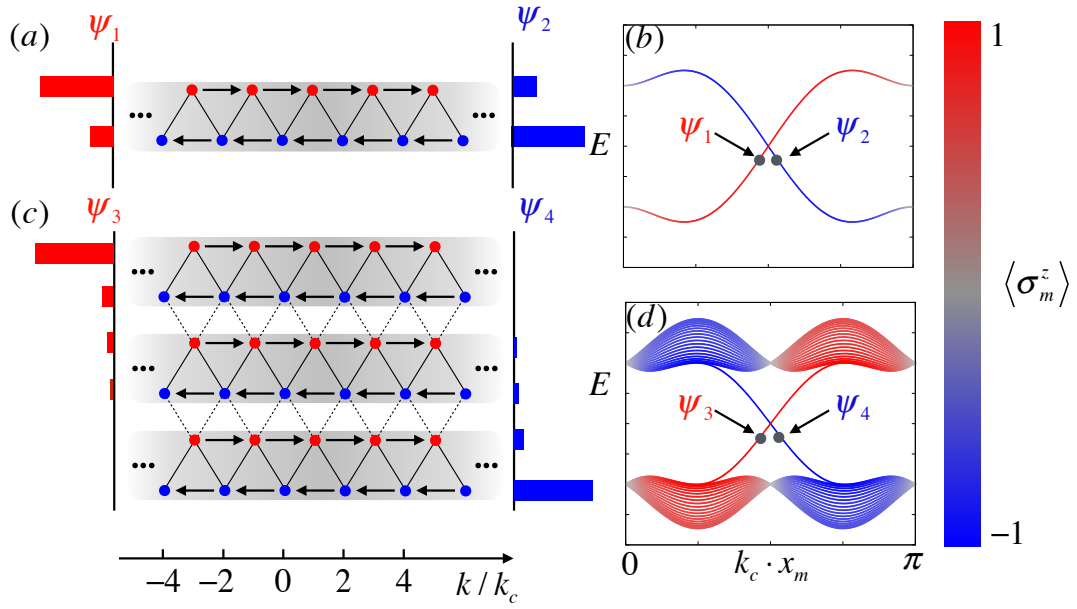

Figure 9.2: The lattice and band structure with effective magnetic field. (a) ribbon lattice, the arrow indicates the complex phase $\pi/2$ carried by the interaction between two sites. Distribution of eigenstates ψ_1 and ψ_2 over two edges is on the side. (b) Dispersion of two edge states. (c) Virtually extend the lattice to multiple layers, keeping the effective magnetic flux uniform over the system. ψ_3 and ψ_4 on the side. (d) Bulk band structure and two edge states.

larly $|a_j\rangle \equiv a_j^\dagger|c_1, c_2, ..., c_N\rangle$.

The lattice structure is shown in Fig. (9.2a). Due to the phase factor $i \equiv \sqrt{-1}$ before κ, each of the unit triangle encloses $1/4$ effective magnetic flux quantum $\Phi_0 = h/2\pi$. Here the sign of i is crucial in determining the direction of the synthetic magnetic field, the effective flux will be reversed when $\theta = -\pi/2$ or eliminated when $\theta = 0, \pi$. A momentum space tight-binding lattice is diagonal in real space. The dispersion relation can be obtained from Eq. (9.1),

$$\Lambda_\pm = \pm 2\sqrt{\kappa^2 \sin^2(2\mathbf{k}_c \cdot \mathbf{r}_m) + \Omega^2 \cos^2(\mathbf{k}_c \cdot \mathbf{r}_m)}, \tag{9.4}$$

and the eigenfunctions $|\psi_+\rangle = \cos(\theta/2)|a_m\rangle + \sin(\theta/2)|b_m\rangle$ and $|\psi_-\rangle = -\sin(\theta/2)|a_m\rangle +$

$\cos(\theta/2)|b_m\rangle$, with $\theta = \arccos[2\kappa \sin(2\mathbf{k}_c \cdot \mathbf{r}_m)/|\Lambda_\pm|]$ for $\mathbf{k}_c \cdot \mathbf{r}_m \neq \pi/2$. At the zero energy point $\mathbf{k}_c \cdot \mathbf{r}_m = \pi/2$, we simply assign $|\psi_+\rangle = |b_m\rangle$ and $|\psi_-\rangle = |a_m\rangle$.

9.3 Band Structure and Edge States

In Fig. (9.2b), we plot the dispersion with the "spin texture" $\langle \sigma_m^z \rangle$, where $\sigma_m^z = |b_m\rangle\langle b_m| - |a_m\rangle\langle a_m|$, indicated by the colors. It is obvious that the two eigenstates concentrate on each of the two edges, ψ_1 and ψ_2, have opposition group velocities. In Fig. (9.2c), we virtually extend the two edges, i.e., from quasi-one dimensional to a two-dimensional triangular lattice, with the same $1/4$ unit magnetic flux per triangle [100]. There are two energy bands with Chern numbers ± 1 connected by two groups of edges states ψ_3 and ψ_4, as shown in Fig. (9.2d). The two groups of edge states are nearly the same in both the eigenenergy and state components as those in Fig. (9.2b). In other word, by reducing the system in Fig. (9.2c) to Fig. (9.2a), edge states are preserved.

Studying the Chern number of the extended two-dimensional triangular lattice in details, we have

$$\begin{aligned} H_{2D} = \sum_{ij} & -i\kappa a_{i,j}^\dagger a_{i,j+1} + i\kappa b_{i,j}^\dagger b_{i,j+1} + \Omega a_{i,j}^\dagger b_{i,j} \\ & - i\Omega a_{i+1,j}^\dagger b_{i,j} + \Omega a_{i,j+1}^\dagger b_{i,j} + i\Omega a_{i+1,j+1}^\dagger b_{i,j} + \text{h.c.} \end{aligned} \tag{9.5}$$

the phase of the interaction is chosen, i.e., $\theta = \pi/2$, therefore a uniform effective magnetic field penetrates the lattice, i.e., each of the triangular encloses $1/4$ unit magnetic flux. The H_{2D} is greatly simplified in real space representation, it can be written as

$$H_{2D} = \sum_m \mathbf{h} \cdot \sigma \tag{9.6}$$

where the effective magnetic field is

$$\begin{aligned} h_x &= 2\sqrt{2}\Omega \cos \mathbf{k}_v \cdot \mathbf{x}_m \cos(\mathbf{k}_c \cdot \mathbf{r}_m + \frac{\pi}{4}) \\ h_y &= 2\sqrt{2}\Omega \sin \mathbf{k}_v \cdot \mathbf{x}_m \sin(\mathbf{k}_c \cdot \mathbf{r}_m + \frac{\pi}{4}) \\ h_z &= -2\kappa \sin 2\mathbf{k}_c \cdot \mathbf{r}_m \end{aligned} \tag{9.7}$$

$\mathbf{k}_v$ is a virtual wavevector perpendicular with $\mathbf{k}_c$ and the pseudo spin $\sigma = (\sigma_m^x, \sigma_m^y, \sigma_m^z)$ with the Pauli matrices for the mth atom defined as $\sigma_x = a_m^\dagger b_m + b_m^\dagger a_m$, $\sigma_y = -ia_m^\dagger b_m + ib_m^\dagger a_m$ and $\sigma_z = a_m^\dagger a_m - b_m^\dagger b_m$. The Chern number is defined as the total Berry curvature in the whole first Brillouin zone, i.e., $|\mathbf{k}_c \cdot \mathbf{x}_m|, |\mathbf{k}_v \cdot \mathbf{x}_m| \leq \pi/2$, the Chern number of top band is

$$C = -\frac{1}{4\pi} \iint d^2\mathbf{x} \frac{1}{h^3} \epsilon_{abc} h_a \frac{\partial h_b}{\partial x} \frac{\partial h_c}{\partial y} = 1 \tag{9.8}$$

where ϵ_{abc} is the Levi-Civita symbol.

The chiral edge transportation is revealed by the dynamics of the superradiance lattice. In the single excitation limit of a weak probe field, the wavefunction is $|\Psi\rangle \approx |c_1, c_2, ..., c_N\rangle + \sum_j \beta_{aj}|a_j\rangle + \beta_{bj}|b_j\rangle$ where $|\beta_{a(b)j}|^2 \ll 1$. For the sake of simplicity, we assume both states $|b\rangle$ and $|a\rangle$ have the same decay rate γ. The Hamiltonian H_p pumps probability to the 0th lattice site. The excitation then propagates in the lattice with a universal decay rate γ. Finally the probability distribution reaches to a steady state for time $t \gg 1/\gamma$. This process is simulated in Fig. (9.3). The excitation on b sublattice travels to the right and the subsequently created the left-traveling excitation on a sublattice via coupling Ω. In the steady state when the pumping is balanced with the transportation and decay, the distribution of the excitation is concentrated on the right side of the pumping point. This result is consistent with the dispersion relation of the edge states as shown in Fig. (9.2b).

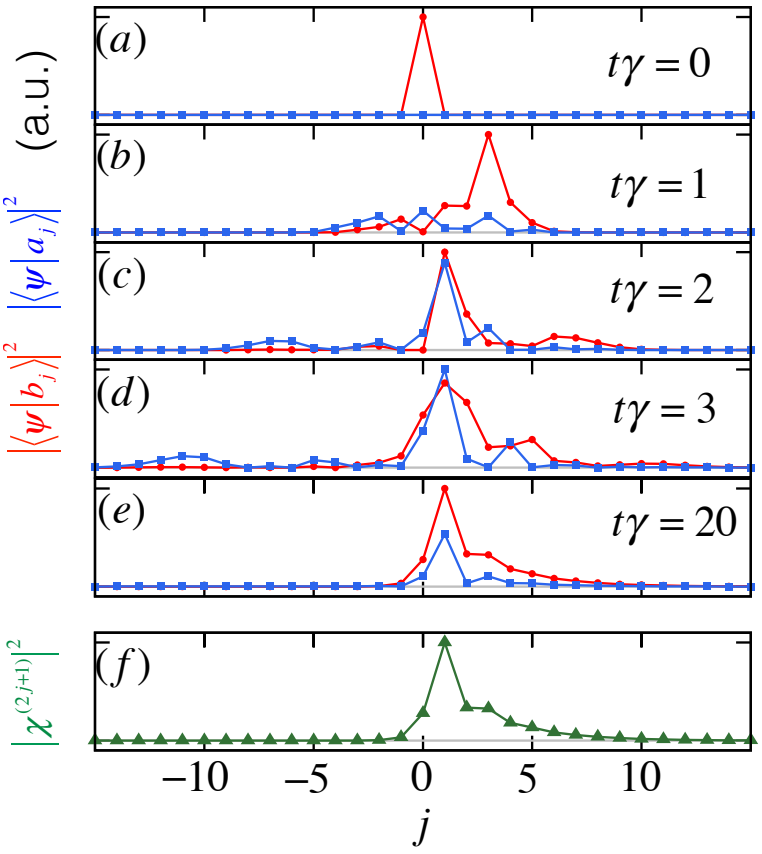

Figure 9.3: The lattice dynamics. (a-e) Plots show that the excitation on $b(a)$ travels to left(right), consistent with the dispersion relation. (f) The values of $|\chi_j|^2$.

9.4 Optical Observable

The next question is how to test this chirality in experiment. To answer this, we first show how the above probability distribution is related to observable optical signals. From Eq. (3.3, 3.4) and Eq. (9.3), we can calculate the susceptibility of the probe field [3],

$$\begin{aligned}\chi(x) &= \frac{3\pi\mathcal{N}\Gamma_{bc}}{\delta - 2\kappa\sin(2k_c x) + i\gamma_{bc} + \frac{\Omega^2\cos^2(k_c x)}{-\Delta_{2ph}+i\gamma_{ac}-2\kappa\sin(2k_c x)}} \\ &= \sum_j \chi_j e^{-2ijk_c x}.\end{aligned} \tag{9.9}$$

Here $\mathcal{N} = n_a\left(\lambda_{bc}/2\pi\right)^3$ with n_a the atomic density, λ_{bc} the transition wavelength and Γ_{bc} the radiative decay rate between $|b\rangle$ and $|c\rangle$. $\delta = \Delta_p + 2\kappa$, $\Delta_c = \omega_{ba} - \nu_1$, $\Delta_p = \omega_{bc} - \nu_p$ and $\Delta_{2ph} = \Delta_p - \Delta_c - 2\kappa$ with ω_{ij} and γ_{ij} being the transition frequency and dephasing rate between $|i\rangle$ and $|j\rangle$. χ_j is the Fourier component of $\chi(x)$ with phase $e^{-2jik_c x}$. The connection between the helical edge states and the EIT susceptibility is demonstrated by comparing Fig. (9.3e) with (f). The values of $|\chi_j|^2$ is linearly proportional with the steady state probabilities of $|b_j\rangle$. The coupling field detuning Δ_c is the energy offset between a and b lattices and δ, including probe field detuning Δ_p and spatial-independent Stark shift 2κ, can be used to control the energy of the excitation [103].

A probe field with wavevector $\mathbf{k}_{p+}$ (here approximately along the x-axis) can excite the timed Dicke state $|b_0\rangle$, which have directional emissions along $\mathbf{k}_{p+}$ [7]. If the phase-matching condition is satisfied for $\mathbf{k}_{p-} = \mathbf{k}_{p+} - 2\mathbf{k}_c$ with $|\mathbf{k}_{p-}| \approx |\mathbf{k}_{p+}|$, the corresponding timed Dicke state $|b_{-1}\rangle$ can also have directional emission (approximately along the $-x$ axis), as shown in Fig. (9.1). Other timed Dicke states in the superradiance lattice cannot satisfy the momentum conservation when coupled to the vacuum modes and thus have no directional emissions[7]. This is usually understood as the phase-matching condition of the traditional nonlinear optics, where χ_j is the $(2|j|+1)'$th order nonlinear coefficient of

the $(2|j|+2)$-wave-mixing. The distribution of χ_j can, therefore, be tested by the wave-mixing signals. For example, the light signal due to $\chi_{\pm 1}$ is governed by the coupled-wave equations [70],

$$\begin{aligned} 2\frac{\partial E_p}{\partial k_p x} &= i\chi_0 E_p + i\chi_{-1} e^{-i\Delta k x} E_f, \\ 2\frac{\partial E_f}{\partial k_p x} &= -i\chi_0 E_f - i\chi_1 e^{i\Delta k x} E_p, \end{aligned} \tag{9.10}$$

where $E_{p\pm}$ is the slowly-varying field amplitude of modes $\mathbf{k}_{p\pm}$ and $\Delta k = 2(\mathbf{k}_p - \mathbf{k}_c)\cdot\hat{x}$ is the wavevector mismatch.

We can see the asymmetry in Eq. (9.10) by noticing that $|\chi_1| \gg |\chi_{-1}|$ (as shown in Fig. (9.3). The conversion rate from E_p to E_f is much smaller than the one $|\chi_{-1}| \gg |\chi_1|$. Consequently, the reflectivity of the probe field R_+ if we lock the spatial phase difference $\theta/2 = \pi/4$, is much smaller than the one, R_-, of $\theta/2 = -\pi/4$, as shown in Fig. (9.4a). The reflectance $R_\pm$ for the probe field E_p is drawn as a function of the probe detuning, as well as R_0 of $\theta/2 = 0$, i.e., $|\chi_{-1}| = |\chi_1|$, for comparison. Different probe detunings probe different energy at $\Lambda_\pm = -\delta$ of the $|b\rangle$ edge states, which mostly have positive (negative) dispersion and thus $|\chi_1| > (<)|\chi_{-1}|$ for $\theta = \pm\pi/2$. We see that $R_+ < R_-$ for most of the probe detuning except near the band edge, where the dispersion of the edge states goes in the other way, as shown in Fig. (9.2d).

We next analyse the effect of the Doppler shift due to the motion of the atoms. The atomic velocity component v_x along x-axis introduces a detuning $\delta = 2v_x\nu_c/c$ between the two coupling fields. This detuning introduces an effective force in the superradiance lattice [49]. Intuitively, the position of the atom with respect to the standing wave is $r = v_x t$, i.e., changes linearly with time, which is analogous to the linear evolution of the crystalline momentum of an electron subjected to an electric field in real space crystals. In Fig. (9.4b), we plotted the reflection spectra with different detunings. It is obvious that the bias between the reflectivity $R_\pm$ is robust to this Doppler shift.

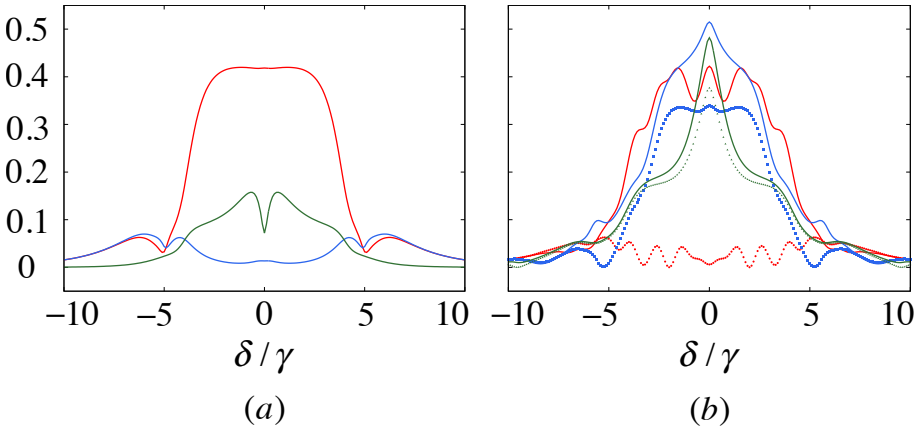

Figure 9.4: (a) The reflection spectrum for atoms without motion. Tuning the spatial phase difference, $\theta = \pi/2$, R_+(blue); $\theta = -\pi/2$, R_- (red); $\theta = 0$, R_0 (green). (b) The reflection spectrum for atoms with certain velocity. Dashed (Solid) line means $\theta = (-)\pi/4$. Atoms have Doppler shift γ (red), 3γ (blue) and 5γ (green).

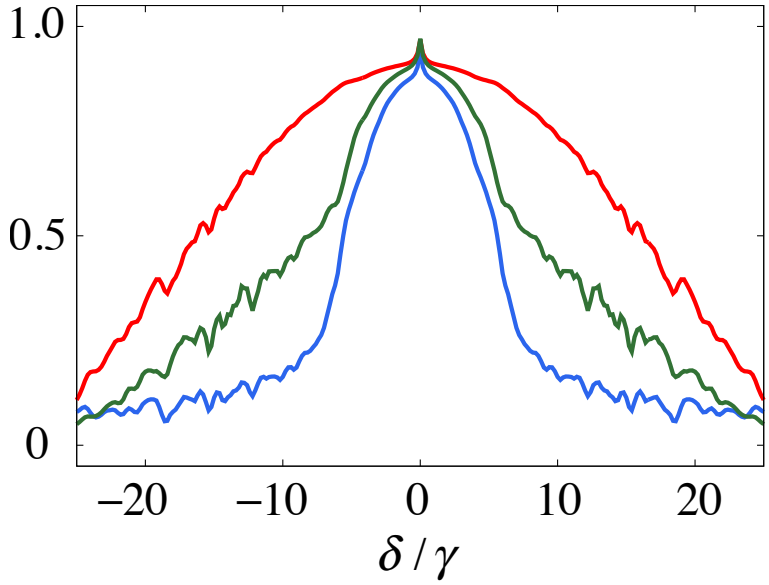

Figure 9.5: The reflection spectra in Rb vapor cells in room temperature. The Rabi frequency of the coupling fields is $2\pi \times 50MHz$ with cell length $L = 5cm$, the atomic density $N = 3.5 \times 10^{10} cm^{-3}$. See more details in the text.

To investigate the feasibility of experimental detection, we simulate the reflection spectra in Fig. (9.5) with Cs vapour cell at the room temperature. The three levels involved are $|a\rangle = |6^2S_{1/2}, F = 4\rangle$, $|b\rangle = |6^2P_{1/2}, F = 3\rangle$ and $|c\rangle = |6^2S_{1/2}, F = 3\rangle$. The results show that $R_+ > R_-$ for any probe detuning, particularly for nonzero probe detuning. Although the FWHM of the Doppler broadening of the atoms is 360MHz while the Rabi frequency of each components in the coupling field is around 20MHz, the asymmetry is very robust against the thermal fluctuation. The reason is similar with the optical diode in hot vapor[104] and electrons transportation in a metal. For electrons, suffering from large random diffusion, they have a small uni-directional drift velocity induced by the applied electric field. The non-reciprocity in optical diode comes from the unidirectional velocity of the detuned standing wave modulation in a medium gas with large but symmetrically distributed thermal velocities. Similarly, asymmetry in the reflection spectrum from both directions survives in the large doppler broadening.

10. CONCLUSION

The primary conclusion of the present dissertation is that (a). cooperative effect plays an active role in fundamental research and novel application of quantum optics; (b) superradiance lattice offers a new platform in quantum optics to test topological non-trivial effect. The main results are summarized as follows.as follows.

(1) The symmetry of the atomic distribution is cruial in mitigation of the collective Lamh shift, which is vital in the preparetion of a single-photon subradiant state.

(2) A theory and an experiment in BEC is performed to demenstate the superradiance lattice, which is the bridge connecting quantum optics and novel topological effect.

(3) A theory predicts a topological phase transition in 2D superradiance lattice, realizing the Haldane model in quantum optics.

(4) A novel system is proposed to prepare mesoscopic superposition states of photons, consisting of three frequency-modulated cavities and one two-level atom. The physics can be understood in a finite spin-orbit-coupled Fock-state lattice.

(5) An experiment is proposed to observe synthetic magnetic field in thermal vapor of alkali atoms.

REFERENCES

[1] S. E. Harris, "Lasers without inversion: Interference of lifetime-broadened resonances," *Physical Review Letters*, vol. 62, no. 9, p. 1033, 1989.

[2] K.-J. Boller, A. Imamoğlu, and S. E. Harris, "Observation of electromagnetically induced transparency," *Physical Review Letters*, vol. 66, no. 20, p. 2593, 1991.

[3] M. Fleischhauer, A. Imamoglu, and J. P. Marangos, "Electromagnetically induced transparency: Optics in coherent media," *Reviews of modern physics*, vol. 77, no. 2, p. 633, 2005.

[4] O. Kocharovskaya and Y. I. Khanin, "Coherent amplification of an ultrashort pulse in a three-level medium without a population inversion," *Soviet Journal of Experimental and Theoretical Physics Letters*, vol. 48, p. 630, 1988.

[5] M. O. Scully, S.-Y. Zhu, and A. Gavrielides, "Degenerate quantum-beat laser: Lasing without inversion and inversion without lasing," *Physical review letters*, vol. 62, no. 24, p. 2813, 1989.

[6] L. V. Hau, S. E. Harris, Z. Dutton, and C. H. Behroozi, "Light speed reduction to 17 metres per second in an ultracold atomic gas," *Nature*, vol. 397, no. 6720, p. 594, 1999.

[7] M. O. Scully, E. S. Fry, C. H. R. Ooi, and K. Wódkiewicz, "Directed spontaneous emission from an extended ensemble of n atoms: Timing is everything," *Phys. Rev. Lett.*, vol. 96, no. 1, p. 010501, 2006.

[8] M. O. Scully, "Single photon subradiance: Quantum control of spontaneous emission and ultrafast readout," *Phys. Rev. Lett.*, vol. 115, p. 243602, Dec 2015.

[9] M. O. Scully, "Collective lamb shift in single photon dicke superradiance," *Phys. Rev. Lett.*, vol. 102, no. 14, p. 143601, 2009.

[10] R. Röhlsberger, K. Schlage, B. Sahoo, S. Couet, and R. RÃijffer, "Collective lamb shift in single-photon superradiance," *Science*, vol. 328, no. 5983, pp. 1248–1251, 2010.

[11] R. Röhlsberger, "Cooperative emission from nuclei: The collective lamb shift and electromagnetically induced transparency," *Fortschritte der Physik*, vol. 61, no. 2-3, pp. 360–376, 2013.

[12] M. O. Scully, K. R. Chapin, K. E. Dorfman, M. B. Kim, and A. Svidzinsky, "Quantum heat engine power can be increased by noise-induced coherence," *Proceedings of the National Academy of Sciences*, vol. 108, no. 37, pp. 15097–15100, 2011.

[13] M. O. Scully, "Quantum photocell: Using quantum coherence to reduce radiative recombination and increase efficiency," *Physical review letters*, vol. 104, no. 20, p. 207701, 2010.

[14] R. Dicke, "Coherence in spontaneous radiation processes," *Phys. Rev.*, vol. 93, no. 1, p. 99110, 1954.

[15] A. Gero and E. Akkermans, "Effect of superradiance on transport of diffusing photons in cold atomic gases," *Physical review letters*, vol. 96, no. 9, p. 093601, 2006.

[16] E. Akkermans, A. Gero, and R. Kaiser, "Photon localization and dicke superradiance in atomic gases," *Phys. Rev. Lett.*, vol. 101, no. 10, p. 103602, 2008.

[17] A. A. Svidzinsky, J.-T. Chang, and M. O. Scully, "Dynamical evolution of correlated spontaneous emission of a single photon from a uniformly excited cloud of n atoms," *Physical review letters*, vol. 100, no. 16, p. 160504, 2008.

[18] A. Svidzinsky and J.-T. Chang, "Cooperative spontaneous emission as a many-body eigenvalue problem," *Phys. Rev. A*, vol. 77, no. 4, p. 043833, 2008.

[19] A. A. Svidzinsky, J.-T. Chang, and M. O. Scully, "Cooperative spontaneous emission of n atoms: Many-body eigenstates, the effect of virtual lamb shift processes, and analogy with radiation of n classical oscillators," *Phys. Rev. A*, vol. 81, no. 5, p. 053821, 2010.

[20] B. Zhu, J. Cooper, J. Ye, and A. M. Rey, "Light scattering from dense cold atomic media," *Phys. Rev. A*, vol. 94, aug 2016.

[21] P. Longo, C. H. Keitel, and J. Evers, "Tailoring superradiance to design artificial quantum systems," *Scientific reports*, vol. 6, 2016.

[22] J. Keaveney, A. Sargsyan, U. Krohn, I. G. Hughes, D. Sarkisyan, and C. S. Adams, "Cooperative lamb shift in an atomic vapor layer of nanometer thickness," *Physical review letters*, vol. 108, no. 17, p. 173601, 2012.

[23] T. Bienaimé, N. Piovella, and R. Kaiser, "Controlled dicke subradiance from a large cloud of two-level systems," *Physical review letters*, vol. 108, no. 12, p. 123602, 2012.

[24] R. Puthumpally-Joseph, M. Sukharev, O. Atabek, and E. Charron, "Dipole-induced electromagnetic transparency," *Physical review letters*, vol. 113, no. 16, p. 163603, 2014.

[25] S. L. Bromley, B. Zhu, M. Bishof, X. Zhang, T. Bothwell, J. Schachenmayer, T. L. Nicholson, R. Kaiser, S. F. Yelin, M. D. Lukin, A. M. Rey, and J. Ye, "Collective atomic scattering and motional effects in a dense coherent medium," *Nature Communications*, vol. 7, p. 11039, mar 2016.

[26] F. D. M. Haldane, "Model for a quantum hall effect without landau levels: Condensed-matter realization of the" parity anomaly"," *Physical Review Letters*, vol. 61, no. 18, p. 2015, 1988.

[27] C. L. Kane and E. J. Mele, "Quantum spin hall effect in graphene," *Physical review letters*, vol. 95, no. 22, p. 226801, 2005.

[28] B. A. Bernevig and S.-C. Zhang, "Quantum spin hall effect," *Physical Review Letters*, vol. 96, no. 10, p. 106802, 2006.

[29] M. König, S. Wiedmann, C. Brüne, A. Roth, H. Buhmann, L. W. Molenkamp, X.-L. Qi, and S.-C. Zhang, "Quantum spin hall insulator state in hgte quantum wells," *Science*, vol. 318, no. 5851, pp. 766–770, 2007.

[30] X.-L. Qi, T. L. Hughes, S. Raghu, and S.-C. Zhang, "Time-reversal-invariant topological superconductors and superfluids in two and three dimensions," *Physical review letters*, vol. 102, no. 18, p. 187001, 2009.

[31] C.-Z. Chang, J. Zhang, X. Feng, J. Shen, Z. Zhang, M. Guo, K. Li, Y. Ou, P. Wei, L.-L. Wang, *et al.*, "Experimental observation of the quantum anomalous hall effect in a magnetic topological insulator," *Science*, vol. 340, no. 6129, pp. 167–170, 2013.

[32] F. Haldane and S. Raghu, "Possible realization of directional optical waveguides in photonic crystals with broken time-reversal symmetry," *Physical review letters*, vol. 100, no. 1, p. 013904, 2008.

[33] M. Hafezi, S. Mittal, J. Fan, A. Migdall, and J. Taylor, "Imaging topological edge states in silicon photonics," *Nature Photonics*, vol. 7, no. 12, pp. 1001–1005, 2013.

[34] M. C. Rechtsman, J. M. Zeuner, Y. Plotnik, Y. Lumer, D. Podolsky, F. Dreisow, S. Nolte, M. Segev, and A. Szameit, "Photonic floquet topological insulators," *Nature*, vol. 496, no. 7444, pp. 196–200, 2013.

[35] A. B. Khanikaev, S. H. Mousavi, W.-K. Tse, M. Kargarian, A. H. MacDonald, and G. Shvets, "Photonic analogue of two-dimensional topological insulators and helical one-way edge transport in bi-anisotropic metamaterials," *arXiv preprint arXiv:1204.5700*, 2012.

[36] A. Nalitov, G. Malpuech, H. Terças, and D. Solnyshkov, "Spin-orbit coupling and the optical spin hall effect in photonic graphene," *Physical review letters*, vol. 114, no. 2, p. 026803, 2015.

[37] T. Oka and H. Aoki, "Photovoltaic hall effect in graphene," *Physical Review B*, vol. 79, no. 8, p. 081406, 2009.

[38] J.-i. Inoue and A. Tanaka, "Photoinduced transition between conventional and topological insulators in two-dimensional electronic systems," *Physical review letters*, vol. 105, no. 1, p. 017401, 2010.

[39] T. Kitagawa, E. Berg, M. Rudner, and E. Demler, "Topological characterization of periodically driven quantum systems," *Physical Review B*, vol. 82, no. 23, p. 235114, 2010.

[40] N. H. Lindner, D. L. Bergman, G. Refael, and V. Galitski, "Topological floquet spectrum in three dimensions via a two-photon resonance," *Physical Review B*, vol. 87, no. 23, p. 235131, 2013.

[41] G. Jotzu, M. Messer, R. Desbuquois, M. Lebrat, T. Uehlinger, D. Greif, and T. Esslinger, "Experimental realisation of the topological haldane model," *Nature*, vol. 515, pp. 237–240, 2014.

[42] H. Cai, D.-W. Wang, A. A. Svidzinsky, S.-Y. Zhu, and M. O. Scully, "Symmetry-protected single-photon subradiance," *Physical Review A*, vol. 93, no. 5, p. 053804, 2016.

[43] W. E. Lamb Jr and R. C. Retherford, "Fine structure of the hydrogen atom by a microwave method," *Phys. Rev.*, vol. 72, no. 3, p. 241, 1947.

[44] A. Crubellier, S. Liberman, and P. Pillet, "Superradiance and subradiance in three-level systems," *Opt. Comm.*, vol. 33, no. 2, pp. 143–148, 1980.

[45] C. H. van der Wal, M. D. Eisaman, A. André, R. L. Walsworth, D. F. Phillips, A. S. Zibrov, and M. D. Lukin, "Atomic memory for correlated photon states," *Science (New York, N.Y.)*, vol. 301, no. 5630, pp. 196–200, 2003.

[46] A. T. Black, J. K. Thompson, and V. Vuletić, "On-demand superradiant conversion of atomic spin gratings into single photons with high efficiency," *Phys. Rev. Lett.*, vol. 95, no. 13, p. 133601, 2005.

[47] A. Kuzmich, W. P. Bowen, A. D. Boozer, A. Boca, C. W. Chou, L. M. Duan, and H. J. Kimble, "Generation of nonclassical photon pairs for scalable quantum communication with atomic ensembles," *Nature*, vol. 423, no. 6941, pp. 731–734, 2003.

[48] V. Balic, D. A. Braje, P. Kolchin, G. Y. Yin, and S. E. Harris, "Generation of paired photons with controllable waveforms," *Phys. Rev. Lett.*, vol. 94, no. 18, p. 183601, 2005.

[49] D.-W. Wang, R.-B. Liu, S.-Y. Zhu, and M. O. Scully, "Superradiance lattice," *Phys. Rev. Lett.*, vol. 114, no. 4, p. 043602, 2015.

[50] A. A. Svidzinsky, X. Zhang, and M. O. Scully, "Quantum versus semiclassical description of light interaction with atomic ensembles: Revision of the maxwell-bloch equations and single-photon superradiance," *Phys. Rev. A*, vol. 92, no. 1, p. 013801, 2015.

[51] W. Feng, Y. Li, and S.-Y. Zhu, "Effect of atomic distribution on cooperative spontaneous emission," *Phys. Rev. A*, vol. 89, no. 1, p. 013816, 2014.

[52] M. O. Scully and M. S. Zubairy, "Quantum optics," 1999.

[53] J. R. Ackerhalt, P. L. Knight, and J. H. Eberly, "Radiation reaction and radiative frequency shifts," *Physical Review Letters*, vol. 30, no. 10, p. 456, 1973.

[54] G. S. Agarwal, *Quantum statistical theories of spontaneous emission and their relation to other approaches*. Springer, 1974.

[55] T. Bienaimé, R. Bachelard, N. Piovella, and R. Kaiser, "Cooperativity in light scattering by cold atoms," *Fortschritte der Physik*, vol. 61, no. 2-3, pp. 377–392, 2013.

[56] R. Friedberg, S. R. Hartmann, and J. T. Manassah, "Frequency shifts in emission and absorption by resonant systems ot two-level atoms," *Phys. Rep.*, vol. 7, no. 3, pp. 101–179, 1973.

[57] M. O. Scully and A. A. Svidzinsky, "The lamb shiftâĂŤyesterday, today, and tomorrow," *Science*, vol. 328, no. 5983, pp. 1239–1241, 2010.

[58] M. Gross and S. Haroche, "Superradiance: An essay on the theory of collective spontaneous emission," *Phys. Rep.*, vol. 93, no. 5, pp. 301–396, 1982.

[59] J. J. Sakurai and J. J. Napolitano, *Modern quantum mechanics*. Pearson Higher Ed, 2014.

[60] G. Heinze, C. Hubrich, and T. Halfmann, "Stopped light and image storage by electromagnetically induced transparency up to the regime of one minute," *Physical review letters*, vol. 111, no. 3, p. 033601, 2013.

[61] W. E. Lamb Jr, "Capture of neutrons by atoms in a crystal," *Physical Review*, vol. 55, no. 2, p. 190, 1939.

[62] R. L. Mössbauer, "Kernresonanzfluoreszenz von gammastrahlung in ir191," *Zeitschrift für Physik*, vol. 151, no. 2, pp. 124–143, 1958.

[63] H. M. Price, T. Ozawa, and I. Carusotto, "Quantum mechanics with a momentum-space artificial magnetic field," *Physical Review Letters*, vol. 113, nov 2014.

[64] P. Wang, Z.-Q. Yu, Z. Fu, J. Miao, L. Huang, S. Chai, H. Zhai, and J. Zhang, "Spin-orbit coupled degenerate fermi gases," *Phys. Rev. Lett.*, vol. 109, aug 2012.

[65] L. W. Cheuk, A. T. Sommer, Z. Hadzibabic, T. Yefsah, W. S. Bakr, and M. W. Zwierlein, "Spin-injection spectroscopy of a spin-orbit coupled fermi gas," *Phys. Rev. Lett.*, vol. 109, aug 2012.

[66] M. B. Dahan, E. Peik, J. Reichel, Y. Castin, and C. Salomon, "Bloch oscillations of atoms in an optical potential," *Physical Review Letters*, vol. 76, no. 24, p. 4508, 1996.

[67] A. Polkovnikov, S. Sachdev, and S. M. Girvin, "Nonequilibrium gross-pitaevskii dynamics of boson lattice models," *Phys. Rev. A*, vol. 66, nov 2002.

[68] C. Hooley and J. Quintanilla, "Single-atom density of states of an optical lattice," *Phys. Rev. Lett.*, vol. 93, aug 2004.

[69] S. Ryu and Y. Hatsugai, "Topological origin of zero-energy edge states in particle-hole symmetric systems," *Physical review letters*, vol. 89, no. 7, p. 077002, 2002.

[70] D.-W. Wang, H. Cai, L. Yuan, S.-Y. Zhu, and R.-B. Liu, "Topological phase transitions in superradiance lattices," *Optica*, vol. 2, no. 8, p. 712, 2015.

[71] A. Gómez-León and G. Platero, "Floquet-bloch theory and topology in periodically driven lattices," *Physical review letters*, vol. 110, no. 20, p. 200403, 2013.

[72] Y. Lumer, Y. Plotnik, M. C. Rechtsman, and M. Segev, "Self-localized states in photonic topological insulators," *Physical review letters*, vol. 111, no. 24, p. 243905, 2013.

[73] D.-W. Wang, H. Cai, R.-B. Liu, and M. O. Scully, "Mesoscopic superposition states generated by synthetic spin-orbit interaction in fock-state lattices," *Phys. Rev. Lett.*, vol. 116, jun 2016.

[74] H. Wang, M. Mariantoni, R. C. Bialczak, M. Lenander, E. Lucero, M. Neeley, A. O'Connell, D. Sank, M. Weides, J. Wenner, *et al.*, "Deterministic entanglement of photons in two superconducting microwave resonators," *Physical review letters*, vol. 106, no. 6, p. 060401, 2011.

[75] P. Sekatski, N. Sangouard, M. Stobińska, F. Bussieres, M. Afzelius, and N. Gisin, "Proposal for exploring macroscopic entanglement with a single photon and coherent states," *Physical Review A*, vol. 86, no. 6, p. 060301, 2012.

[76] R. Ghobadi, A. Lvovsky, and C. Simon, "Creating and detecting micro-macro photon-number entanglement by amplifying and deamplifying a single-photon entangled state," *Physical review letters*, vol. 110, no. 17, p. 170406, 2013.

[77] B. C. Sanders, "Entangled coherent states," *Physical Review A*, vol. 45, no. 9, p. 6811, 1992.

[78] J. Koch, A. A. Houck, K. Le Hur, and S. Girvin, "Time-reversal-symmetry breaking in circuit-qed-based photon lattices," *Physical Review A*, vol. 82, no. 4, p. 043811, 2010.

[79] K. Sliwa, M. Hatridge, A. Narla, S. Shankar, L. Frunzio, R. Schoelkopf, and M. Devoret, "Reconfigurable josephson circulator/directional amplifier," *Physical Review X*, vol. 5, no. 4, p. 041020, 2015.

[80] N. A. Estep, D. L. Sounas, J. Soric, and A. Alù, "Magnetic-free non-reciprocity and isolation based on parametrically modulated coupled-resonator loops," *Nature Physics*, vol. 10, no. 12, p. 923, 2014.

[81] C. Guerlin, J. Bernu, S. Deleglise, C. Sayrin, S. Gleyzes, S. Kuhr, M. Brune, J.-M. Raimond, and S. Haroche, "Progressive field-state collapse and quantum non-demolition photon counting," *arXiv preprint arXiv:0707.3880*, 2007.

[82] C. Sayrin, I. Dotsenko, X. Zhou, B. Peaudecerf, T. Rybarczyk, S. Gleyzes, P. Rouchon, M. Mirrahimi, H. Amini, M. Brune, *et al.*, "Real-time quantum feedback prepares and stabilizes photon number states," *arXiv preprint arXiv:1107.4027*, 2011.

[83] M. Hofheinz, E. Weig, M. Ansmann, R. C. Bialczak, E. Lucero, M. Neeley, A. O'connell, H. Wang, J. M. Martinis, and A. Cleland, "Generation of fock states in a superconducting quantum circuit," *Nature*, vol. 454, no. 7202, p. 310, 2008.

[84] J. Krause, M. O. Scully, and H. Walther, "State reduction and $|n$-state preparation in a high-q micromaser," *Phys. Rev. A*, vol. 36, pp. 4547–4550, Nov 1987.

[85] P. Bertet, S. Osnaghi, P. Milman, A. Auffeves, P. Maioli, M. Brune, J.-M. Raimond, and S. Haroche, "Generating and probing a two-photon fock state with a single atom in a cavity," *Physical Review Letters*, vol. 88, no. 14, p. 143601, 2002.

[86] C. Rigetti, J. M. Gambetta, S. Poletto, B. Plourde, J. M. Chow, A. Córcoles, J. A. Smolin, S. T. Merkel, J. Rozen, G. A. Keefe, *et al.*, "Superconducting qubit in a waveguide cavity with a coherence time approaching 0.1 ms," *Physical Review B*, vol. 86, no. 10, p. 100506, 2012.

[87] E. Jeffrey, D. Sank, J. Mutus, T. White, J. Kelly, R. Barends, Y. Chen, Z. Chen, B. Chiaro, A. Dunsworth, *et al.*, "Fast accurate state measurement with superconducting qubits," *Physical review letters*, vol. 112, no. 19, p. 190504, 2014.

[88] T. Niemczyk, F. Deppe, H. Huebl, E. Menzel, F. Hocke, M. Schwarz, J. Garcia-Ripoll, D. Zueco, T. Hümmer, E. Solano, *et al.*, "Circuit quantum electrodynamics in the ultrastrong-coupling regime," *Nature Physics*, vol. 6, no. 10, p. 772, 2010.

[89] P. Forn-Díaz, J. Lisenfeld, D. Marcos, J. J. García-Ripoll, E. Solano, C. Harmans, and J. Mooij, "Observation of the bloch-siegert shift in a qubit-oscillator system in the ultrastrong coupling regime," *Physical review letters*, vol. 105, no. 23, p. 237001, 2010.

[90] M. Reagor, W. Pfaff, C. Axline, R. Heeres, N. Ofek, K. Sliwa, E. Holland, C. Wang, J. Blumoff, K. Chou, *et al.*, "A quantum memory with near-millisecond coherence in circuit qed, 2015," *arXiv preprint arXiv:1508.05882*.

[91] M. R. Vissers, J. Hubmayr, M. Sandberg, S. Chaudhuri, C. Bockstiegel, and J. Gao, "Frequency-tunable superconducting resonators via nonlinear kinetic inductance," *Applied Physics Letters*, vol. 107, no. 6, p. 062601, 2015.

[92] J. R. Johansson, G. Johansson, C. M. Wilson, and F. Nori, "Dynamical casimir effect in a superconducting coplanar waveguide," *Phys. Rev. Lett.*, vol. 103, p. 147003, Sep 2009.

[93] C. Wilson, G. Johansson, A. Pourkabirian, M. Simoen, J. Johansson, T. Duty, F. Nori, and P. Delsing, "Observation of the dynamical casimir effect in a superconducting circuit," *Nature*, vol. 479, pp. 376–379, 2011.

[94] K. v. Klitzing, G. Dorda, and M. Pepper, "New method for high-accuracy determination of the fine-structure constant based on quantized hall resistance," *Physical Review Letters*, vol. 45, no. 6, pp. 494–497, 1980.

[95] Y. J. Lin, R. L. Compton, K. Jimenez-Garcia, J. V. Porto, and I. B. Spielman, "Synthetic magnetic fields for ultracold neutral atoms," *Nature*, vol. 462, no. 7273, pp. 628–632, 2009.

[96] J. Dalibard, F. Gerbier, G. Juzeliunas, and P. Öhberg, "Colloquium: Artificial gauge potentials for neutral atoms," *Reviews of Modern Physics*, vol. 83, no. 4, pp. 1523–

1543, 2011.

[97] M. Mancini, G. Pagano, G. Cappellini, L. Livi, M. Rider, J. Catani, C. Sias, P. Zoller, M. Inguscio, M. Dalmonte, *et al.*, "Observation of chiral edge states with neutral fermions in synthetic hall ribbons," *Science*, vol. 349, no. 6255, pp. 1510–1513, 2015.

[98] M. Atala, M. Aidelsburger, M. Lohse, J. T. Barreiro, B. Paredes, and I. Bloch, "Observation of chiral currents with ultracold atoms in bosonic ladders," *Nat Phys*, vol. 10, no. 8, pp. 588–593, 2014.

[99] B. Stuhl, H.-I. Lu, L. Aycock, D. Genkina, and I. Spielman, "Visualizing edge states with an atomic bose gas in the quantum hall regime," *Science*, vol. 349, no. 6255, pp. 1514–1518, 2015.

[100] D. Hügel and B. Paredes, "Chiral ladders and the edges of quantum hall insulators," *Phys. Rev. A*, vol. 89, no. 2, p. 023619, 2014.

[101] E. Anisimovas, M. Račiūnas, C. Sträter, A. Eckardt, I. Spielman, and G. Juzeliūnas, "Semisynthetic zigzag optical lattice for ultracold bosons," *Physical Review A*, vol. 94, no. 6, p. 063632, 2016.

[102] A. Celi, P. Massignan, J. Ruseckas, N. Goldman, I. Spielman, G. Juzeliūnas, and M. Lewenstein, "Synthetic gauge fields in synthetic dimensions," *Phys. Rev. Lett.*, vol. 112, no. 4, p. 043001, 2014.

[103] D.-W. Wang, S.-Y. Zhu, J. Evers, and M. O. Scully, "High-frequency light reflector via low-frequency light control," *Phys. Rev. A*, vol. 91, no. 1, p. 011801, 2015.

[104] D.-W. Wang, H.-T. Zhou, M.-J. Guo, J.-X. Zhang, J. Evers, and S.-Y. Zhu, "Optical diode made from a moving photonic crystal," *Phys. Rev. Lett.*, vol. 110, no. 9, p. 093901, 2013.

APPENDIX A

FURTHER SIMPLIFICATION OF THE KUBO FORMULA

Eq. (6.24) is rewritten

$$\sigma_2 = \sum_{\mathbf{k}\mathbf{k}'} \frac{\hbar e^2}{i}[f_0(\mathbf{k}') - f_0(\mathbf{k})]\frac{\langle \mathbf{k}|v_x|\mathbf{k}'\rangle\langle \mathbf{k}'|v_y|\mathbf{k}\rangle}{[E(\mathbf{k}') - E(\mathbf{k})]^2}. \tag{A.1}$$

In the limit of zero temperature $T \to 0$, the difference of Fermi-Dirac distribution $f_0(\mathbf{k}') - f_0(\mathbf{k})$ will be equal to

$$\begin{aligned} &1, \text{ if } E(\mathbf{k}') < E_F < E(\mathbf{k}) \\ &-1, \text{ if, } E(\mathbf{k}') > E_F > E(\mathbf{k}) \\ &0, \text{ otherwise} \end{aligned} \tag{A.2}$$

the conductivity is simplified as

$$\sigma_2 = \sum_{E(\mathbf{k}')<E_F<E(\mathbf{k})} \frac{\hbar e^2}{i}\frac{-\langle \mathbf{k}|v_y|\mathbf{k}'\rangle\langle \mathbf{k}'|v_x|\mathbf{k}\rangle + \langle \mathbf{k}|v_x|\mathbf{k}'\rangle\langle \mathbf{k}'|v_y|\mathbf{k}\rangle}{[E(\mathbf{k}') - E(\mathbf{k})]^2}. \tag{A.3}$$

In order to simplify the Hall conductivity from Eq. (6.24) to Eq. (6.26), we need to replace velocity operator by partial derivative

$$\mathbf{v} = \frac{1}{\hbar}\boldsymbol{\nabla}_{\mathbf{k}} H. \tag{A.4}$$

The matrix element of the velocity operator could be written as

$$\langle u(\mathbf{k}')|H|u(\mathbf{k})\rangle = 0, \tag{A.5}$$

$$\begin{aligned}\langle u(\mathbf{k}')|\frac{\partial H}{\partial k_i}|u(\mathbf{k})\rangle &= -\langle\frac{\partial u(\mathbf{k}')}{\partial k_i}|H|u(\mathbf{k})\rangle - \langle u(\mathbf{k}')|H|\frac{\partial u(\mathbf{k})}{\partial k_i}\rangle \\ &= -E(\mathbf{k})\langle\frac{\partial u(\mathbf{k}')}{\partial k_i}|u(\mathbf{k})\rangle - E(\mathbf{k}')\langle u(\mathbf{k}')|\frac{\partial u(\mathbf{k})}{\partial k_i}\rangle \\ &= [E(\mathbf{k}) - E(\mathbf{k}')]\langle u(\mathbf{k}')|\frac{\partial u(\mathbf{k})}{\partial k_i}\rangle \\ &= -[E(\mathbf{k}) - E(\mathbf{k}')]\langle\frac{\partial u(\mathbf{k}')}{\partial k_i}|u(\mathbf{k})\rangle.\end{aligned} \tag{A.6}$$

Substitute the matrix element in Eq. (A.6), we obtain

$$\begin{aligned}\sigma_2 = &\sum_{E(\mathbf{k}')<E_F}^{E_F<E(\mathbf{k})} \frac{e^2}{i\hbar}(\langle\frac{\partial u(\mathbf{k}')}{\partial k_y}|u(\mathbf{k})\rangle\langle u(\mathbf{k})|\frac{\partial u(\mathbf{k}')}{\partial k_x}\rangle - \langle\frac{\partial u(\mathbf{k}')}{\partial k_x}|u(\mathbf{k})\rangle\langle u(\mathbf{k})|\frac{\partial u(\mathbf{k}')}{\partial k_y}\rangle), \\ = &\sum_{E(\mathbf{k}'),E(\mathbf{k}")<E_F}^{E_F<E(\mathbf{k})} \frac{e^2}{i\hbar}(\langle\frac{\partial u(\mathbf{k}')}{\partial k_y}|u(\mathbf{k})\rangle\langle u(\mathbf{k})|\frac{\partial u(\mathbf{k}')}{\partial k_x}\rangle - \langle\frac{\partial u(\mathbf{k}')}{\partial k_x}|u(\mathbf{k})\rangle\langle u(\mathbf{k})|\frac{\partial u(\mathbf{k}')}{\partial k_y}\rangle) \\ &+ \frac{e^2}{i\hbar}(\langle\frac{\partial u(\mathbf{k}')}{\partial k_y}|u(\mathbf{k}")\rangle\langle u(\mathbf{k}")|\frac{\partial u(\mathbf{k}')}{\partial k_x}\rangle - \langle\frac{\partial u(\mathbf{k}')}{\partial k_x}|u(\mathbf{k}")\rangle\langle u(\mathbf{k}")|\frac{\partial u(\mathbf{k}')}{\partial k_y}\rangle),\end{aligned} \tag{A.7}$$

due to the relation

$$\begin{aligned}&\sum_{E(\mathbf{k}'),E(\mathbf{k}")<E_F} \langle\frac{\partial u(\mathbf{k}')}{\partial k_y}|u(\mathbf{k}")\rangle\langle u(\mathbf{k}")|\frac{\partial u(\mathbf{k}')}{\partial k_x}\rangle - \langle\frac{\partial u(\mathbf{k}')}{\partial k_x}|u(\mathbf{k}")\rangle\langle u(\mathbf{k}")|\frac{\partial u(\mathbf{k}')}{\partial k_y}\rangle \\ =&\sum_{E(\mathbf{k}'),E(\mathbf{k}")<E_F} \langle u(\mathbf{k}')|\frac{\partial u(\mathbf{k}")}{\partial k_x}\rangle\langle\frac{\partial u(\mathbf{k}")}{\partial k_y}|u(\mathbf{k}')\rangle - \langle\frac{\partial u(\mathbf{k}')}{\partial k_x}|u(\mathbf{k}")\rangle\langle u(\mathbf{k}")|\frac{\partial u(\mathbf{k}')}{\partial k_y}\rangle \\ =&\sum_{E(\mathbf{k}'),E(\mathbf{k}")<E_F} \langle u(\mathbf{k}")|\frac{\partial u(\mathbf{k}')}{\partial k_x}\rangle\langle\frac{\partial u(\mathbf{k}')}{\partial k_y}|u(\mathbf{k}")\rangle - \langle\frac{\partial u(\mathbf{k}')}{\partial k_x}|u(\mathbf{k}")\rangle\langle u(\mathbf{k}")|\frac{\partial u(\mathbf{k}')}{\partial k_y}\rangle \\ =&0.\end{aligned} \tag{A.8}$$

Then the completeness of the Hilbert space is used if we include the all the states below and above the Fermi energy, i.e., $\sum_{E(\mathbf{k}")<E_F<E(\mathbf{k})} |u(\mathbf{k}")\rangle\langle u(\mathbf{k}")| + |u(\mathbf{k})\rangle\langle u(\mathbf{k})| = 1$, Eq.

(A.7) is further simplified

$$\sigma_2 \sum_{E(\mathbf{k})<E_F} \frac{e^2}{i\hbar}(\langle \frac{\partial u(\mathbf{k})}{\partial k_y} | \frac{\partial u(\mathbf{k})}{\partial k_x} \rangle - \langle \frac{\partial u(\mathbf{k})}{\partial k_x} | \frac{\partial u(\mathbf{k})}{\partial k_y} \rangle). \tag{A.9}$$

If it's a two band model and the Fermi energy is located in the gap, the summation will be over all the states of the lower band, i.e., the BZ integration of the lower band

$$\sigma_2 = -i\frac{e^2}{\hbar} \int_{BZ} \langle \frac{\partial u(\mathbf{k})}{\partial k_y} | \frac{\partial u(\mathbf{k})}{\partial k_x} \rangle - \langle \frac{\partial u(\mathbf{k})}{\partial k_x} | \frac{\partial u(\mathbf{k})}{\partial k_y} \rangle \tag{A.10}$$

APPENDIX B

COUPLED WAVE EQUATIONS FOR THE HALDANE MODEL IN SL

We set $\mathbf{k}_p = \mathbf{k}_1$, $\mathbf{k}_+ = -\mathbf{k}_3$ and $\mathbf{k}_- = -\mathbf{k}_2$. There will be directional emission in $\mathbf{k}_\pm$ by TDS $|e_{\mathbf{k}_\pm}\rangle$. The emitted photons in $\mathbf{k}_\pm$ interact with the atomic ensemble the same way as the probe field $\mathbf{k}_p$, creating TDS and resulting in directional emission in the other modes. For example, emission at $\mathbf{k}_+$ excites the atom ensemble and leads to emission at $\mathbf{k}_-$ and $\mathbf{k}_p$. Therefore, the three optical fields in $\mathbf{k}_{p,\pm}$ are coupled via the atoms. In the following, we derive the coupling equations.

The expectation value of the dipole momentum of the jth atom at position $\mathbf{r}_j$ is

$$\begin{aligned}\langle\Psi|\boldsymbol{\mu}_j|\Psi\rangle &= \sum_{\mathbf{k}}\langle G|\boldsymbol{\mu}_j|e_{\mathbf{k}}\rangle + c.c. \\ &= \frac{\mu}{\sqrt{N}}\sum_{\mathbf{k}} c_{\mathbf{k}} e^{i\mathbf{k}\cdot\mathbf{r}_j} + c.c.,\end{aligned} \tag{B.1}$$

where $\boldsymbol{\mu}$ is the dipole operator of the jth atom and $\mu = \langle g_j|\boldsymbol{\mu}|e_j\rangle$. Since the atoms are homogeneously distributed, the polarization density as a function of positions is,

$$P(\mathbf{r}) = \frac{N}{V}\frac{\mu}{\sqrt{N}}\sum_{\mathbf{k}} c_{\mathbf{k}} e^{i\mathbf{k}\cdot\mathbf{r}} + c.c., \tag{B.2}$$

where V is the volume of the atomic ensemble. The probe field Rabi frequency is $\Omega_p = \mu E_p/\hbar$ with E_p being the probe field strength. The polarization density contains the Frourier components in $\mathbf{k}_\pm$, $P_{\pm,p} = \epsilon_0\chi_\pm E_p$ with $\chi_\pm = \sqrt{N}\mu c_{\mathbf{k}_\pm}/V\epsilon_0 E_p$ and ϵ_0 is the permittivity in vacuum. The notation $P_{\pm,p}$ means the $\mathbf{k}_\pm$ Fourier component of polarization density generated by optical field in $\mathbf{k}_p$. Once modes $\mathbf{k}_\pm$ are excited and the corresponding fields $E_\pm$ are generated, they also polarize the atoms. For $\phi_1 = 0$, $\phi_2 = 4\pi/3$

and $\phi_3 = 2\pi/3$, the three fields have a cyclic relation between each other. We have $P_{p,+} = \epsilon_0\chi_- E_+$, $P_{-,+} = \epsilon_0\chi_+ E_+$, $P_{p,-} = \epsilon_0\chi_+ E_-$and $P_{+,-} = \epsilon_0\chi_- E_-$.

We assume the quasi-static approximation in which the atoms are assumed in steady states. This approximation is justified when the pulse duration is much longer than the decoherence time $1/\gamma_e$. We also use the slowly-varying-envelop approximation. The fields in the three relevant modes $\mathbf{k}_j$ with $j = p, +$ and $-$ are denoted as $E_j(\mathbf{r})e^{-i\nu_p t + i\mathbf{k}_j\cdot\mathbf{r}}$ where $|\mathbf{k}_j| = \nu_p/c \equiv k_p$. The coupled-wave Maxwell equations for the three modes are

$$(\hat{\mathbf{k}}_p \cdot \boldsymbol{\nabla} + \frac{1}{\nu_g}\frac{\partial}{\partial t})E_p = \frac{ik_p}{2}(\chi_0 E_p + \chi_- E_+ + \chi_+ E_-), \tag{B.3}$$

$$(\hat{\mathbf{k}}_+ \cdot \boldsymbol{\nabla} + \frac{1}{\nu_g}\frac{\partial}{\partial t})E_+ = \frac{ik_p}{2}(\chi_0 E_+ + \chi_- E_- + \chi_+ E_p), \tag{B.4}$$

$$(\hat{\mathbf{k}}_- \cdot \boldsymbol{\nabla} + \frac{1}{\nu_g}\frac{\partial}{\partial t})E_- = \frac{ik_p}{2}(\chi_0 E_- + \chi_- E_p + \chi_+ E_+), \tag{B.5}$$

where $\hat{\mathbf{k}}_{p,\pm}$ are the unit vectors in the directions of $\mathbf{k}_{p/+/-}$ and ν_g is the group velocity of the pulses.

APPENDIX C

CAT STATE PREPARATION AND THE DISCREPANCY DUE TO DIFFERENCE RABI FREQUENCIES OF DIFFERENT NUMBER STATES

We can also obtain a coherent state superposition of single mode, $|\alpha\rangle - |\alpha\rangle$. In the process shown in Fig. 8.1, after we obtain $|\psi_2\rangle$, we detune all cavities out of resonance with the atom and cavity a_2 is detuned from cavities by an amount ϵ for a time t. A dynamic phase $N\phi$ with $\phi = -\epsilon t$ is then attached to the wavefunction,

$$|\psi_2^{'}\rangle = \frac{1}{\sqrt{2}}(e^{iN\phi}|g\rangle|0,0,N\rangle - |e\rangle|0,N-1,0\rangle). \tag{C.1}$$

We choose $\phi = \pi$, recover the on resonance interaction and the periodic modulation and wait for a time $2T$. The wavefunction is then

$$|\psi_3^{'}\rangle = \frac{1}{\sqrt{2}}((-1)^N|g\rangle|N,0,0\rangle - |e\rangle|N-1,0,0\rangle). \tag{C.2}$$

After resonant interaction only with a_1 for a $\pi/2$ Rabi rotation, the final state is $|\psi_4^{'}\rangle = 1/2[(-1)^N - 1]|g\rangle|N,0,0\rangle - 1/2[(-1)^N + 1]|e\rangle|N-1,0,0\rangle$, which is $-|e\rangle|N-1,0,0\rangle$ for even N or $-|g\rangle|N,0,0\rangle$ for odd N. The even and odd number states are separated. When the initial state is a coherent state, we obtain approximately $|\alpha\rangle + |-\alpha\rangle$ entangled with $|e\rangle$ states.

The discrepancy for the cat state here and for the entangled coherent state discussed in Section 8 lies in the imperfection of the $\pi/2$ and π pulses for the different number states of a coherent state. However, this discrepancy is negligible for large α. Here we take the

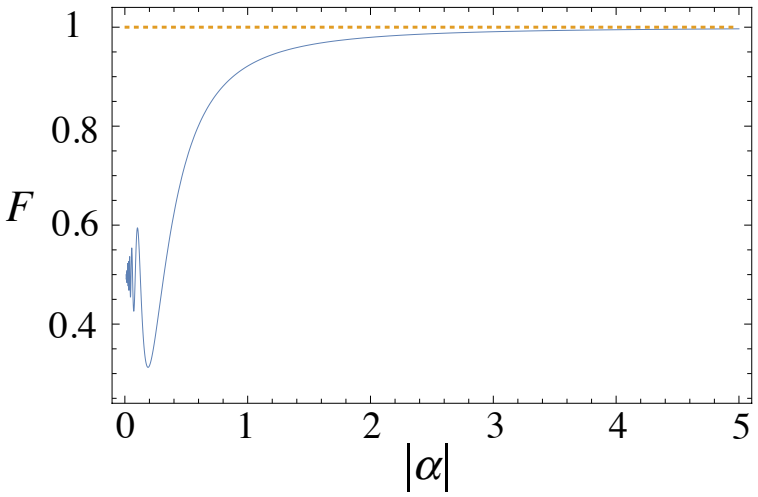

Figure C.1: The fidelity F as a function of $|\alpha|$.

$\pi/2$ pulse for example. We start from the state $|g\rangle|\alpha\rangle$ and choose the interaction time such that for the average photon number $\bar{n} = |\alpha|^2$ the pulse area is $\pi/2$. After the $\pi/2$ pulse, the state is

$$|\psi_a\rangle = \sum_{n=0}^{\infty} e^{-|\alpha|^2} \frac{\alpha^n}{\sqrt{n!}} \cos(\frac{\pi}{4}\sqrt{\frac{n}{\bar{n}}})|g\rangle|n\rangle - e^{-|\alpha|^2} \frac{\alpha^{n+1}}{\sqrt{(n+1)!}} \sin(\frac{\pi}{4}\sqrt{\frac{n+1}{\bar{n}}})|e\rangle|n\rangle.$$

The overlap between $|\psi_a\rangle$ and the target state $|\psi_b\rangle = (|g\rangle|\alpha\rangle + |e\rangle|\alpha\rangle)/\sqrt{2}$ (the fidelity) is

$$F = |\langle\psi_b|\psi_a\rangle|^2 = \frac{1}{2}\left| e^{-|\alpha|^2} \sum_{n=0}^{\infty} \frac{|\alpha|^{2n}}{n!} [\cos(\frac{\pi}{4}\sqrt{\frac{n}{\bar{n}}}) + \frac{\alpha}{\sqrt{\bar{n}+1}} \sin(\frac{\pi}{4}\sqrt{\frac{n+1}{\bar{n}}})] \right|^2 .$$

In Fig. (C.1), we draw F as a function of $|\alpha|$. It is clear that for $|\alpha| > 1$, $F > 0.9$ and approaches to 1 quickly.

APPENDIX D

THE DERIVATION FOR THE EFFECTIVE HAMILTONIAN IN THE SYNTHETIC MAGNETIC FIELD GENERATION

The Hamiltonian of an ensemble of Λ-type three-level atoms with the ground state $|c\rangle$, the excited state $|b\rangle$ and the metastable state $|a\rangle$ in a standing wave coupled EIT is

$$\begin{aligned} H_{\text{EIT}} =& \Delta_p |b_m\rangle\langle b_m| + \Delta_{2ph} |a_m\rangle\langle a_m| + \\ &+ \sum_m (2\Omega_1 \cos(k_1 r) + 2\Omega_2 \cos(k_2 r + \frac{\theta}{2}) e^{i\nu_d t}) |b_m\rangle\langle a_m| \\ &+ \Omega_p e^{ik_p r_m} |b_m\rangle\langle c_m| + h.c.. \end{aligned} \tag{D.1}$$

where $H_s = \Delta_p = \omega_{bc} - \nu_p$ is the single photon detuning and $\Delta_{2ph} = \Delta_p - \Delta_c = \Delta_p - (\omega_{ba} - \nu_1)$ is the two photon detuning, $\nu_d = \nu_1 - \nu_2$ is the frequency difference of two standing waves. $|b\rangle$ and $|a\rangle$ are coupled with two standing waves, one is near resonant with frequency $\nu_1 \approx \omega_{ba}$ and the other is far-detuning with frequency ν_2. The Hamiltonian can therefore be decomposed to

$$H_{\text{EIT}} = H_0 + H_1 e^{i\nu t} + H_{-1} e^{-i\nu t}, \tag{D.2}$$

with

$$\begin{aligned} H_0 =& \sum_m \Delta_p |b_m\rangle\langle b_m| + \Delta_{2ph} |a_m\rangle\langle a_m| \\ &+ 2\Omega \cos(k_1 r_m) |b_m\rangle\langle a_m| + \Omega_p e^{ik_p r_m} |b_m\rangle\langle c_m| + h.c., \end{aligned} \tag{D.3}$$

$$H_1 = H_{-1}^\dagger = 2\Omega_2 \sum_m \cos(k_2 r + \frac{\theta}{2}) |b_m\rangle\langle a_m| \tag{D.4}$$

Using the standard second-order perturbation theory and we neglect high frequency

Floquet sidebands, the effective Hamiltonian is then

$$\begin{aligned} H_{\text{eff}} =& H_0 + \frac{1}{\nu_d}[H_1, H_{-1}] \\ =& \sum_m (\Delta_p + 2\kappa)|b_m\rangle\langle b_m| + (\Delta_{2ph} - 2\kappa)|a_m\rangle\langle a_m| \\ &+ \sum_m 2\kappa \cos(2k_2 r_m + \theta)(|b_m\rangle\langle b_m| - |a_m\rangle\langle a_m|) \\ &+ \sum_m 2\Omega \cos(k_1 r_m)(|b_m\rangle\langle a_m| + h.c.) \\ &+ \sum_m \Omega_p e^{ik_p r_m}|b_m\rangle c a_m + h.c.. \end{aligned} \tag{D.5}$$

where $\kappa = 2\Omega_2^2/\nu_d$. we could treat the wavevector of the two standing wave the same, i.e., $k_c = \nu_1/c \approx \nu_2/c$, provided that negligible phase difference is accumulated in the region of atomic sample, i.e., $(\nu_1 - \nu_2)L/c \ll \pi$, L is the length of the cell. It is justified with $\nu_1 - \nu_2 = 2\pi \times 300MHz$ and $L = 6cm$, so $(\nu_1 - \nu_2)L/c = 0.12\pi \ll \pi$. Finally, we obtain the effective Hamiltonian in Eq. (9.1)